

# POLITECNICO DI TORINO

Mechanical, Aerospace, Automotive and Production Engineering Department

## Master's degree in Mechanical Engineering



## Correlation between the productivity and mechanical performance of AISI 316L parts produced via Laser powder bed fusion process

### Tutors:

prof. Luca Iuliano  
prof. Abdollah Saboori

### Candidate:

Giovanni Del Greco

October 2021



## *Abstract*

Laser Powder Bed Fusion (LPBF) is an Additive Manufacturing (AM) process, able to generate parts of a quality comparable to those produced through conventional manufacturing methods. The technology allows the production of complex objects directly from metal powder, exploiting a layer-by-layer build-up methodology.

Among the many advantages of SLM, low productivity is still one of the most difficult challenges to address since it drastically increases the overall production time. Consequently, the ability to manufacture components with enhanced accuracy and quality is counterbalanced by high manufacturing costs.

This thesis aims to study the relationship between productivity and mechanical properties of AISI 316L parts. Process productivity depends on many factors; one of them is the Build Rate (BR) that directly depends on Volumetric Energy Density (VED).

In this work, a procedure to select a process parameter combination with an increased BR is presented and experimentally validated, exploiting the VED lumped parameter.

This thesis is divided into five chapters.

The first one, "Introduction", presents a general overview of AM.

Chapter 2, "State of Art", deals with the main findings reviewed during the research activity. First, the main process parameters and their effects on productivity and mechanical features are studied, providing a suitable productivity and cost equation model. In addition, it describes the principal procedures to select a set of process parameters with optimized BR, as well as some case studies with the support of previous works.

Chapter 3, "Materials and methods", includes the experimental part of the thesis. To run the experiment, different combinations of process parameters were used to produce 24 test samples.

The methods and the procedures used for the characterization of the samples are there described in detail. The purpose of the characterization was to identify the relation between the porosity percentage of the trial cubes and the VED values used to print them. Once identified the most promising parameter sets which showed the best results in terms of porosity, tensile specimens were produced with those characteristics to test the mechanical properties.

Chapter 4, "Results and discussions", discusses the influence of process parameters on porosity, density, surface quality and roughness, tensile properties, and build time of 316L parts. The tensile test results only showed a slight difference in Yield Strength and ultimate tensile strength between specimens produced with high VED and those built with low VED. Despite this difference, two case studies are presented to highlight the significant advantages that the use of optimized parameters has, both in terms of time and costs: the low VED level allows to build products with an 18% faster build time.

Finally, chapter 5 summarizes the conclusion of the whole work, clearly underlining the fact that the build time can be improved while maintaining good mechanical properties by adjusting the process parameters.

# ***Index***

<i>1 Introduction</i> .....	1
<i>2 State of the art</i> .....	4
2.1 Process parameters .....	5
2.1.1 Laser Power .....	6
2.1.2 Scan Speed.....	7
2.1.3 Hatch Distance.....	7
2.1.4 Scanning Strategy .....	8
2.1.5 Layer Thickness.....	9
2.1.6 Combined process parameters .....	9
2.2 Productivity .....	11
2.2.1 Processing Time .....	11
2.2.2 Build time model .....	11
2.2.3 Build Rate .....	12
2.2.4 Cost Model .....	12
2.3 Quality Parameters .....	14
2.3.1 Surface Roughness .....	15
2.3.2 Microstructure .....	15
2.3.2.1 AISI 316L microstructure.....	15
2.3.3 Porosity.....	16
2.3.4 Densification behavior.....	17
2.3.5 Mechanical properties.....	18
2.3.5.1 Residual stress .....	21
2.4 Process optimization methods .....	21
2.4.1 Layer thickness increase.....	21
2.4.2 VED method.....	21
2.4.3 Taguchi and ANOVA analysis .....	22
2.4.4 Optimization algorithms and numerical modeling .....	23
2.5 Case studies .....	23
2.5.1 Case study n.1: Layer thickness increase .....	23
2.5.2 Case study n.2: VED density control method.....	23
2.6 Conclusions .....	24
<i>3 Materials and methods</i> .....	27
3.1 Experimental equipment: Concept Laser Mlab R .....	27
3.2 Material: AISI 316L .....	29
3.3 Design of experiments (Doe): process parameters selection.....	30
3.4 Samples characterization .....	33

3.4.1 Surface morphology .....	33
3.4.2 Dimensional accuracy.....	34
3.4.3 Surface roughness characterization .....	34
3.4.4 Measurement of density and porosity.....	36
3.4.5 Mechanical characterization: tensile testing.....	37
<i>4 Results and discussions</i> .....	39
4.1 Analysis of the effects of single process parameters on relative density and porosity.....	39
4.1.1 Influence of scanning speed on density .....	41
4.1.2 Influence of hatch distance on density.....	42
4.1.3 Influence of scanning speed on porosity .....	43
4.1.4 Influence of hatch distance on porosity .....	45
4.2 Analysis of the effects of combined process parameters on relative density and porosity .....	48
4.2.1 The relationship between volumetric energy density and relative density.....	48
4.2.2 The relationship between volumetric energy density and porosity .....	50
4.2.3 The relationship between productivity and density/porosity.....	51
4.3 Analysis of the surface quality .....	52
4.3.1 Dimensional accuracy.....	52
4.3.2 Surface roughness.....	55
4.3.3 Effects of VED on surface roughness.....	56
4.3.4 Effects of productivity on surface roughness .....	57
4.4 Mechanical characterization .....	58
4.4.1 Selection of the process parameters for mechanical testing .....	58
4.4.2 Tensile test.....	59
4.5 Cost analysis .....	62
4.5.1 Case study 1: Bearing block .....	63
4.5.2 Case study 2: Turbine wheel .....	64
<i>5 Conclusions</i> .....	67
<i>6 List of acronyms</i> .....	69
<i>7 List of symbols</i> .....	71
<i>9 Appendix</i> .....	77



# ***1 Introduction***

Additive manufacturing (AM) is a machinery process capable of creating three-dimensional (3D) objects by adding layer-upon layers of material. This process, comprising a family of different technologies, starts from a computer-aided design (CAD) file that includes digital data about how the finished product should look. AM is achieved using an additive process; it differs from conventional machining techniques that generally remove material by subtractive methods like drilling or lathe-turning [1].

Charles Hull developed this technology in 1986 [2]. At that time, the more commonly used term to describe the process was Rapid Prototyping (RP), mirroring its main application: the manufacture of prototypes more quickly and efficiently than conventional methods, but at a cost and speed not competitive for production. After more than thirty years of development, AM has become an ordinary fabrication process involving various materials and new technologies. It is possible to distinguish multiple similarities between the different technologies. All AM technologies require steps that move from the virtual 3D geometric representations to the physical model. Due to the variety of product demands and complexity, AM technology develops single processes in different ways. However, according to *Gibson* [3], it is possible to define the same sequence of operations in the production process. The following eight steps represent this sequence:

1. Conceptualization and CAD
2. Conversion to Stereolithography (STL) file
3. Transfer to AM machine and STL file manipulation
4. Machine setup
5. Build
6. Part removal
7. Post-processing of part
8. Application

All AM parts start from solid modeling software. The output of the first step is a CAD surface representation which is then converted into an STL file. This format provides details about the external surface of the original CAD model and the basic calculations of the two-dimensional (2D) slices of the part. The following stage concerns the file uploading on the AM machine. There could be some corrections to the file, so that size, position, and orientation match the AM technology restrictions. Afterward, the machine is set up according to the building parameters and the build process can occur. Building the part is mainly an automated stage in which supervision is minimal. When the layered piece is completed, the operator needs to interact with the machine as the product must be removed. Finally, to exploit the manufactured part in its application field, some finishing operations are required. For example, they may require additional treatments to enhance the final properties of the piece. The entire procedure is not necessarily a fast process; however, AM accelerates the design to market time with respect to conventional manufacturing and decreases the number of steps required to manufacture a good.

The feedstock material used to manufacture parts can be polymeric, metallic, concrete, ceramic, or composite. There are several criteria used to classify AM technology, such as machine architecture (laser, printer, etc.), starting material (polymeric, metallic, etc.), and the status of feedstock material (powder, liquid, etc.). Following the pioneering ASTM standards committee [1], seven families of processes can be distinguished:

- Vat Photopolymerization: an additive manufacturing process in which liquid photopolymer in a vat is selectively cured by light-activated polymerization.

- **Material Extrusion:** an additive manufacturing process in which material is selectively dispensed through a nozzle or orifice.
- **Material Jetting:** an additive manufacturing process in which droplets of build material are selectively deposited.
- **Binder Jetting:** an additive manufacturing process in which a liquid bonding agent is selectively deposited to join powder materials.
- **Powder Bed Fusion:** an additive manufacturing process in which thermal energy selectively fuses regions of a powder bed.
- **Sheet Lamination:** an additive manufacturing process in which sheets of material are bonded to form an object.
- **Directed Energy Deposition:** an additive manufacturing process in which focused thermal energy is used to fuse materials by melting as they are being deposited.

A more practical way to categorize these processes was proposed by Guo [4]. This classification groups the methods according to the state of the starting material: (1) liquid, (2) filament/paste, (3) powder, and (4) solid sheet. Other researchers also used such a form of categorization, and it is represented in Table 1.1.

*Table 1.1: AM processes classification according to supply material state*

<b>Material State</b>	<b>Process</b>	<b>Material Preparation</b>	<b>Layer creation technique</b>	<b>Materials</b>
<b>Liquid</b>	SLA	Liquid resin in a vat	Laser scanning/light projection	UV curable resin, ceramic
	MJM	Liquid polymer in jet	Link-jet printing	UV curable resin, wax
	RFP	Liquid droplet in nozzle	On-demand droplet deposition	Water
<b>Filament/Paste</b>	FDM	Filament melted in nozzle	Continuous extrusion and deposition	Thermoplastics, wax
	Robocasting	Paste in nozzle	Continuous extrusion	Ceramic paste
	FEF	Paste in nozzle	Continuous extrusion	Ceramic paste
<b>Powder</b>	SLS	Powder in bed	Laser scanning	Thermoplastic, ceramic
	DMLS	Powder in bed	Laser scanning	Metal
	SLM	Powder in bed	Laser scanning	Metal
	EBM	Powder in bed	Electron beam scanning	Metal
	LMD	Powder injection through nozzle	On-demand powder injection and melted by laser	Metal
<b>Solid sheet</b>	LOM	Laser cutting	Feeding and binding of sheets with adhesives	Paper, plastic, metal

SLA: stereolithography; MJM: multi-jet modeling; RFP: rapid freeze prototyping; FDM: fused deposition modeling; FEF: freeze-form extrusion fabrication; SLS: selective laser sintering; DMLS: direct metal laser sintering; SLM: selective laser melting; EBM: electron beam melting; LMD: laser metal deposition; LOM: laminated object manufacturing.

This table is not an exhaustive list of every available technology; instead, there is a focus on those processes which have shown to be promising for production applications and are widely used across industry sectors. In particular, aerospace, biomedical, and automotive fields are increasing their interest in such technologies thanks to the competitive advantages offered by AM. The competitive advantages are geometrical freedom, shortened design to product time, mass customization, and material flexibility. More specifically, AM provides the possibility to create high complexity customized parts on demand. As a result, the production becomes more straightforward.

Moreover, it is even possible to achieve one-step production processes for complex products since pieces can consolidate into a single component, and even complete assemblies with moving parts are feasible. Furthermore, since production steps such as assembling, cutting, and creating molds are dismissed, this technology does not present any restrictions on complexity; it achieves any shape without representative increases in manufacture time or pricing. As a result, products can be topologically optimized to become lighter, stronger, and more performant. This technique is also sustainable; it generates savings in material since it only uses what is needed and is compatible with recycling. Also, by using this technology, manufacturers can achieve the versatility some industries need. For example, creating a medical prosthesis might require adjustments for every patient; with AM, small production batches become feasible.

Despite the competitive advantages listed, the optimization of the practice requires facing some challenges. Productivity is one of those conditions to turn AM processes into a production technique for commercial components.

Therefore, this thesis will focus on the production rate issues which characterize AM. The next chapter will review the literature, analyzing the problem to find out methodologies to overcome this issue.

## 2 State of the art

Powder Bed Fusion (PBF) processes allow the production of complex parts with good quality, directly from a CAD model, exploiting a layer-by-layer build-up methodology [5]. The different PBF technologies principally differ for the energy source used to melt the powder: Laser Powder Bed Fusion (LPBF) process adopts a laser energy source. At the same time, Electron Beam Melting (EBM) takes advantage of an electron beam source to produce the parts [6]. Laser Powder Bed Fusion (LPBF), also known as Selective Laser Melting (SLM), Direct Metal Laser Melting (DMLM), or Direct Metal Laser Sintering (DMLS), offers the possibility of building customized designs with elevated accuracy and higher complexity concerning conventional manufacturing processes [7]. The different technologies show a fundamental difference on a molecular level: LPBF, SLM, or DMLM process heats the metal substrate until it fully melts into a liquid. DMLS process does not fully melt the powder but heats it enough so that the surfaces weld together. Although this difference, all the processes have in common the same technological features reported in Figure 2.1: specific points of the powder bed are selectively scanned along predefined paths thanks to the energy developed by the laser source. The heated substrate then cools down and solidifies, creating a new layer of the product. After the first layer has been processed, the powder dispenser platform moves upward to supply the material required for printing a new surface. The building platform lowers down a distance equals to the thickness of a new layer, and the recoater transfers the material to the melting zone to form a new stratum. The same cycle continues until the final shape is obtained [8].

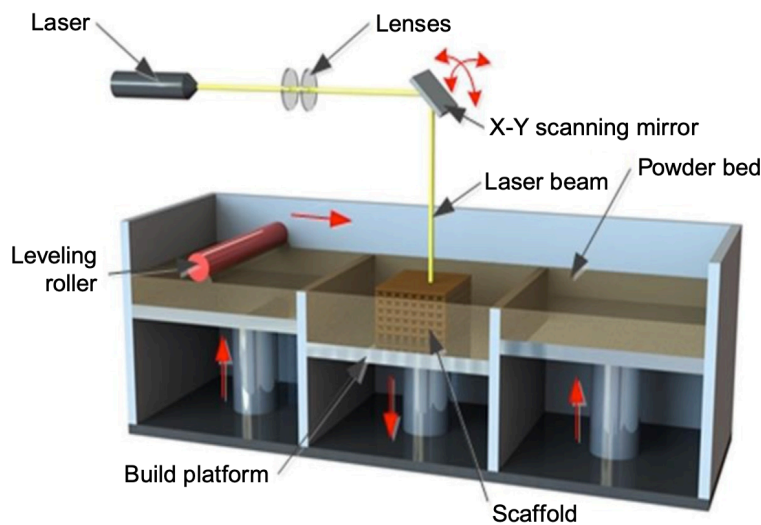


Figure 2.1: LPBF system schematic [61]

The process has the making of producing near-net-shaped parts, especially for high-performance application areas, as reported in table 2.1. In the last years, an increasing interest in this technology has arisen, particularly for its applications in the field of design for the automotive and aerospace industry, manufacture of parts for energy industries (nuclear, oil, and gas), and medical prostheses and implants production [9].

Table 2.1: Different alloys and their applications [10]

Alloy	Aerospace	Medical	Energy industries	Automotive	Marine	High-Temperature applications	Tools and molds
Aluminum	✓			✓			
Stainless steel	✓	✓	✓	✓	✓	✓	✓
Titanium	✓	✓		✓	✓	✓	
Inconel	✓				✓		

As mentioned by several researchers, the main problem of the method is its efficiency: the production rate is relatively low compared to traditional manufacturing techniques. Consequently, the process is characterized by high manufacturing costs [7], [9], [11]. The LPBF facility for manufacturing components with enhanced accuracy and quality is counterbalanced by a substantial production time, resulting in a drastic productivity drop. Consequently, this method is not used extensively and there is a need to overcome a modern design problem where large-scale parts are produced [7]. This unsolved drawback limits the field of application and distribution: nowadays, due to the limited build speed, LPBF is used primarily for high-end components, mostly within application fields where the production volumes are small and high costs are affordable [11]. The solution to the productivity dilemma would allow producing metallic 3D parts with complex geometry in a short production period [12]. This work analyzes the main process parameters and their effects on productivity and quality performances, providing a suitable productivity and cost equations model. Furthermore, the main procedures to select a process parameter combination with an increased build rate are described. Finally, some case studies are discussed.

## 2.1 Process parameters

Processing conditions include both machine settings, which typically are predefined, and process parameters that can be set depending on the case. In modern LPBF systems, there are over 100 processing parameters which can be grouped into five categories as shown in Figure 2.2: a) Laser related parameters, b) Scan related, c) Powder related, d) Atmosphere related, and e) Temperature related [3], [12]. The parameters optimization can have different purposes, such as full densification, high dimensional accuracy, low superficial roughness, and remarkable mechanical properties. In addition, the parameters involved vary depending on the alloy and final application [13].

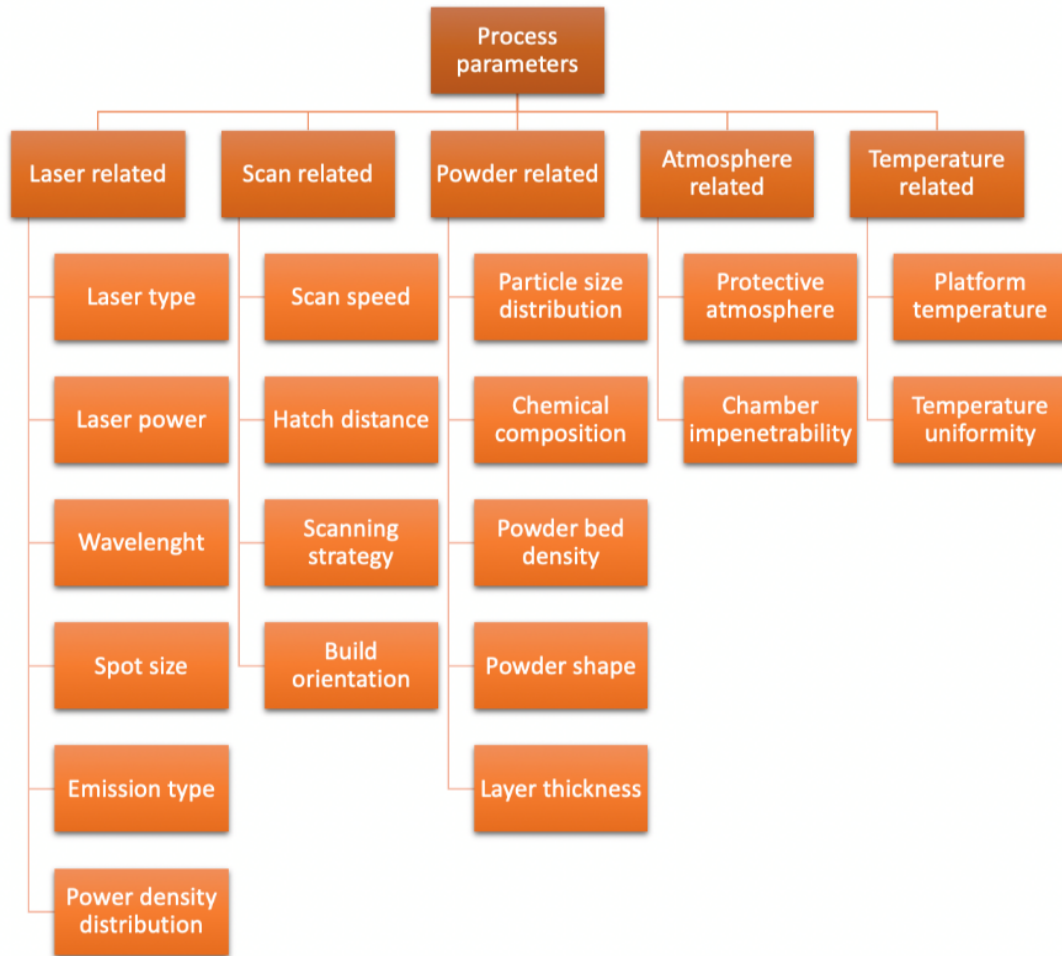


Figure 2.2: Principal process parameters

Amongst the factors, few parameters, namely laser power, scan speed, hatch distance, layer thickness, and scanning strategy, have a considerable impact on mechanical efficiency, economy, and ultimate quality of the entire PBF method [14]. Therefore, the following paragraphs briefly introduce the most influencing parameters, providing some lumped quantities used to analyze their combined effects. In comparison, their influence on the densification behavior and material quality properties are furtherly discussed in section 4.

### 2.1.1 Laser Power

Laser power ( $P$ ) determines the magnitude of the temperature gradient on the powder bed, influencing the overall melting behavior. This parameter directly affects the material characteristics such as density, surface quality, morphology, and mechanical properties. The required laser power typically increases with the material's melting point and lower platform temperature [3]. It also varies depending upon the layer thickness, scanning speed, and hatching distance to ensure the processed substrate's correct fusion. Commonly, high laser power gives rise to dense products with reduced porosity. *Pragana et al.* underlined that, for higher power values, an acceptable density could be reached, allowing a flexible range for the other process parameters [15]. *Leicht* and *Cacace* also set the laser to the maximum allowable power of 200 W, adjusting the remaining variables to optimize several properties of the built part [9], [16].

Despite the superior densification behavior, an extreme magnification of the laser power may result in vaporization phenomenon and melt-pool instability with the occurrence of residual stresses and

curling of the parts. [3]. Alternatively, low laser power produces better dimensional accuracy, but it results in reduced densification and elevated predisposition to layer delamination [3]. Machine manufacturers offer systems with laser power ranging between 100  $W$  and 400  $W$ , and in the case of most modern solutions, up to 1  $kW$ . Systems equipped with high-power lasers, most often with dual or quad laser solutions, exhibit a high gain in productivity of the whole process. For such machines, more alloys can be processed, and large-scale parts may be designed cost-effectively.

### 2.1.2 Scan Speed

Scanning speed ( $v_s$ ) is the forward velocity the laser beam moves over the powder bed. This parameter sets the amount of energy provided during the melting, contributing to the final surface quality of the part and the speed of the entire process.

LPBF machines allow to reach very high speeds, up to 10000  $mm/s$ , according to the technical datasheets; however, in the literature examined, the values typically range between 220÷3000  $mm/s$  [11], [15]. Indeed, high scan speed leads to reduced dwelling time, reduced melt-pool temperature, and hence incomplete melting; these drastically increase not only the part porosity but also the number of defects and the residual thermal stress [10]. However, an elevated velocity of the laser spot should be carefully associated with sufficiently high laser power and optimal hatch distance; otherwise, dense, nonporous material is rather difficult to achieve [17]. It is comprehensible that growth in the scan speed directly improves productivity: technically, if the scan speed doubles up, the build time halves. Therefore, a trade-off between the two opposite objectives, productivity and quality performances, should be found: enhancement to the build rate can be achieved by processing fast enough with slightly lower obtainable densities, thus not drastically sacrificing the component properties [18].

### 2.1.3 Hatch Distance

The spacing between two parallel laser tracks is typically called hatch distance ( $h$ ). This parameter joined with the spot size ( $d$ ), regulates powder melting, ensuring an adequate attachment between adjacent laser tracks. Neighboring strips are generally overlapped to avoid pores between subsequent tracks or rather unfused powder zones. Figure 2.3 underlines that an intersection in the tracks is necessary to obtain a dense solidification.

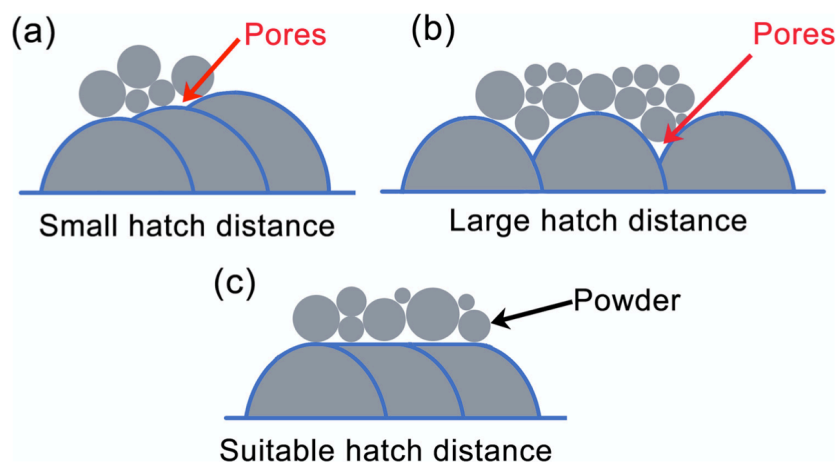


Figure 2.3: *Hatch* distance and overlap [62]

In fact, by diminishing the hatch distance, the increase in the overlap of each laser pass becomes more evident. Generally, higher overlap results in good surface roughness, low porosity, and well

mechanical properties [19]. However, when the hatch distance diminishes too much, the applied energy density rises with possible drawbacks: the outer edge of the laser track could over burn and the processed layer could warp and curve [17]. Furthermore, productivity drastically diminishes as the number of paths to be scanned increases. For these reasons, in most of the LPBF processes, the hatch spacing is always lower than the diameter of the laser beam to have better quality [20]; the optimal hatch spacing is calculated as:

$$h_{opt} = 0.25 \cdot d \quad (2.1)$$

According to the literature review, the typical range for this parameter is between 0,05 mm and 0,4 mm [15], [21].

#### 2.1.4 Scanning Strategy

The laser spot can cross a layer in various routes. This trajectory defines the scanning strategy, namely the path that the laser beam follows over the build platform, which may differ inside a single layer or between consecutive ones [22]. Scanning often occurs in two ways, contour mode and hatch mode. In contour mode, the beam scans the outer edge of a single layer. Processing hatch firstly and then contour paths guarantees better accuracy and surface finish. The most used hatch patterns are indicated in figure 2.4.

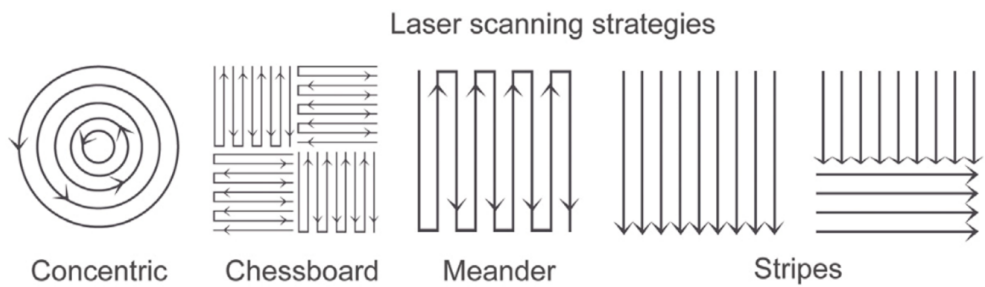


Figure 2.4: Examples of scanning strategies [26]

Common hatch trajectories are straight and parallel stripes, where each stripe is scanned sequentially and the stripe angle is rotated after processing every layer; concentric or meander routes; and chessboard sections, with each square being processed apart [3]. The choice of a suitable laser-pattern strongly influences the quality of the final component, in particular the magnitude of residual stresses. Many studies have shown that residual stresses and subsequent part deflection increase with scan lines extension. On the other hand, reducing the longest uninterrupted travel streak appears beneficial for the final features [10]. Based on these observations, dividing the scan area into squares of small segments, and traversing two subsequent layers with different rotation angles, successfully affects the residual stresses [21].

Even though an elaborated trajectory of the laser spot guarantees an amplified accuracy, optimizing the laser movements ensures minimum layer build time, which results in a great time saving for fabricating the whole part. Hence, the two outcomes should be appropriately balanced since the preferable strategy for improving the layer forming quality never corresponds to the least time-consuming one [23].

### 2.1.5 Layer Thickness

The layer thickness ( $z$ ) stands for the height of a single slice generated from the CAD model, and it is regulated by the downwards movement of the machine build platform.

The value this parameter can assume typically ranges between  $20\ \mu\text{m}$  and  $80\ \mu\text{m}$  [11]. The lower layer thickness size is suitable for high-resolution components, resulting in improved dimensional accuracy and reduced surface roughness values of the finished piece [27]. On the other hand, the energy source may not guarantee the correct fusion and cohesion between two successive layers for greater thicknesses. [24]. Therefore, the density and mechanical properties of the fabricated component drastically fall [25]. As a layered manufacturing method, LPBF efficiency increases with the slice thickness if the other parameters remain constant. An improved build speed is ensured if the total number of layers decreases and consequently also the required build time. Besides this, the tensile properties' degradation of the fabricated parts under higher slice thicknesses limits the achievable productivity gain. Therefore, the right balance between maximum permitted layer thickness and excellent tensile behavior is one of the focal points of LPBF optimization [19]. *de Formanoir et al.* proposed a “hull-core” strategy to match productivity requirements and part accuracy correctly. As shown in figure 2.5, this strategy involves a high productivity parameter set for the core and a high accuracy parameter set for the outer region [7].

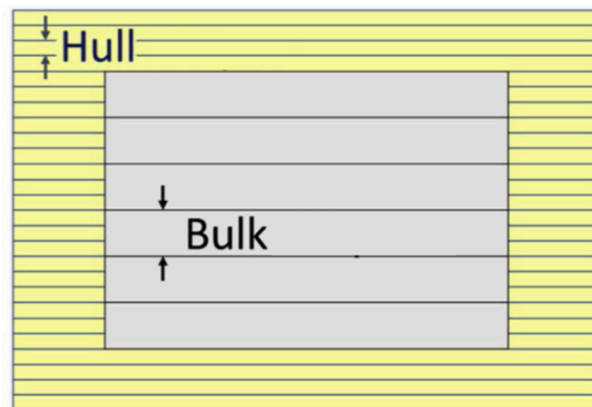


Figure 2.5: Hull-Bulk strategy [7]

### 2.1.6 Combined process parameters

Process parameters are strongly interdependent and mutually interacting [3]. Indeed, laser power ( $P$ ), scan speed ( $v_s$ ), hatch distance ( $h$ ), and layer thickness ( $z$ ) cannot be changed arbitrarily due to the fact they determine the energy density transferred to the area of the expanded melt pool [21]. Figure 2.6 presents the most dominant process parameters which influence the LPBF process. The combinations of the reported parameters determine the LPBF energy-input characteristics, which are helpful for process optimization.

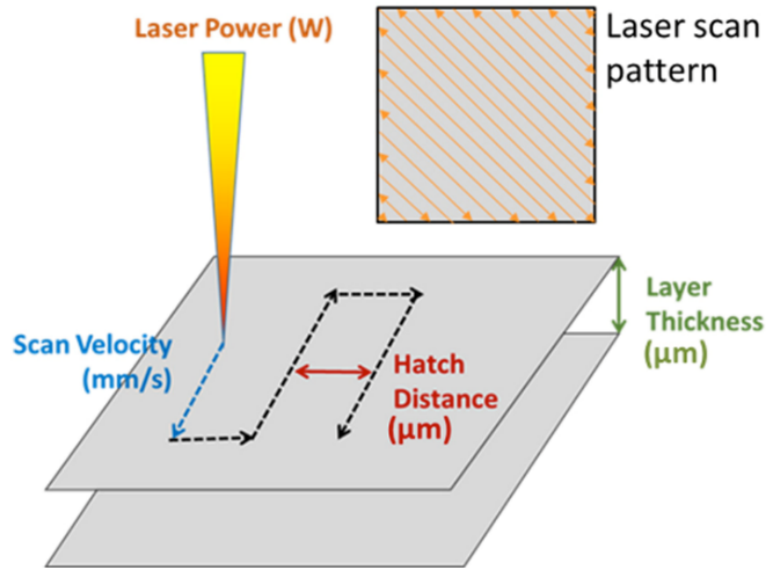


Figure 2.6: Dominant process parameters in LPBF process [13]

- The simplest quantity is the *Linear Energy Density (LED)*:

$$LED = \frac{P}{v_s} \left[ \frac{J}{mm} \right] \quad (2.2)$$

This variable relates laser power  $P$  and scanning speed  $v_s$ , as the beam energy is varied according to the scan speed to determine the dwell time of the laser source on the melt surface. Several authors have used this parameter to optimize geometrical accuracy and surface roughness [26]. At the same time, with the help of process window diagrams, it is possible to map combinations of the involved parameters, which assure the optimum density and reduced porosity of the produced object [3].

- The second quantity, used to quantify the amount of energy provided by the laser, is the *Areal Energy Density (AED)*:

$$AED = \frac{P}{h \cdot v_s} \left[ \frac{J}{mm^2} \right] \quad (2.3)$$

As the name suggests, AED is a physical quantity that specifies the amount of energy the part cross-section receives during the laser fusion process. Numerous investigators employed it as a simple method for correlating input factors to the processing conditions for fabricating the single layer. Hence it represents an adequate criterion among which inter-track pores formation can be studied [27].

- The most specific function is the *Volumetric Energy Density (VED)*:

$$VED = \frac{P}{z \cdot h \cdot v_s} \left[ \frac{J}{mm^3} \right] \quad (2.4)$$

VED is the most frequently adopted quantity to correlate process parameters with the mechanical, geometric, and density properties. From a physical point of view, it indicates the

energy a unit volume receives during the process, which can be used as an indicator to select the optimum range of parameters to cope with multiple objectives [26].

## 2.2 Productivity

The modest production rate of the LPBF process compared to conventional manufacturing technologies is well known, and intense effort is being given to the method to increase its efficiency [9]. The primary consequence of this problem is the high cost per part, which limits the metal AM extensive use in all the industrial fields. The economic restriction is often connected to machine cost, raw material cost, energy and gas consumption, and build time [16]. The productivity for LPBF technology is defined as parts' volume produced ( $V_p$ ) per timing of production, expressed as the total processing time ( $T_p$ ) [12]:

$$PR = \frac{V_p}{T_p} \left[ \frac{cm^3}{h} \right] \quad (2.5)$$

Productivity increases when the same processing time results in more volume produced or when it is possible to get the same output by reducing the total processing time. As introduced in section 1, nowadays, PBF processes have very low productivity indexes, which makes the methods almost in all cases unable to support high-volume production.

### 2.2.1 Processing Time

The total processing time consists of the pre-processing time ( $T_{pre}$ ), the build time ( $T_b$ ), and the post-processing time ( $T_{post}$ ) [28]:

$$T_p = T_{pre} + T_b + T_{post} \quad (2.6)$$

The first contribution includes the AM machine setup and loading of the STL file; the second part accounts for the time needed to build products; finally, the last term considers operations such as supports removal and finishing treatments on the object.

### 2.2.2 Build time model

The overall build time is the central contribution to the total processing time, given that preparation operations and post-processing are always required. The build-up process can be split into three parts: the delay time ( $T_d$ ), the recoating time ( $T_r$ ), and the material scanning time ( $T_s$ ) [3]:

$$T_b = T_d + T_r + T_s \quad (2.7)$$

The delay time represents a minimal contribution. It accounts for the accumulation of delays before and after scanning each layer due to the platform lowering. When the platform lowers in the correct position, the recoat system can spread a new layer of powder to permit the laser source to scan a new layer. The second part represents the time for a recoating blade (SLM) or roller (LPBF) to deposit material on each layer for further processing. Finally, the scanning component accounts for the time required to melt every slice.

### 2.2.3 Build Rate

The LPBF process cycle time can be divided into primary and auxiliary process time. The primary process time only consists of the time needed to melt every layer (scanning time), while the other operations are part of the auxiliary process time [9]. The process-related build-up rate gives a benchmark to measure the productivity of the LPBF process since the scan time constitutes the main contribution to the total manufacturing [29]:

$$BR = v_s \cdot h \cdot z \left[ \frac{mm^3}{s} \right] \quad (2.8)$$

The build rate represents the volume of material the process can melt per time unit, identified as the product of hatch distance ( $h$  in  $mm$ ), laser scan speed ( $v_s$  in  $mm/s$ ), and layer thickness ( $z$  in  $mm$ ). Therefore, enlarging the build rate would increase productivity, which will reduce the price per part accordingly. As equation (2.8) shows, theoretically, the most logical method to increment the building rate is combining a thicker powder layer with a larger scanning speed under a bigger hatch distance. Anyway, this straightforward approach directly damages the product's surface roughness, geometrical accuracy, and mechanical properties, as the following section will deeply remark.

For this reason, the trade-off between part quality and productivity is always required not only to avoid defects' formation but also to guarantee the economic sustainability of the method. Therefore, various approaches are implemented to address this issue, starting from augmented technological features. For example, as Table 2.2 reports, machines with enlarged build volume, able to process while using multiple laser-scanning systems ("twin or quad laser"), are very effective since the build space enlarges and several laser sources can process the piece simultaneously.

Table 2.2: LPBF Machines available on the market [30]–[32]

Company	Process	Machine	Laser	Build Volume	Layer Thickness	Scan Speed	Build Rate
EOS	DMLS	EOS M280	Yb-fiber laser, 200 W or 400 W	250 x 250 x 325 mm	20 $\mu$ m – 80 $\mu$ m	up to 7,0 m/s	7.2 – 28,8 cm <sup>3</sup> /h
		EOS M290	Yb-fiber laser, 400 W	250 x 250 x 325 mm	20 $\mu$ m – 100 $\mu$ m	up to 7,0 m/s	7.2 – 28,8 cm <sup>3</sup> /h
		EOS M400	Yb-fiber laser, 1000 W	400 x 400 x 400 mm	20 $\mu$ m – 100 $\mu$ m	up to 7,0 m/s	7.2 – 36,0 cm <sup>3</sup> /h
Concept Laser (GE Additive)	DMLM	M2 Series 5	dual-laser system: 2x400W or 2x1kW	245 x 245 x 350 mm	25 $\mu$ m – 120 $\mu$ m	up to 4,5 m/s	2-35 cm <sup>3</sup> /h or 2-93 cm <sup>3</sup> /h
SLM SOLUTIONS	SLM	SLM 125	IPG fiber laser, 400 W	125 x 125 x 125 mm	20 $\mu$ m – 75 $\mu$ m	up to 10 m/s	up to 25 cm <sup>3</sup> /h
		SLM 280 2.0	Single (400 W or 700 W) IPG fiber laser Twin (2x 400 W or 2x 700 W) IPG fiber lasers	280 x 280 x 365 mm	20 $\mu$ m – 90 $\mu$ m	up to 10 m/s	up to 113 cm <sup>3</sup> /h
		SLM 500	Twin (2x 400 W or 2x 700 W) IPG fiber laser Quad (4x 400 W or 4x 700 W) IPG fiber laser	500 x 280 x 365 mm	20 $\mu$ m - 90 $\mu$ m	up to 10 m/s	up to 171 cm <sup>3</sup> /h
		SLM 800	Quad (4x 700 W) IPG fiber laser	500 x 280 x 850 mm	20 $\mu$ m - 90 $\mu$ m	up to 10 m/s	171 cm <sup>3</sup> /h

### 2.2.4 Cost Model

Due to the vast build times that characterize this technology, LPBF is typically adopted to manufacture small batches of complex components. The complexity achievable in LPBF processes

benefits component functionality and weight reduction, which leads to feedstock material saving. Moreover, small lot sizes can be economically feasible. This asset is extremely powerful for medical and aerospace applications where complexity in part-customization is always required. On the other hand, traditional manufacturing methods are widely preferred for relatively simple designs and result in being economically advantageous [33].

The total cost of a job produced using AM technology breaks down into direct and indirect costs. The formers depend on the amount of material used, and the latter costs depend on the working time of the machine [34]:

$$C_{job} [\text{€}] = C_{direct} + C_{indirect} \quad (2.9)$$

The simplest cost model considers as direct costs only the material cost, while the indirect costs include amortization, electricity consumption, and gas consumption:

$$C_{job} = C_{material} + C_{operating} = m_{material} \cdot p_{powder} + \dot{C}_{operating} \cdot T_{bld} \quad (2.10)$$

$$C_{material} = k_s \cdot k_r \cdot V_{part} \cdot \rho_{material} \cdot p_{powder} \quad (2.11) [3]$$

Multiplying the part volume ( $V_p$  in  $cm^3$ ), times the material density ( $\rho_{material}$  in  $kg/cm^3$ ), and the powder price ( $p_{powder}$  in  $€/kg$ ) results in the material cost. Furthermore, this term is corrected with two coefficients,  $k_s$  and  $k_r$ . The former accounts for supports materials ( $1 \div 1.5$ ), while the latter regards powder recyclability ( $1 \div 7$ ).

The hourly machine cost lumps all the specific contributions which affect indirect costs. This quantity includes the principal factors depending on processing time: the machine overhead, the electricity consumption, and the gas consumption. The AM labor cost ( $C_l$ ) is generally negligible, as the time required to perform operations by workers is minimal:

$$\dot{C}_{operating} \left[ \frac{\text{€}}{h} \right] = \frac{Pp}{h_y \cdot a_y} + p_{el} \cdot c_{el} + p_{gas} \cdot c_{gas} \quad (2.12)$$

$Pp$ : machine purchase price [€]

$h_y$ : hours of production per year  $\left[ \frac{h}{y} \right]$

$a_y$ : amortization time [y]

$p_{el}$ : electricity price  $\left[ \frac{\text{€}}{KWh} \right]$

$c_{el}$ : electricity consumption  $\left[ \frac{KWh}{h} \right]$

$p_{gas}$ : gas price  $\left[ \frac{\text{€}}{l} \right]$

$c_{gas}$ : gas consumption  $\left[ \frac{l}{h} \right]$

Table 2.3 shows examples of machines' operating costs computed with equation (2.12). The hourly rate is calculated with these assumptions: production is prudentially restricted to 5000  $h$  per year [35]. Amortization time ( $a_y$ ) is equal to 5 years since technology evolves and new machine models are released continuously. Electricity and gas consumption data have been taken from the technical datasheets. The electricity cost considered is the Italian one of 0,217  $€/KWh$ , while the gas price equals 3,23  $€/m^3$ , considering the machine's building chamber filled with nitrogen [36].

Table 2.3: Machine's operating cost computed with equation (XII)

	Concept Laser Mlab R	EOS M290	SLM 500
Price [€]	131.150,00	574.000,00	1.230.000,00
Electricity consumption [KW <sub>h</sub> ]	1,5	2,4	10
Gas consumption [m <sup>3</sup> /h]	0,048	0,150	0,96
Operating cost [€/h]	5,73	23,97	54,47

The machine working time can be approximated with the build time ( $T_b$ ), considering that the delay time is negligible if compared to the scan time and the recoating time:

$$T_b [s] = \frac{V_{part}[mm^3]}{BR[mm^3/s]} + \frac{Part\ height[mm]}{layer\ thickness [mm]} \cdot T_r[s] \quad (2.13)$$

$$T_b [h] = \frac{\frac{V_{part}[mm^3]}{BR[mm^3/s]} + \frac{Part\ height[mm]}{layer\ thickness [mm]} \cdot T_r[s]}{3600} \quad (2.14)$$

$T_r$  is the recoating time of a single cycle, and for the Concept Laser Mlab R, it accounts for approximately 8 s.

This simplified model does not consider the costs linked to machine preparation and post-processing, which in general cannot be neglected. According to a survey, these costs account for up to 13% of the total production cost [37].

Other cost models consider the energy usage of the manufacturing step as a direct cost when assessing the life cycle of AM metal parts.

In this case, the energy usage is evaluated as the energy consumed to fabricate a unit mass of material [MJ/kg], often referred to as specific energy consumption (SEC).

This value varies between 80 and 600 MJ/kg for SLM and LPBF [38], and the typical value adopted in state-of-the-art is the one provided by *Kellens et al.* of 96.82 [MJ/kg] [39].

## 2.3 Quality Parameters

The quality of the final part is typically evaluated upon surface roughness, microstructure status, the presence of pores, and the mechanical properties of the final product, as figure 2.7 shows. Thus, the optimized process parameters are generally derived from complying with one or more objectives such as producing fully dense components, minimizing defects, reducing surface roughness, producing parts with good mechanical properties, and increasing the build rate [13].

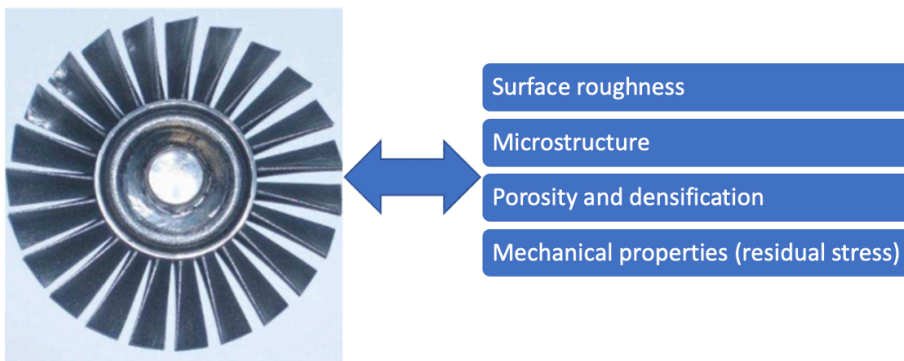


Figure 2.7: Product quality parameters

However, as said in the previous sections, these quality objectives never match productivity optimization, and it is rather challenging to maximize both priorities. Therefore, this chapter aims to analyze the quality of the parts produced with the LPBF process, taking advantage of previous research on Stainless steel, Aluminum, Inconel, and Titanium alloys pointing out how laser power, scan speed, layer thickness, and hatch distance impact the outcomes.

### 2.3.1 Surface Roughness

Surface roughness is sensitive on all the main process parameters ( $P$ ,  $h$ ,  $z$ ,  $v_s$ ) but mainly on hatch spacing [18], [40]. In fact, according to state of the art, hatch distance is the parameter that most influences surface finishing. For AISI 316L, a reduction in surface roughness is observed with decreasing hatch spacing until an optimum level, where further reductions result to be detrimental [18]. The same trend is found for Inconel alloys [41]. Deficient laser power generally leads to a high roughness and low dimensional accuracy. This phenomenon happens because the heat source cannot completely melt the powder layer, especially when the slice thickness is large. Increasing laser power can effectively reduce the roughness with improved geometrical accuracy and a suitable powder melting effect. However, this trend becomes unstable at very high power combined with high speed [41]. Increasing scan speed can negatively affect surface quality when it becomes too high to fully melt the powder bed surface [41]. This result has been confirmed by *Badrossamay et al.* work. Their study did not show an apparent trend between roughness and scan speed; however, with an evident increase in scan speed, AISI 316L built samples' roughness dramatically decreased [18]. *Guo* found that both too high and too low scan speed can lead to a decrease in the surface quality of Inconel Inconel-built.

Moreover, as pointed out in many research works, roughness parameters are slightly higher at greater layer thickness. This phenomenon happens because the melt pool formed with thicker layer thickness is larger; thus, solidification results in rougher surfaces [11], [18].

### 2.3.2 Microstructure

Additively manufactured components often show a complex microstructure with large elongated grains, which may cross several melt pool boundaries [16]. The processing parameters directly influence the microstructure of as-built LPBF. The optimal parameters not only allow a reduction in the number of defects (pores, cracks) but also give a uniform microstructure. A finer microstructure can be obtained by optimizing the laser power, and it is highly beneficial for the resulting mechanical properties [25]. As reported by *Oliveira*, typical defects encountered are microsegregation, undesired texture, coarse columnar grains, and meta-stable phases such as martensite. The former issue can be solved either by increasing laser velocity or by strongly reducing it. The best practice for undesired texture and coarse/columnar grains is to lower laser speed or reduce laser power. While for the last problem, remelting is suggested under reduced laser power [13]. These downsides weaken the quality properties of the final part, and it is essential to avoid these defects to obtain a finer microstructure enhancing the mechanical properties.

#### 2.3.2.1 AISI 316L microstructure

Two main phases characterize LPBF-built SS316L parts: face-centered cubic (FCC) austenite ( $\gamma$  phase) and body-centered cubic (BCC) ferrite ( $\delta$  phase). Therefore there should be no martensitic phase if no strain is applied [42]. Figure 2.8 shows the general microstructural features observed by *Leicht* on 316L built samples. These are melting pool boundaries (MPB), high angle grain boundaries (HAGB), and hexagonal cell boundaries. Moreover, cell boundaries and nano-sized oxide particles

are always present, and their silicon and chromium concentration may contribute to the strength of the material [16].

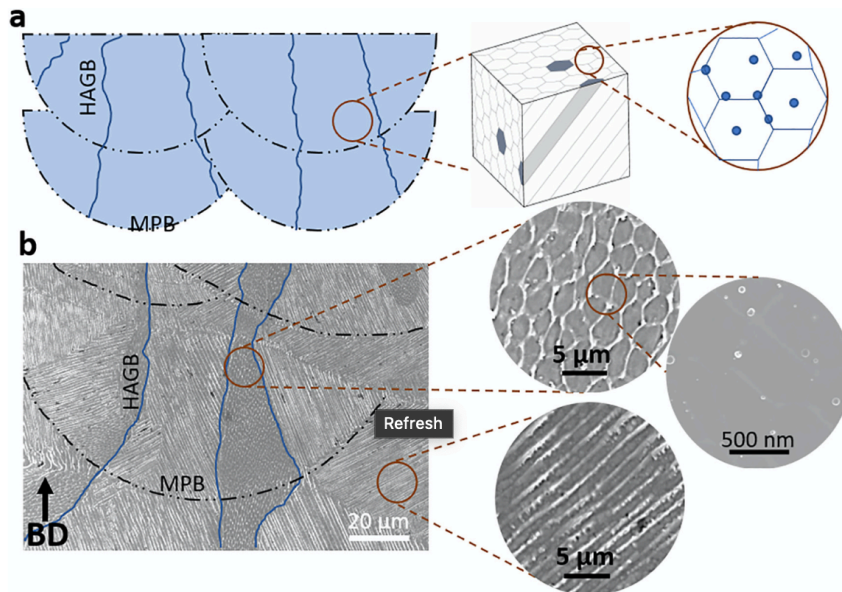


Figure 2.8: LPBF 316L microstructure general features [16]

*Leicht* reported that crystallographic orientation and grain size could be controlled by altering the volumetric energy density. The outlines of his research demonstrate that samples fabricated with the highest VED showed a firm  $\langle 101 \rangle$  texture along the building direction for the large, elongated grains. As VED decreased, the preferential orientation became weaker, and the grains became smaller. However, the sample fabricated with the lowest VED had small but elongated grains along the building direction with random texture [16]. *Eliasu* also analyzed the microstructure of AISI 316L built samples and observed two distinct microstructural features: cellular structures and columnar (or lathe) structures. The substructures became more distinct, increasing the laser power while keeping scanning speed and hatch spacing constant. The boundaries of the cellular and columnar structures evolved into thicker and well-defined ones as the laser power increased from 200 to 250 *W*. Thus, the higher power made the substructures more densely packed than they were in the sample with lower laser energy. In addition, the same effect arose, modifying scan speed from 750 to 1250 *mm/s* while laser power and hatch spacing remained constant. With lower scanning speeds, the boundaries increased in thickness, and tightly packed substructures were obtained. On the other hand, smaller hatch spacings created densely packed cellular structures while having a relatively sparse distribution of the columnar structures. The inverse effect appeared enlarging the hatch spacing, which resulted in a tightly packed columnar structure and a sparsely packed cellular structure. [43].

### 2.3.3 Porosity

Porosity is a common defect in metal AM parts and can negatively affect mechanical properties. Pores formed by processing technique, known as process-induced porosity, manifest in two distinct variations:

- Lack of fusion porosity is a combined effect that occurs when the applied energy is not sufficient for complete melting. It involves scan strategy, power, scan velocity, hatch distance, and layer thickness [13]. These pores are typically non-spherical and tend to be thin and of crescent shapes[44].

- Keyhole porosity comes from irregular melt pool dynamics. These defects are caused by gas entrapment in the solidified material. When the applied power is too high, the metal vaporizes, and spatter ejection may occur, creating gas bubbles that may become trapped. In such cases, round pores are observed. The key factors contributing to keyhole porosity are laser power and scan velocity. It is nearly unaffected by changes in layer thickness and hatch distances. Scan strategy can also affect the occurrence of this phenomenon. The general solution to avoid keyhole porosity is simply reducing laser power or increasing the scanning speed [13].

The Volumetric Energy Density strongly influences the total porosity: low VED values are associated with higher porosity due to increased unfused powder particles within the layers. Conversely, an increase in VED improves melting and the flow of the molten material, thus reducing the pores. Finally, if the energy density is too high, porosity increases again due to the keyhole effect. *Eliasu* found this relationship between porosity and VED while studying the microstructure of AISI 316L's built parts. Other studies outlined that the same evolution is also typical for other metallic alloys [9].

### 2.3.4 Densification behavior

The selection of the optimal set of processing parameters allows building parts with a density above 99%. Density appears to be negatively influenced when increasing the hatch distance and the vector scan size [15]. It also improves when laser power grows, while too high and too low scan speed values negatively affect density, especially when matched with high hatch spacings. Considering volumetric energy, the presence of a steady region between a minimum and a maximum level of VED, as shown in figure 2.9, indicates several optimal conditions available for processing the material.

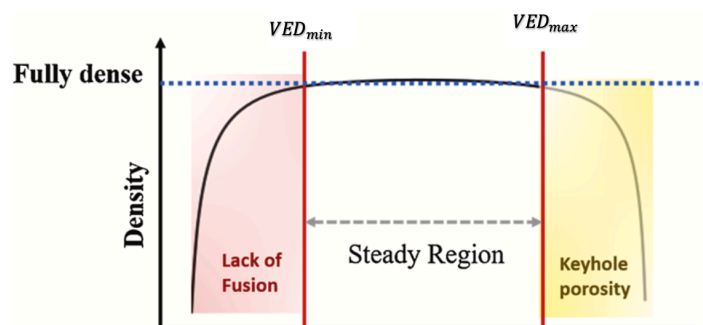


Figure 2.9: Density as a function of VED [9]

Thus, it is possible to choose different combinations of process parameters in the steady region, where the density content is high enough [9]. To this aim, Table 2.4 reports the VED values found by various researchers, which assure proper densification.

Table 2.4: VED ranges for optimal densification.

<b>Researcher</b>	<b>Machine</b>	<b>Material</b>	<b>Optimal VED for dense parts</b>
<i>Eliasu</i> [43]	EOS M280	316L	40 – 100 J/mm <sup>3</sup>
<i>Yakout</i> [45]	EOS M280	316L	62,5 – 104,2 J/mm <sup>3</sup>
<i>Cherry</i> [46]	AM250 Renishaw	316L	104,52 J/mm <sup>3</sup>
<i>Leicht</i> [11]	EOS M290	316L	37 – 65 J/mm <sup>3</sup>
<i>Leicht</i> [16]	EOS M290	316L	73,9 – 203,1 J/mm <sup>3</sup>
<i>Cacace</i> [9]	AM250 Renishaw	A357	85 – 140 J/mm <sup>3</sup>
<i>Read</i> [47]	Concept Laser M2	AlSi10Mg	60 – 75 J/mm <sup>3</sup>
<i>Brown</i> [48]	EOS M270	IN625	78 – 110 J/mm <sup>3</sup>
<i>Guo</i> [41]	Concept Laser M2	IN738LC	55 – 75 J/mm <sup>3</sup>
<i>Sun</i> [49]	DiMetal-280	Ti6Al4V	250 J/mm <sup>3</sup>
<i>de Formanoir</i> [7]	ProX DMP 320	Ti6Al4V	30,2 – 58,9 J/mm <sup>3</sup>

### 2.3.5 Mechanical properties

The analyses of the mechanical properties of LPBF designed components evidence that it is possible to produce high-strength alloys, even exceeding the performance of parts produced by traditional manufacturing methods. The mechanical characteristics of LPBF alloys are mainly due to the refined microstructure and the supersaturated solid solution obtained by the rapid solidification effect. A summary of the properties obtained according to the literature analyzed is reported in Table 2.5.

Table 2.5: Mechanical properties and Surface roughness characterization.

Researcher	Machine	Material	Property	Results
<i>Eliasu</i> [43]	EOS M280	316L	Hardness	208,7 - 241 HV
<i>Cherry</i> [46]	AM250	316L	Hardness	225 HV
			$R_a$	9 - 16 $\mu\text{m}$
<i>Leicht</i> [11]	EOS M290	316L	YS	460 - 540 MPa
			UTS	600 MPa
			E%	44 - 61 %
<i>Leicht</i> [16]	EOS M290	316L	UTS	525 - 575 MPa
			YS	452 - 483 MPa
			E%	33 - 52 %
<i>Slotwinski</i> [50]	-	316L	Young's Modulus	180 $\pm$ 25 GPa
			YS	521 $\pm$ 101 Mpa
			UTS	610 $\pm$ 80 MPa
			E%	32 $\pm$ 17 %
<i>Zheng</i> [51]	HRPM-II SLM	316L	Microhardness	255 HV
			UTS	321 - 722 MPa
<i>Liu</i> [52]	ProX DMP 320	316L	UTS	up to 707 MPa
			E%	30 - 55 %
<i>Cacace</i> [9]	AM250	A357	UTS	393 $\pm$ 7,4 MPa
			E%	10,5 $\pm$ 1,6 %
			YS	202,5 - 217,6 MPa
<i>Read</i> [47]	Concept Laser M2	AlSi10Mg	YS	240 - 275 MPa
			UTS	280 - 375 MPa
			E%	0,5 - 2,25 %
<i>Brown</i> [48]	EOS M270	IN625	Hardness	31.8 - 36,4 HRC
			Hardness	61.5 - 69,3 HRA
<i>Guo</i> [41]	Concept Laser M2	IN738LC	$R_a$	11,16 $\mu\text{m}$ - 21,1 $\mu\text{m}$
			UTS	300 -1200 MPa
			E%	3.5 - 11 %
<i>Sun</i> [49]	DiMetal-280	Ti6Al4V	Hardness	492 HV
<i>De Formanoir</i> [7]	ProX DMP 320	Ti6Al4V	Top $R_a$	4,16 $\pm$ 0,5 $\mu\text{m}$
			Side $R_a$	6,95 $\pm$ 0,2 $\mu\text{m}$
			Young's modulus	68 - 113 GPa
			YS	1016 - 1111 MPa
			E%	7,8 - 10,3 %

Mechanical tests on the produced parts highlight that the properties of LPBF processed parts strongly depend on the building parameters used during the process [20]. Density is a crucial factor for strength in LPBF parts that directly affect the mechanical properties of the products. Good mechanical properties can be achieved by reducing the porosity content below 1% [53]. *Guo* found that too high or too low  $v_s$  resulted in increased porosity on IN738LC built samples. Ultimate tensile strength (UTS), Young's modulus (E), microstructure, elongation at the break (E%), and yield strength (YS) depend on the layer thickness [14]. These properties tend to decrease concerning the increase of layer thickness. The main reasons for higher hardness and tensile properties are attributed to finer grain size, finer cellular microstructure, and the presence of well-distributed nano-sized sediments [54]. Despite this, Shi outlined that high layer thickness has a more significant influence on surface

roughness ( $R_a$ ) than tensile properties [55]. On the other hand, microhardness and tensile properties are also found to increase with increasing laser power [25]. The effects of process parameters on the produced parts are summarized in table 2.6.

Table 2.6: Effects of process parameters on the final quality of the product.

<b>Increase Scan Speed (<math>v_s</math>)</b>			
<b>Researcher</b>	<b>Machine</b>	<b>Material</b>	<b>Effect</b>
<i>Eliasu</i> [43]	EOS M280	316L	↑ porosity
			↓ density
<i>Liu</i> [52]	ProX DMP 320	316L	↓ Elongation to failure
<i>Read</i> [47]	Concept Laser M2	AlSi10Mg	↑ porosity
<i>Brown</i> [48]	EOS M270	IN625	↓ Hardness
<i>Guo</i> [41]	Concept Laser M2	IN738LC	↑ porosity (too high or too low $v_s$ )
			↑ Surface roughness
<b>Increase Laser power (<math>P</math>)</b>			
<b>Researcher</b>	<b>Machine</b>	<b>Material</b>	<b>Effect</b>
<i>Eliasu</i> [43]	EOS M280	316L	↓ porosity
			↑ density (P = 150 – 200 W)
<i>Yakout</i> [45]	EOS M280	316L	↑ density (for high $v_s$ )
			↓ density (for low $v_s$ and h)
<i>Zheng</i> [51]	HRPM-II SLM	316L	↑ Tensile Strength
			↑ Elongation
			~Microhardness
<i>Brown</i> [48]	EOS M270	IN625	↑ Hardness
<i>Guo</i> [41]	Concept Laser M2	IN738LC	↓ Surface roughness
			↓ porosity
<b>Increase hatch spacing (<math>h</math>)</b>			
<b>researcher</b>	<b>Machine</b>	<b>Material</b>	<b>Effect</b>
<i>Eliasu</i> [43]	EOS M280	316L	↑ porosity
			↓ density
<i>Brown</i> [48]	EOS M270	IN625	↓ Hardness
<i>Guo</i> [41]	Concept Laser M2	IN738LC	↑ porosity
			↑ Surface roughness
<b>Increase Layer Thickness (<math>z</math>)</b>			
<b>researcher</b>	<b>Machine</b>	<b>Material</b>	<b>Effect</b>
<i>Leicht</i> [11]	EOS M290	316L	↓ Yield strength
			↓ Elongation to fracture
			~ Ultimate tensile strength
			↑ Surface roughness
<i>Sun</i> [49]	DiMetal-280	Ti6Al4V	↓ density
<i>Badrossamay</i> [18]	Concept Laser M3	316L	↑ Surface roughness

### 2.3.5.1 Residual stress

Residual stresses are a common drawback of SLM as-built components since they typically result in part distortion, cracking, and delamination [56]. The residual stress profile generally consists of two zones of significant tensile stresses at the top and bottom of the part and a large zone of intermediate compressive stress in between [57]. The magnitude of residual stresses can reach values above 500 MPa [45], and without sufficient control, it can easily exceed the yield stress of the alloy. Standard methods to balance residual stresses include reducing the scan vector size, preheated substrates, and the use of sacrificial supports to restrain part deformation [13]

## 2.4 Process optimization methods

Once explained the goals, high process productivity and high-quality product, this section will discuss how to optimize the LPBF process considering both objectives. For this purpose, various effective methods are described as follows.

### 2.4.1 Layer thickness increase

The first method concerns increasing the powder layer thickness, and it is the most effective way to improve productivity. It not only allows rising the build rate by reducing the building time, but it also decreases the overall production time by lessening the recoater run. *Badrossamay* reported that it is possible to improve productivity from 20% to 25% only by applying a thicker layer within a specific threshold limit. Further enhancement could also be achieved by processing at scanning speeds higher than the default values. Still, in this case, attainable densities start to drop down since it would not be possible to obtain the same adequate melt pool [18]. The main drawback of the method, as outlined by *Leicht*, is that despite the remarkable enhancement in productivity, if the powder layer is too thick, several defects start to appear in the produced parts due to a lack of fusion related to a missing melting between layers. Moreover, such defects introduce stress concentration sites that can be detrimental in the case of dynamic loading [11].

### 2.4.2 VED method

The second approach to improve the build speed is the Volumetric Energy Density method, an effective optimization strategy, as demonstrated by many researchers [9], [16]. For a given material, a series of tests can determine the minimum applied energy required to achieve adequate material fusion for the desired material properties. Afterward, productivity can be maximized using the fastest combination of laser power, scan speed, and hatch distance for a particular machine layout [3]. From figure 2.10 to figure 2.13, the results found by *Eliasu* on AISI 316L are reported, evidencing the trend of VED versus porosity/density [43].

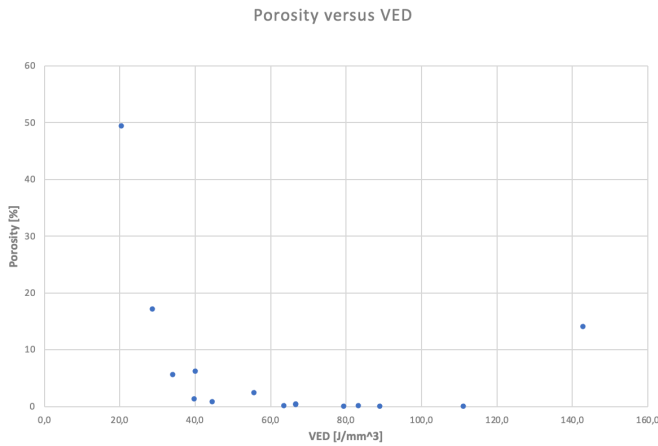


Figure 2.10: Porosity versus VED experimental result

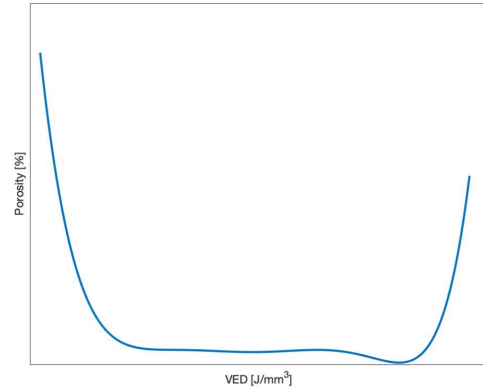


Figure 2.11: Porosity trend as a function of VED

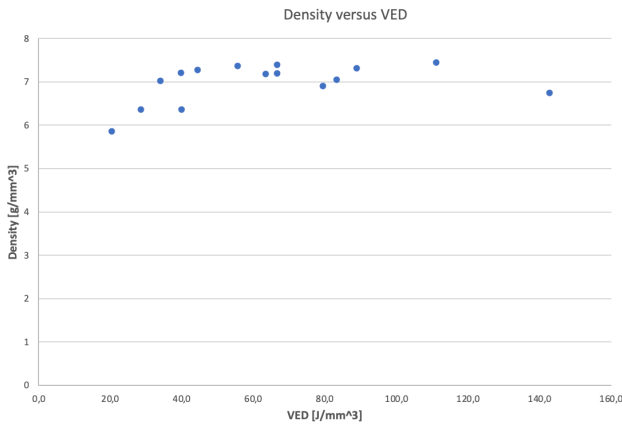


Figure 2.12: Density versus VED experimental results

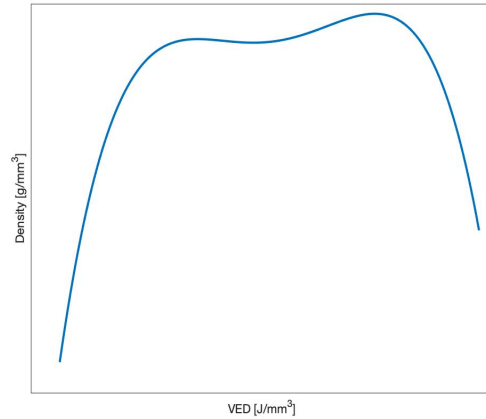


Figure 2.13: Porosity trend as a function of VED

By combining equations (2.4) and (2.6), it is possible to obtain the relation:

$$VED = \frac{P}{BR} \quad (2.15)$$

For a given laser power, BR maximization corresponds to VED minimization. Thus, the procedure allows identifying a combination of parameters to increase productivity while maintaining an acceptable density and pore content [9].

### 2.4.3 Taguchi and ANOVA analysis

The third option consists of the Taguchi Response Surface method. It involves the statistical analysis of variance (ANOVA), which has shown to be helpful to study the effect of many parameters. This method generally consists of 4 steps:

- 1) Select proper quality characteristics and process parameters according to experimental analysis.
- 2) Select the proper orthogonal array to conduct the experiments.
- 3) Analyze the experimental results using the S/N ratio and statistical analysis of variance (ANOVA)

4) Based on the analysis results, obtain the optimal process parameters (productivity criterion)

*Dzukey* used this method for the significance of SLM process parameters (laser power, scan speed, hatch spacing, and layer thickness) of AISI 316L on density [58]. Similarly, *Calignano* used the Taguchi method and ANOVA techniques to optimize the DMLS process of aluminum parts by studying the impact of the process parameters (laser power, scan speed, and hatch spacing) on surface roughness [20].

#### 2.4.4 Optimization algorithms and numerical modeling

Artificial Neural Network and Numerical Modeling, proposed by *Marrey* [14] and *Letenneur* [59], have proven to optimize the LPBF process while maintaining the quality goal. *Marrey* used an Artificial Neural Network (ANN) algorithm, which resulted in a complete understanding of the correlation between process parameters and part quality. This model was adopted to optimize process parameters and to achieve the desired properties. This study presents a framework for optimizing the PBF process by mapping the ultimate quality of a fabricated part into the process parameters. This correlation allows the creation of an intelligent neural network for parameters suggestion and build-time estimations. *Letenneur* proposed a simplified analytical model for the melt pool modeling of the LPBF process. This approach contributed to developing a density prediction approach that can be adapted for any given powder feedstock and LPBF system. The numerical analysis consisted of a thermal field model generated by a moving heat source on a solid body. This simulation was then exploited to determine the melt dimensions for the selected sets of printing parameters, demonstrating that it can reliably optimize the LPBF process. This approach was then validated for different alloys and processing conditions using literature data, thus demonstrating its potential for process optimization.

### 2.5 Case studies

In this final section, two case studies are reported; both were taken by the research work performed by *Leicht* on AISI 316L alloy.

#### 2.5.1 Case study n.1: Layer thickness increase

In this study, *Leicht* [11] provided a detailed microstructure characterization and a mechanical properties analysis for AISI 316L samples with 20  $\mu\text{m}$  and 80  $\mu\text{m}$  layer thicknesses, respectively, produced by adjusting the other process parameters ( $P = 220 \div 370 \text{ W}$ ;  $v_s = 800 \div 2100 \text{ mm/s}$ ,  $h = 0,09 \div 0,12 \text{ mm}$ ) and with a VED ranging from 19  $\text{J/mm}^3$  to 77  $\text{J/mm}^3$ . Two factors were evaluated to determine the process window: the build speed and the process stability. The process stability was assessed using the standard deviation of the grey values available in the EOS M290 system, linked to the melt pool intensities. A high standard deviation indicates a widespread of intensities and a less stable process. The standard deviation of the grey values was found to rise by increasing VED globally. The process becomes unstable for a VED greater than 50  $\text{J/mm}^3$ . The results suggest that parts can be fabricated four times faster with tensile strengths comparable to those obtained using standard process parameters. Both layer thicknesses achieved a density greater than 99.9%, but a lack of fusion defects in samples produced with an 80  $\mu\text{m}$  layer thickness was found.

#### 2.5.2 Case study n.2: VED density control method

To perform this analysis, *Leicht* [16] used an EOS M290 machine to produce AISI 316L samples. Laser power and layer thickness were kept constant, respectively equal to 195 W, and 0.02 mm. Hatch distance (0.06–0.12 mm) and scan speed (800–1400 mm/s) were varied to obtain different VEDs,

ranging between  $58.0 \text{ J/mm}^3$  and  $203.1 \text{ J/mm}^3$ . The results shown in figure 2.14 indicate that the highest build speed was obtained for the samples produced with the lowest VED ( $58.0 \text{ J/mm}^3$ ), resulting in a relative density of 98.7% and with a 20% faster built time compared to the samples produced with standard process parameters ( $v_s=800$ ,  $h=0,09 \mu\text{m}$ , and  $\text{VED} = 98.5 \text{ J/mm}^3$ ). On the other hand, samples produced with the highest VED ( $203.1 \text{ J/mm}^3$ ) had no positive effect on relative density compared to the standard and led to a 30% slower built time. The samples with a VED of  $73.9 \text{ J/mm}^3$  resulted to be the ones with the best trade-off between build time (10% faster) and relative density (99.8%).

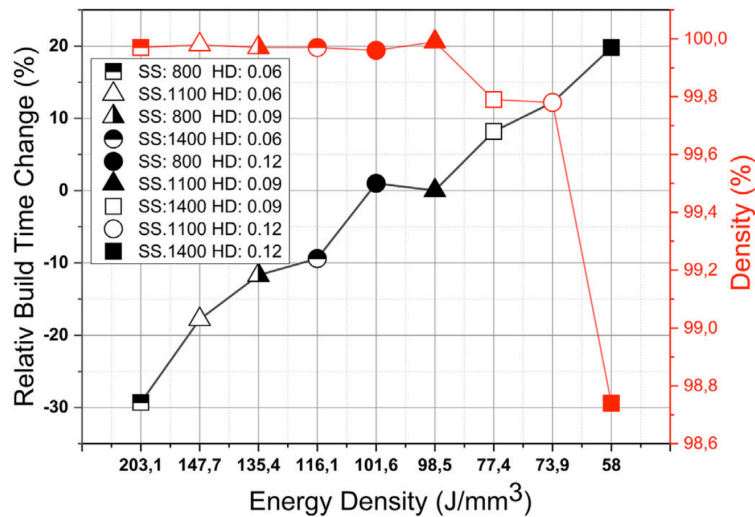


Figure 2.14: Graph of relative build time and density as a function of VED [16]

## 2.6 Conclusions

Additive manufacturing processes can produce complex parts with high quality and, at the same time, cut material waste. The capability of LPBF systems to process metallic alloys with good quality and enhanced productivity is reported in detail in this review. LPBF can reach optimal quality and mechanical properties in several metal alloys. However, productivity should be improved. The high production times needed to complete the process result in increased costs which limit its mass spreading. Up to now, several approaches have been used to balance mechanical properties and production time:

- Layer thickness increase
- VED Method
- Taguchi statistical approach
- Optimization algorithms and numerical modeling

These methods allow increasing productivity when compared to the traditional values while guaranteeing good quality properties. Respectively, each plan establishes a correlation between the process parameters and production time. The process optimization provides several parameters sets that accelerate the production by increasing hatch spacing, scan speed, and layer thickness without compromising the mechanical properties. Although changing the parameters proves to be effective, build rates are still low. Thus, further studies are needed to enrich the current know-how, providing a best practice to exploit high productive parameters. Furthermore, technology improvements should supply innovative hi-tech machinery capable of incrementing the current productivity features. In this context, the adoption of LPBF with optimized productivity will reflect substantial cost savings and

efficiency enhancement in every engineering application, from the biomedical industry to automotive production.



### ***3 Materials and methods***

The optimization of the LPBF process is a crucial activity that requires a considerable quantity of experimental data. Parameters such as laser power (P), scanning velocity ( $v_s$ ), hatch distance (h), and powder layer thickness (z) are the typical ones to be considered for this aim. Previous studies have demonstrated that various strategies can optimize processes to increase the part's mechanical properties concerning the production time.

One approach to investigating the relationship between final part properties and processing parameters is implementing different “trial” experimental tests. The volumetric energy density (VED) is used above all to describe such experimental data coming from LPBF tests.

A second possibility is the in-situ monitoring of the process, particularly suited for increasing the layer thickness and consequently reducing the overall production time.

Finally, numerical simulation can effectively support experiments by reducing the number of tests necessary for process parameter optimization.

Among those techniques, there is a great consensus in considering the increased layer thickness approach as the best way to enhance the productivity of the process. However, despite the considerable savings in terms of costs, a wrong process design leads to defects that have a detrimental effect on the mechanical properties of the printed parts. For example, the final products are generally affected by decohesion between layers and the lack of fusion imperfections. Furthermore, the mentioned deficiencies dramatically reduce Yield strength, Elongation to fracture, and ductility of the finished parts. These considerations have motivated the decision to perform the experimental activity adopting the volumetric energy density methodology. Indeed, as the literature suggests, VED is one of the best predictors for parts porosity in PBF processes.

The main goal of this study was the influence of high productive performances on the final product quality, in terms of relative density, porosity, surface roughness, and mechanical characteristics, then trying to establish a correlation between quality and productivity. This chapter discusses the experimental procedure adopted to reach this goal. In the first part, the LPBF machine used in the experiments is presented. Then, the auxiliary equipment used to characterize the coupons is further introduced in the corresponding section wherever it seems relevant. The second section covers material issues and talks about the material used to produce samples as well as its properties. Finally, the chapter will close by describing the methods used for the characterization of the pieces.

#### **3.1 Experimental equipment: Concept Laser Mlab R**

The samples used in this study were produced using a Concept Laser Mlab R, manufactured by GE, placed in the Integrated Additive Manufacturing (IAM) lab of the Politecnico di Torino. The system, presented in figure 3.1, can build fully dense parts with a formidable surface finish; thus, it is particularly appropriate for manufacturing metal components with elaborate structures.



Figure 3.1: Concept Laser Mlab R [32]

The machine's main feature is the physical separation of the process chamber and handling station, which offers the possibility of using the handling station for multiple devices [32]. The machine is equipped with a fiber laser with a maximum nominal power of 100W operating in continuous wave mode. The process is held under an inert atmosphere, thanks to high-purity nitrogen gas flow, which retains the oxygen content in the build chamber at below 0.1%. A complete list of nominal properties of the machine is reported in table 3.1.

Table 3.1: Properties of LPBF machine used in this work

Property	Value
Building envelope	90 x 90 x 80 [mm]
Layer thickness	15 – 30 [ $\mu\text{m}$ ]
Maximum scanning speed	7000 [mm/s]
Laser type & maximum power	CW- Fiber laser, [100 W]
Focus diameter	50 [ $\mu\text{m}$ ]
Build rate	1 – 5 [ $\text{cm}^3/\text{h}$ ]
Inert gas consumption	0.6 – 0.8 [l/min]

The process chamber is locked during operation while the laser fully melts the powder at the focusing point on the platform. Figure 3.2 shows the working chamber during the scanning of a set of samples.

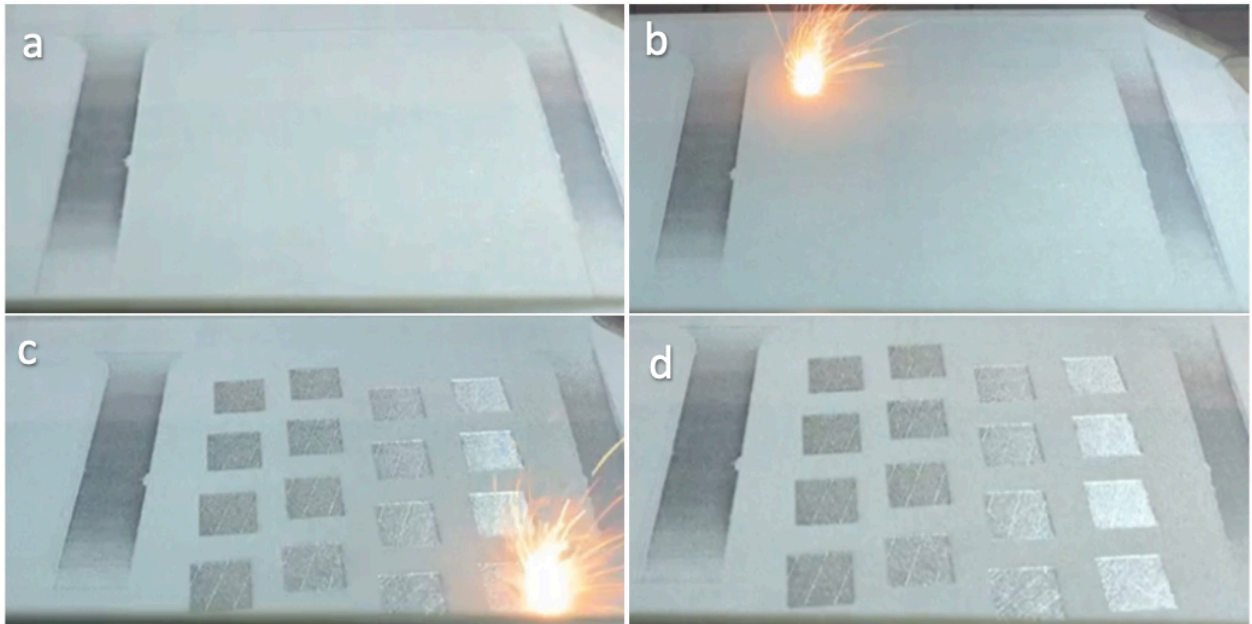


Figure 3.2: Images of the working chamber while processing a set of samples

### 3.2 Material: AISI 316L

In this study, twenty-four samples with different printing parameters were manufactured using 316L powder. The test samples were designed for nominal dimensions of  $10 \times 10 \times 10 \text{ mm}$ ; hence the dimension parallel to the building direction was enlarged with an offset of  $0,5 \text{ mm}$  to account for the loss of material due to the samples cutting from the building plate via Electrical Discharge Machining (EDM). In addition, a label indicating the sample's number was added above each top surface to distinguish the coupons. Figure 3.3 shows the building plate with the printed pieces after the removal from the working chamber.

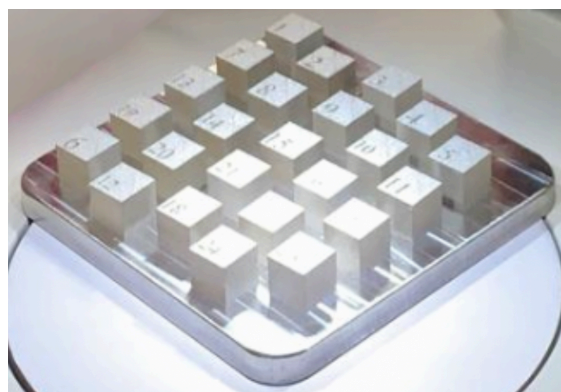


Figure 3.3: The twenty-four cubic samples at end of the printing step

Stainless Steel AISI316L is an austenitic iron-based alloy resistant to corrosion. It is a material that can be used in various industrial applications such as aerospace, automotive, and biomedical. The feedstock powder was produced using the Gas Atomized manufacturing process, with a size distribution of  $15\text{-}50 \mu\text{m}$ , and it was dried for 1 hour at the constant temperature of  $80 \text{ }^\circ\text{C}$  before being processed. The carbon content below  $0.03\%$  and the presence of the molybdenum alloy element effectively limit the tendency to corrosion. The complete chemical composition of the starting powder is reported in table 3.2.

Table 3.2: Chemical composition of 316 stainless steel powder as reported by EOS [30]

Element	Composition [wt%]
Fe	Balance
Cr	17,00 – 19,00
Ni	13,00 – 15,00
Mo	2,25 – 3,00
C	0,03
N	0,10

### 3.3 Design of experiments (Doe): process parameters selection

For this study, a Design of Experiments (DOE) approach was used. The experiments aim to identify a window of VED’s values generating the best results in terms of porosity, reaching an acceptable density value into the sample higher than 98%.

The process parameters selected to examine the influence of energy density on mechanical properties were laser scan velocity and hatch distance. Instead, layer thickness and laser power remained unaltered. The first one was set at the optimum value of 25  $\mu\text{m}$ , while the second was kept constant at the highest level of 95 W. The other three parameters were varied by selecting six levels of scanning speeds (Lowest: SSLT, Low: SSL, Moderate: SSM, High: SSH, Very High: SSVH, and Maximum: SSMM) and four levels of hatch distances (Low: HDL, Moderate: HDM, High: HDH, and Very High: HDVH). A summary of the parameters’ terminology and the constant values adopted is reported in table 3.3.

Table 3.3: Process parameters investigated in this experimentation

Varied parameters		Fixed parameters	
Hatch distance	HDL, HDM, HDH, HDVH [ $\mu\text{m}$ ]	Laser power	95 [W]
Scanning speed	SSLT, SSL, SSM, SSH, SSHT, SSMM [ $\text{mm/s}$ ]	Layer thickness	25 [ $\mu\text{m}$ ]

The samples were produced using a stripe scanning strategy, in which each layer was processed by shifting the laser direction by 67° from one layer to the other. The graphical representation of the scanning strategy is shown in Figure 3.4.

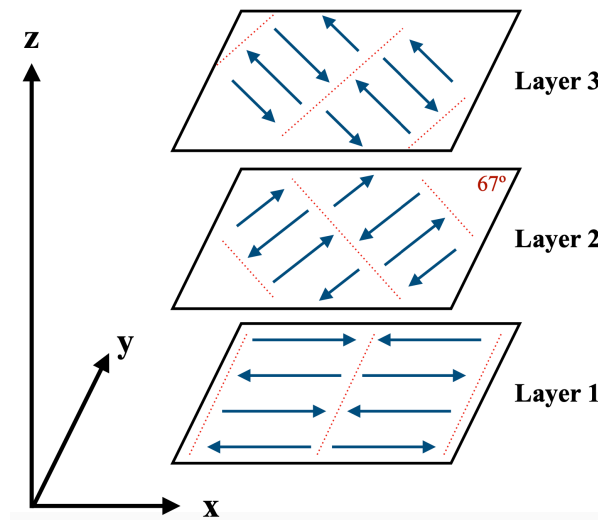


Figure 3.4: 67° stripe scanning strategy

Starting from the above-stated ranges of parameters, the samples were sorted based on the volumetric energy density (VED), described by equation (2.4). Non-optimal VED values lead to unfavorable results such as partially melted particles, inhomogeneous melt track, vaporization phenomenon, and lack of fusion impurities. The VED ranged from 36,54 to 102,70  $J/mm^3$ , which defined the confined window of experimentation. This range of energy densities is comparable with the levels selected in the literature. All the possible combinations using varying process parameters and the resulting VED value are shown in table 3.4.

Table 3.4: Combination of process parameters used in this study

Sample ID	$P$ [J]	$v_s$ [mm/s]	$h$ [mm]	$z$ [mm]	VED [ $J/mm^3$ ]
1	95	SSH	HDVH	0,025	45,67
2	95	SSLT	HDL	0,025	102,70
3	95	SSMM	HDL	0,025	51,35
4	95	SSM	HDH	0,025	57,75
5	95	SSHT	HDH	0,025	44,92
6	95	SSHT	HDM	0,025	50,26
7	95	SSLT	HDM	0,025	90,48
8	95	SSL	HDVH	0,025	60,90
9	95	SSMM	HDVH	0,025	36,54
10	95	SSM	HDM	0,025	64,63
11	95	SSH	HDM	0,025	56,55
12	95	SSHT	HDVH	0,025	40,60
13	95	SSHT	HDL	0,025	57,06
14	95	SSLT	HDH	0,025	80,85
15	95	SSL	HDH	0,025	67,38
16	95	SSMM	HDH	0,025	40,43
17	95	SSM	HDVH	0,025	52,20
18	95	SSH	HDL	0,025	64,19
19	95	SSL	HDL	0,025	85,59
20	95	SSLT	HDVH	0,025	73,08
21	95	SSH	HDH	0,025	50,53
22	95	SSL	HDM	0,025	75,40
23	95	SSMM	HDM	0,025	45,24
24	95	SSM	HDM	0,025	64,63

As a second step, each sample's predicted build rate values were computed starting from equation (2.8) and converting the data in cubic centimeters per hour to obtain a more functional unit of measurement. Those results are reported in Table 3.5.

Table 3.5: Predicted build rates for the different samples

Sample ID	$v_s \left[ \frac{mm}{s} \right]$	$h [mm]$	$z [mm]$	$BR \left[ \frac{cm^3}{h} \right]$
1	SSH	HDVH	0,025	7,49
2	SSLT	HDL	0,025	3,33
3	SSMM	HDL	0,025	6,66
4	SSM	HDH	0,025	5,92
5	SSHT	HDH	0,025	7,61
6	SSHT	HDM	0,025	6,80
7	SSLT	HDM	0,025	3,78
8	SSL	HDVH	0,025	5,62
9	SSMM	HDVH	0,025	9,36
10	SSM	HDM	0,025	5,29
11	SSH	HDM	0,025	6,05
12	SSHT	HDVH	0,025	8,42
13	SSHT	HDL	0,025	5,99
14	SSLT	HDH	0,025	4,23
15	SSL	HDH	0,025	5,08
16	SSMM	HDH	0,025	8,46
17	SSM	HDVH	0,025	6,55
18	SSH	HDL	0,025	5,33
19	SSL	HDL	0,025	4,00
20	SSLT	HDVH	0,025	4,68
21	SSH	HDH	0,025	6,77
22	SSL	HDM	0,025	4,54
23	SSMM	HDM	0,025	7,56
24	SSM	HDM	0,025	5,29

The resulting combinations for each sample in terms of VED and BR, obtained by varying the process parameters, are shown in figure 3.5.

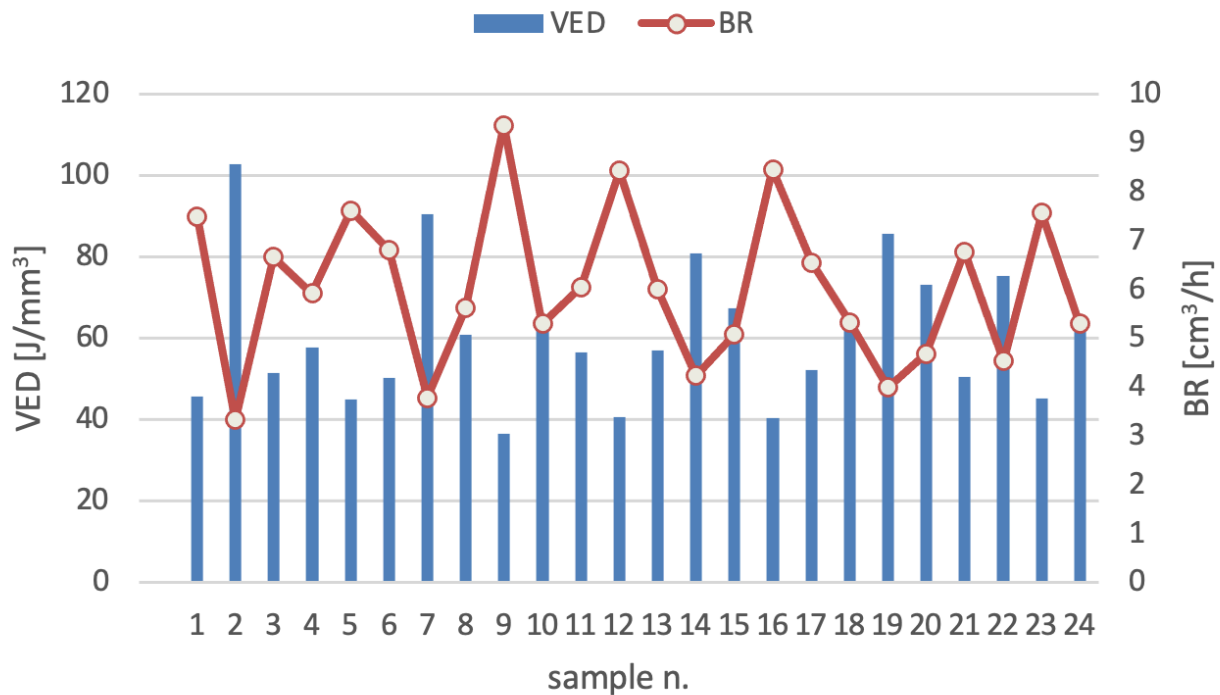


Figure 3.5: VED and BR parameters for each sample

### 3.4 Samples characterization

The design parameters discussed in the previous section were used to examine the influence of energy density on density, porosity, superficial features, surface roughness, and mechanical properties. The samples were cut from the building platform and furtherly analyzed in as-built conditions. This section underlines the methodology used for characterizing the pieces and the selection adopted to outline particular sets of samples.

#### 3.4.1 Surface morphology

The printed cubes were examined under an optical microscope to analyze the surface microstructural features. The apparatus used to perform this analysis was a Leica stereomicroscope, which is presented in figure 3.6.

Three different magnifications (1x, 2x, and 5x) were adopted, and seventy-two pictures were taken. All the adjustments of the optical microscope, as well as images magnifications, and picture capturing, were managed, on a connected personal computer, by special software offered by Leica corporation for the case-specific microscope



*Figure 3.6: Leica Stereomicroscope*

### **3.4.2 Dimensional accuracy**

The dimensional accuracy was measured employing a vernier caliper. The three dimensions of every cube were measured to check if distortions were detected with respect to the design dimensions for the cubes.

### **3.4.3 Surface roughness characterization**

The roughness analysis was performed utilizing an RTP 80 tester, presented in figure 3.7. The apparatus has two main units: the touchscreen display, which allows the operator to set the measurement parameters, and the measurement translator equipped with a roughness probe directly in touch with the surface to be characterized. The equipment is connected to a computer via a specific software which allows downloading measurements and profiles

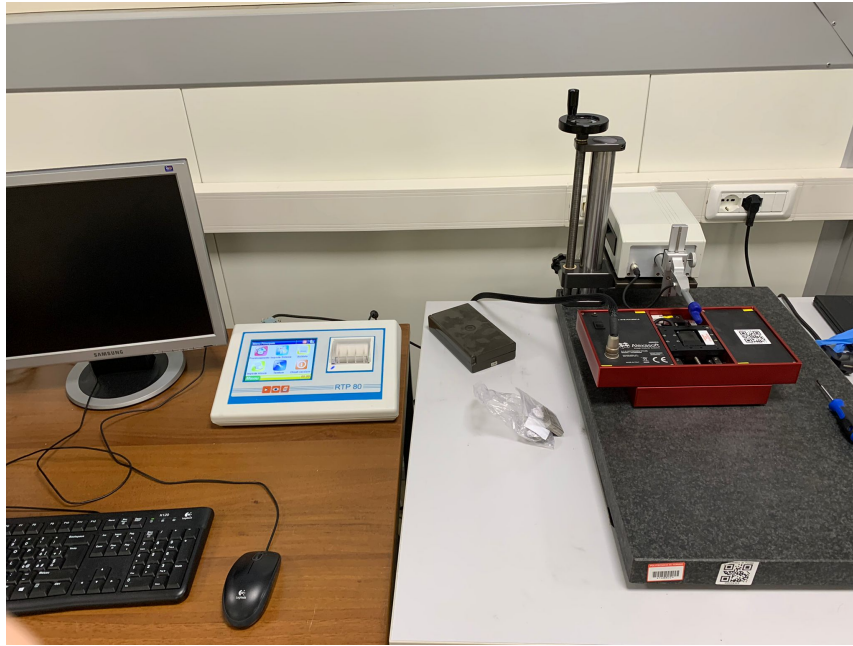


Figure 3.7: RTP 80 roughness tester

The methodology of measurement followed the UNI EN ISO 4227.  $R_a$  and  $R_z$  parameters were calculated on a filtered profile.  $R_a$  is the average roughness of a surface, while  $R_z$  represents the vertical distance between the highest peak and the deepest valley of the profile. The filtration operation calculates a profile that contains the longest wavelengths; such profile is the waviness. To properly set the parameters for the filtration operation, the cutoff and evaluation length were chosen as foreseen by the UNI EN ISO 4288:2000 standard reported in Table 3.6.

Table 3.6: recommended cutoff (UNI EN ISO 4288:2000)

Profile		Cutoff	Evaluation length
$R_z$ [ $\mu m$ ]	$R_a$ [ $\mu m$ ]	$\lambda$ [mm]	$E_l$ [mm]
Up to 0,1	Up to 0,02	0,08	0,4
0,1 – 0,5	0,02 – 1	0,25	1,25
0,05 – 10	1 – 2	0,8	4
10 – 50	2 – 10	2,5	12,5
50 – 200	10 – 80	8	40

Accordingly, for the as-built samples, the cutoff was set at 0,8 mm, the cutoff number was set equal to 5, and the corresponding evaluation length was 4 mm. Moreover, it was possible to initialize the cutoff velocity and the maximum amplitude from the roughness tester. These two parameters were put equal to 0,5 mm/s and  $\pm 600$  mm respectively.

After the system initialization, three measurements of  $R_a$  and  $R_z$  were taken (one at the left, one at the middle, and the last at the right) for five faces of the cubic sample. The primary profile, waviness, and roughness profile were extrapolated using the profilometer. The face where the pieces were cut was excluded from the measurements. Finally, the roughness results were averaged, and the standard deviations were computed.

### 3.4.4 Measurement of density and porosity

Archimedes method was applied to measure the density for each coupon. The principle states that a body immersed in fluid indicates an apparent loss in weight equal to the mass of the fluid it displaces. In this experiment, the weights were measured using an electronic scale equipped with a beaker for the measurements in water. The samples were weighed in air ( $m_{air}$  in  $g$ ) and then in water ( $m_{water}$  in  $g$ ) with a known density ( $\rho_{water} = 0,997 \text{ g/cm}^3$ ). The weight in water was furtherly averaged by computing the mean after three measurements. The Archimedes density ( $\rho_{Archimedes}$  in  $g/cm^3$ ) was calculated as follows:

$$\rho_{Archimedes} = \rho_{water} \cdot \frac{m_{air}}{m_{air}-m_{water}} \quad (3.1)$$

Then, the relative density ( $\rho_{relative}$  in  $g/cm^3$ ) for each sample can be determined as the ratio of the Archimedes density to the known theoretical density for the AISI 316L alloy ( $\rho_{theoretical} = 7,98 \text{ g/cm}^3$ ):

$$\rho_{relative} = \frac{\rho_{Archimedes}}{\rho_{theoretical}} \cdot 100 \quad (3.2)$$

Total porosity was computed starting from the bulk density, using the following formula:

$$\rho_{bulk} = \rho_{water} \cdot \frac{m_{air}}{m_{wet}-m_{water}} \quad (3.3)$$

Where  $m_{wet}$  is the average weight of every sample after the water immersion. For each piece, the wet weight measurement was performed three times. With these parameters, the porosity level can be computed, and it corresponds to:

$$Porosity \% = \frac{\rho_{theoretical}-\rho_{bulk}}{\rho_{theoretical}} \cdot 100 \quad (3.4)$$

The final report in terms of relative total porosity is presented in table 3.7.

Table 3.7: Relative density and porosity computations from Archimedes method

Sample ID	Archimedes Density [g/cm <sup>3</sup> ]	Relative Archimedes Density [%]	Porosity [%]
1	7,527	94,33	5,92
2	7,923	99,29	0,66
3	7,615	95,43	4,61
4	7,726	96,81	3,48
5	7,361	92,25	8,31
6	7,637	95,70	4,37
7	7,942	99,52	0,50
8	7,849	98,36	1,71
9	7,181	89,98	12,19
10	7,897	98,96	1,94
11	7,608	95,34	4,85
12	7,346	92,06	8,86
13	7,803	97,78	2,29
14	7,925	99,31	0,71
15	7,870	98,62	1,39
16	7,314	91,65	9,48
17	7,593	95,15	4,93
18	7,841	98,26	1,79
19	7,937	99,46	0,60
20	7,873	98,66	1,39
21	7,630	95,61	4,42
22	7,903	99,04	1,05
23	7,529	94,35	5,97
24	7,815	97,93	2,07

### 3.4.5 Mechanical characterization: tensile testing

The final mechanical characterization was performed employing the tensile test. Within the steady region of the Porosity – VED plot, in which pores percentage remains constant regardless of the VED, two samples resulting in superior and similar characteristics were identified. Therefore, the two sets of parameters used to fabricate those cubes were selected to test if the resulting static mechanical properties were comparable, even though the differences in energy densities. To this aim, such parameters were used to fabricate six tensile specimens, three for each set. Figure 3.8 presents a drawing of a tensile bar manufactured for the mechanical test.

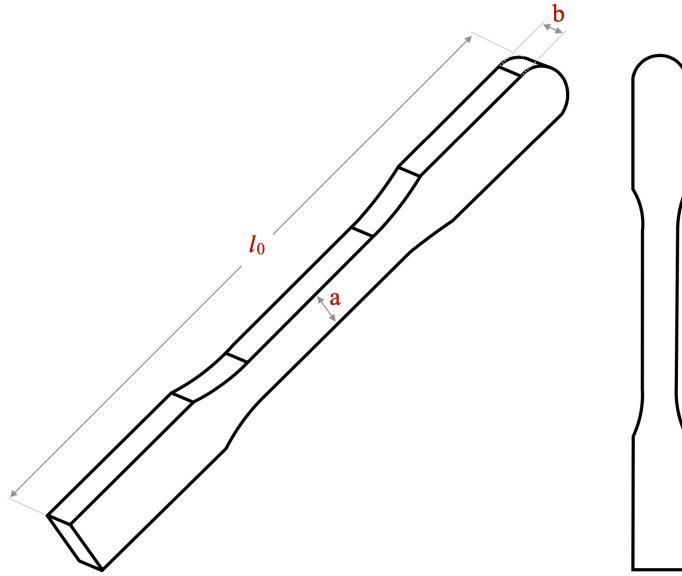


Figure 3.8: Schematic overview of sample a tensile specimen

The mechanical characterization was conducted at room temperature using a tensile test machine with a mobile crossbar velocity of  $2 \text{ mm/min}$ . During the tensile test, the applied force and the displacement were measured. After the elaboration, the stress and strain results were computed. The specimens were finally specified in terms of yield strength, ultimate tensile strength, and elongation to fracture.

## ***4 Results and discussions***

LPBF can process multiple feedstock powders to produce engineering parts. This characteristic makes this technology one of the most innovative. Furthermore, it makes it possible to fabricate novel alloys with different compositions by exploiting a wide range of adjustable parameters. However, the high number of variables interfering with the production activity requires a detailed framework to respect the highest quality while guaranteeing the lowest labor duration. This thesis aims to find a scheme covering both requirements; the State of Art suggested following a specific roadmap to achieve this objective. Indeed, the above-mentioned roadmap allowed to build small cubes, each one with a particular group of input parameters. The trial samples obtained following this procedure were analyzed to select the most promising set for the final part production.

This chapter discusses the analysis performed during the experiments providing the results obtained by showing graphs and reporting numerical values. A large amount of data emerged from this process; thus, the main findings are directly presented in the following section, while the appendix contains the remaining ones.

The structure of the subsequent paragraphs will be as follows:

- a) Analysis of the effects of process parameters on density and porosity; it includes three main parts related to the impact of single process parameters, combined effects of process parameters, and their influence on productivity.
- b) Surface quality analysis; it discusses dimensional accuracy and roughness.
- c) Mechanical testing of the specimens printed with the most promising parameters in terms of quality and productivity.
- d) Cost analysis for LPBF manufactured components.

### **4.1 Analysis of the effects of single process parameters on relative density and porosity**

Density and porosity estimations were taken exploiting the Archimedes principle. It is important to note here that Archimedes' methodology is not the most reputable way of determining the density of the printed parts. For example, pores are counted to determine the part's mass despite being filled with unmolten powders that do not entirely bind with the rest of the structure [43]. Moreover, particular care must be taken to avoid bubbles formation around surfaces of the parts, given that air bubbles deflate the weight in water, lowering the density of the solid. Nevertheless, the measurements were taken according to these considerations, paying particular attention to details; Figures 4.1, 4.2, and 4.3 illustrate the results graphically.

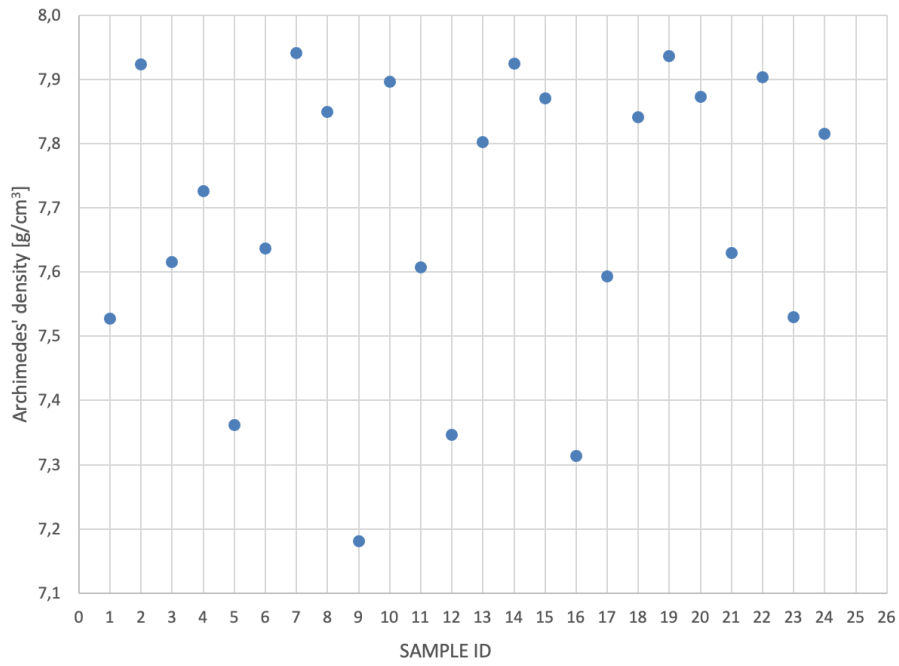


Figure 4.1: Archimedes' density results

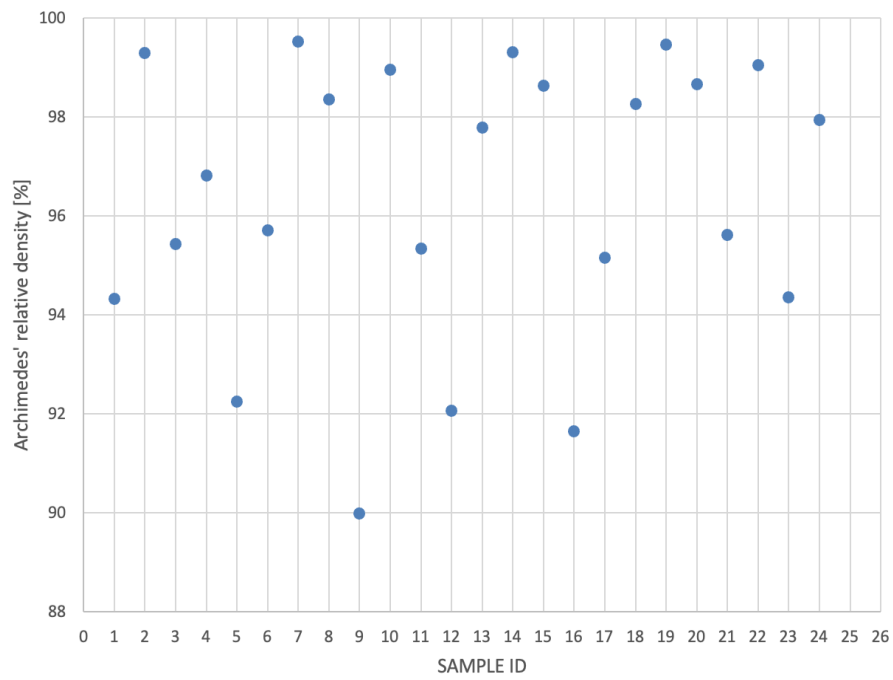


Figure 4.2: Archimedes' relative density results

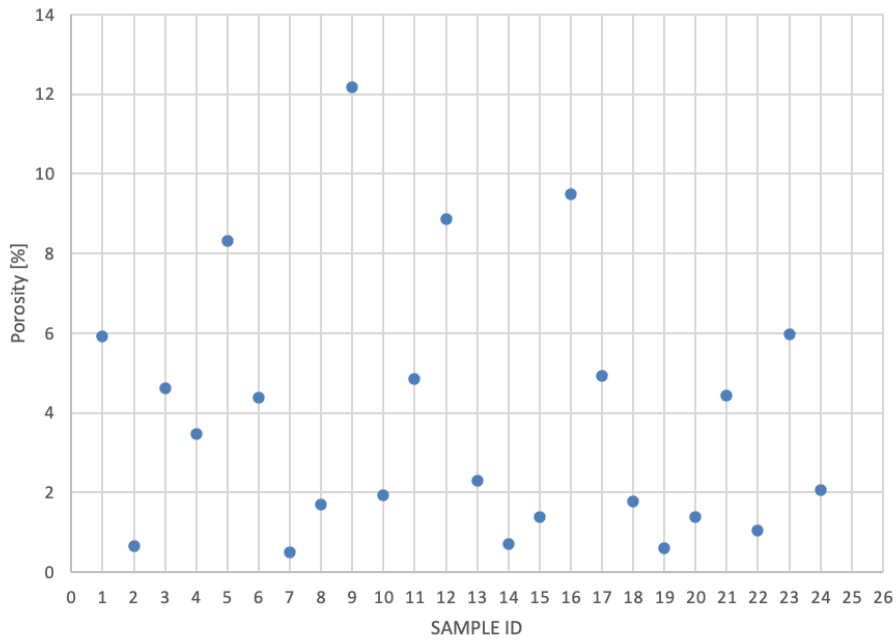


Figure 4.3: Porosity results

Sample 19 registered nearly full dense characteristics, with a relative density of 99,46% and a porosity equal to 0,60%. On the other hand, the worst densification quality, namely 89,98% in relative density and 12,19% in porosity percentage, characterized sample 9. The following paragraphs will analyze a complete discussion regarding the influence of scanning speed and hatch distance on densification and porosity results. It is necessary to underline that these parameters interact with each other, and often they need to be wisely adjusted to guarantee competitive productivity while ensuring good quality properties.

#### 4.1.1 Influence of scanning speed on density

Scanning speed is a fundamental process parameter since it influences the final part quality and the construction speed. Figure 4.4 shows the relative density data as a function of scanning speed (varying from SSLT to SSMM) for different levels of hatch distance (from HDL to HDVH).

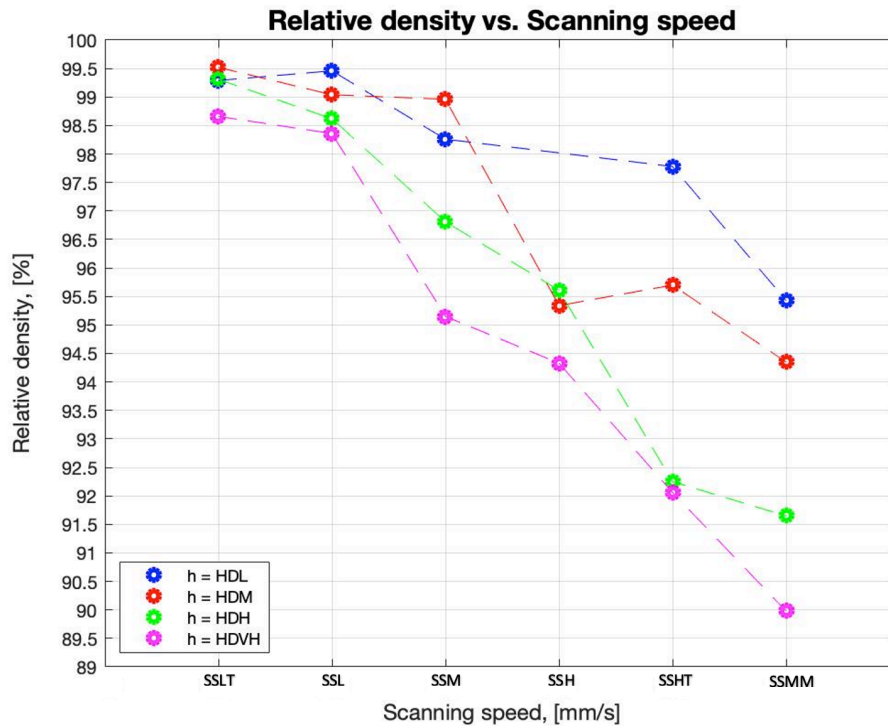


Figure 4.4: Densification behavior as a function of scanning speed

The highest relative density is 99,50 % ( $7,98 \text{ g/cm}^3$ ), recorded for sample 7, while sample 9 is characterized by the lowest relative density value of 89,98% ( $7,18 \text{ g/cm}^3$ ). The highest and lowest relative density results were registered for the lowest (SSLT) and maximum (SSMM) scanning speeds, respectively. Overall, an increase in the scanning speed leads to a reduction in relative density. If the scan speed is too high, scan tracks cannot fully melt, resulting in an inhomogeneous surface characterized by several voids that are detrimental to the densification behavior. As shown by the violet path (HDVH) in figure 4.4, if the scanning speed is increased from SSLT for sample 20 to SSMM for cube number 9, this would drop density from 98.66% to 89,98%, corresponding to a global deterioration by the 8,80%. From a local point of view, still considering the violet path and keeping it constant the hatch distance, a 16,7% increase in scanning speed, from SSL in sample 8 to SSM in sample 17, led to a 3,3% reduction in part density. However, a restricted improvement in densification can be discovered in few cases when scanning speed changes from SSLT to SSL for HDL (blue path, figure 4.4) and from SSH to SSHT for HDM (red way, figure 4.4). This unexpected behavior justifies the fact that scanning speed can be, in some cases, increased when having low values of hatch distance. In fact, since scan tracks are mainly overlapped for low hatch spacing values, a faster speed can nicely melt the powder, obtaining a packed part.

#### 4.1.2 Influence of hatch distance on density

Density sensitivity on hatch distance can be observed in figure 4.5, which displays the relative density as a function of the hatch distance for different levels of scanning speeds. In general, there is a consistent negative correlation to part density when increasing hatch spacing. This effect is particularly evident when hatch spacing increases under very high scan speeds. At the same time, it is less apparent when the laser dwells on the powder slowly, sometimes resulting in beneficial effects.

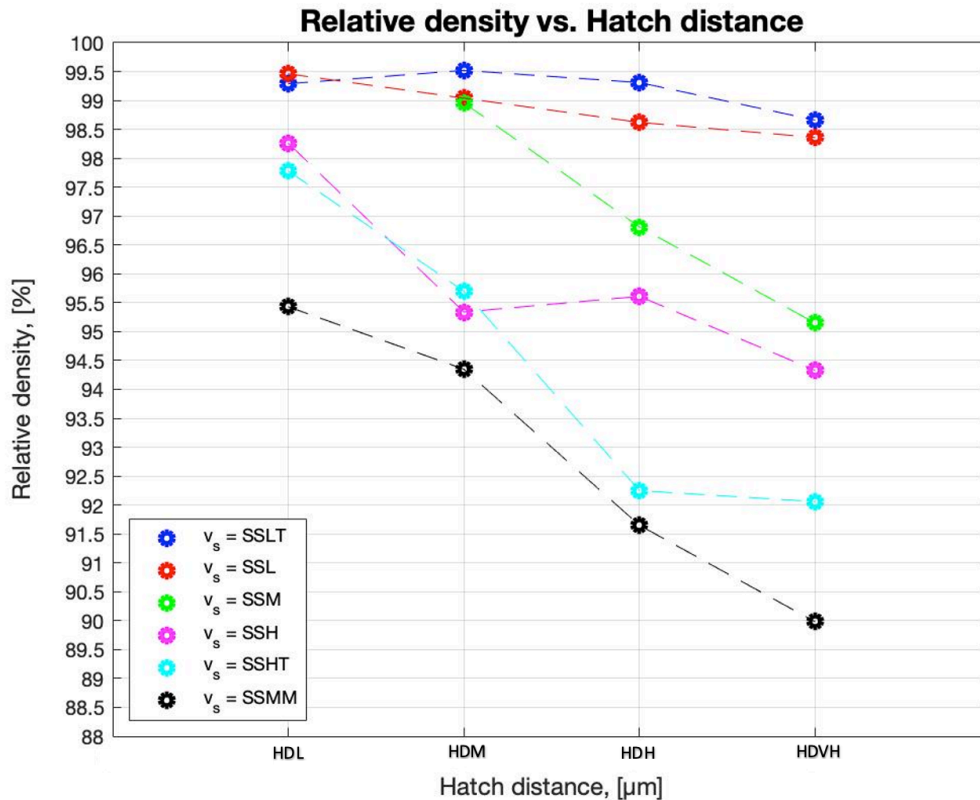


Figure 4.5: Densification behavior as a function of hatch distance

As shown by the black path (SSMM) in figure 4.5, an increase in hatch spacing from HDL to HDVH (40,54%) is responsible for a 5,71% decrease in part density from 7,61  $g/cm^3$  (sample 3) to 7,18  $g/cm^3$  (sample 9). Furtherly, considering the light blue path in figure 4.5, when a SSHT is used, an 11,9% increase in hatch spacing (from HDM to HDH) produces a 3,6% reduction in part density, as evidenced by samples 6 and 5. However, a benefit is visible when increasing hatch spacing from HDL to HDM and from HDM to HDH for samples undergoing a laser scan speed of SSLT (blue path, figure 4.5) and SSL (red trail, figure 4.5), respectively. The obtained results denote that high hatch spacings are mostly linked to lower densities than samples with small hatch spacings. This trend occurs because when the tracks' overlap is insufficient, there is a high probability of the laser missing areas between tracks, generating irregular surfaces.

#### 4.1.3 Influence of scanning speed on porosity

Density by itself is not sufficient to correctly characterize the manufactured samples. To this aim, a porosity analysis is helpful to describe the most typical resulting defects. As figure 4.6 reveals, porosity tends to increase when scanning speed increases, except for few cases where the porosity showed a rather unpredicted improvement. In addition, given the same scan speed incrementation, the higher the hatch distance is, the lower the porosity becomes. For example, sample 9 is characterized by the highest porosity percentage of 12,19% with a scanning speed of SSMM. In contrast, the lowest porosity can be spotted in sample 7, produced with a scanning speed of SSLT.

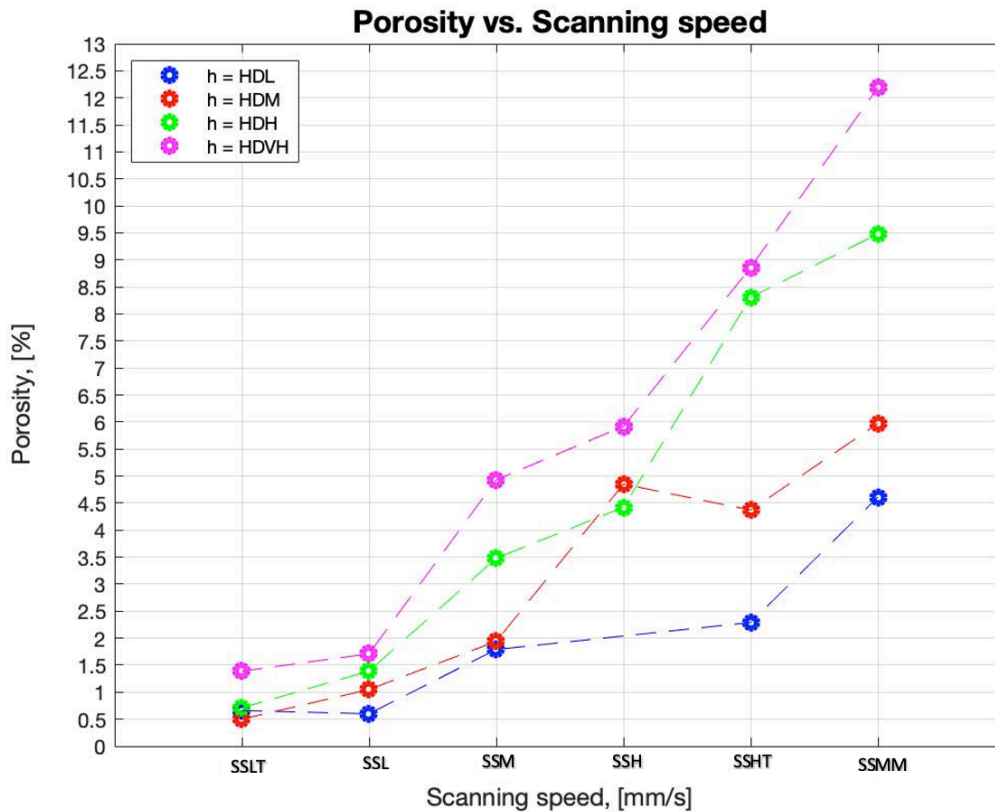


Figure 4.6: Porosity as a function of scanning speed

Scanning speed and porosity are deeply correlated. As a result, pores vary depending on velocity. The most common pores in LPBF manufactured parts are keyhole pores and lack of fusion. Keyhole pores are spherically shaped and small, whereas lack of fusion ones are more significant in size with an irregular shape. Keyhole pores are generated at slow scanning speeds from gas particles trapped within the melt pool. Instead, the lack of fusion porosity is due to the rapid solidification of the metal without completely filling the gaps between particles.

Figure 4.7 reports the stereomicroscope picture of the surface for three different samples with a magnification of x3. It shows the surface porosity evolution with increased scanning speed values when the hatch spacing was kept constant at HDL. The first picture (sample 19) does not display many pores; however, a diagonal defect can be spotted, probably due to the low values of hatch spacing and scan speed used. Pictures 4.7.b and 4.7.c (samples 18 and 13, respectively) display a growing number of surface pores. Such undesired texture characteristics may be limited by decreasing the laser velocity.

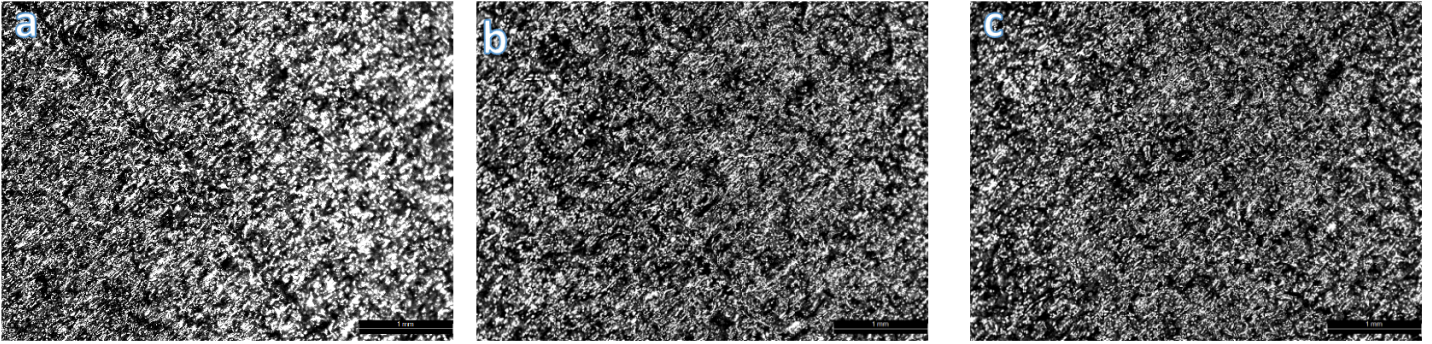


Figure 4.7: Evolution of pores with scanning speed and with a constant hatch distance: (a) SSL, (b) SSM, and (c) SSHT.

#### 4.1.4 Influence of hatch distance on porosity

For the final step of the parameter sensitivity investigation, the influence of hatch spacing on porosity (Fig. 4.8) is investigated.

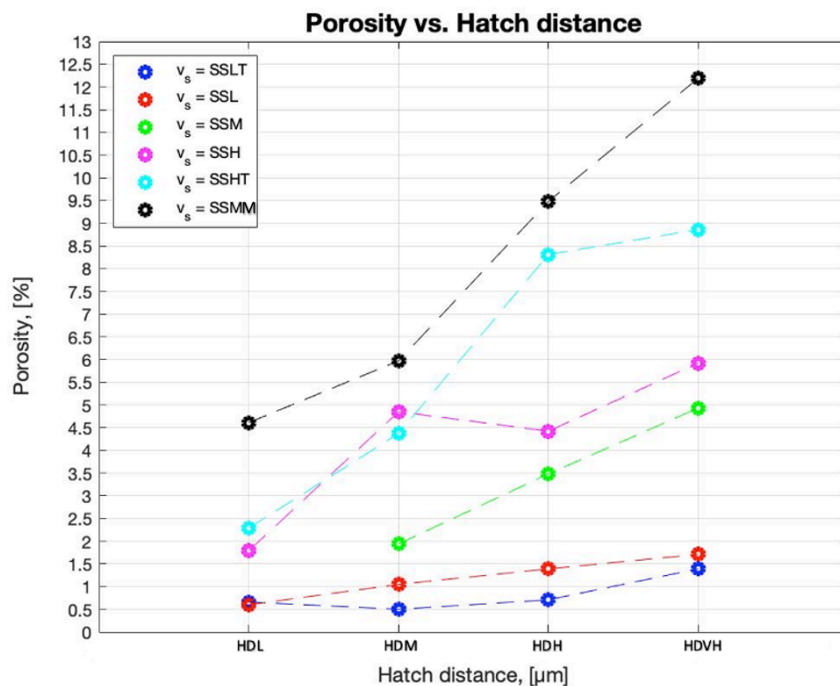


Figure 4.8: Porosity as a function of hatch distance

At a constant scanning speed SSMM (black path in figure 4.8), a 40% increase in hatch spacing from HDL to HDVH results in a 182,8% increase in porosity (4,61% for sample 3 and 12,19% for sample 9). A 90,2% increase in porosity was also observed when hatch spacing was varied from HDM to HDH in samples 6 and 5 while maintaining the laser speed constant at SSHT (light blue path in figure 4.8). However, a decrease in porosity was observed when hatching spacing increases from HDL to HDM under SSLT (blue way in figure 4.8) and when the laser speed is kept constant at SSL (red path in figure 4.8) while the hatch spacing is increased from HDM to HDH. In summary, increasing the hatch spacing leads to an increase in porosity. Also, the higher the scanning speed level, the higher the porosity.

A further central point to highlight is that hatch spacing identifies the physical properties of the melt pool dynamics. If the scan spacing is small, each layer appears smooth due to the high overlap between adjacent melt pool tracks. According to the results obtained, HDL and HDM hatch spacings result in an enhanced overlapping degree between scanning tracks for a better fusion of powder particles and reduced porosity percentage. As the scanning spacing increases, each layer becomes irregular because of significant gaps between adjacent laser marks. However, the solidity of the part could decrease when there are too many overlaps due to the recurrent energy provided to the powder. For this rationale, samples made with small hatch spacings are highly susceptible to the formation of keyhole pores when the scanning speed is low enough. Furthermore, the gas trapped between the powder induces this kind of pores, which finally are detrimental for what densification concerns. Figures 4.9 and 4.10 show the surface porosity evolution for series of samples obtained at low scanning speeds and increasing the hatch distance. The surface pores are mainly spherical for low hatch spacings, while their shape becomes irregular as the hatch spacing increases.

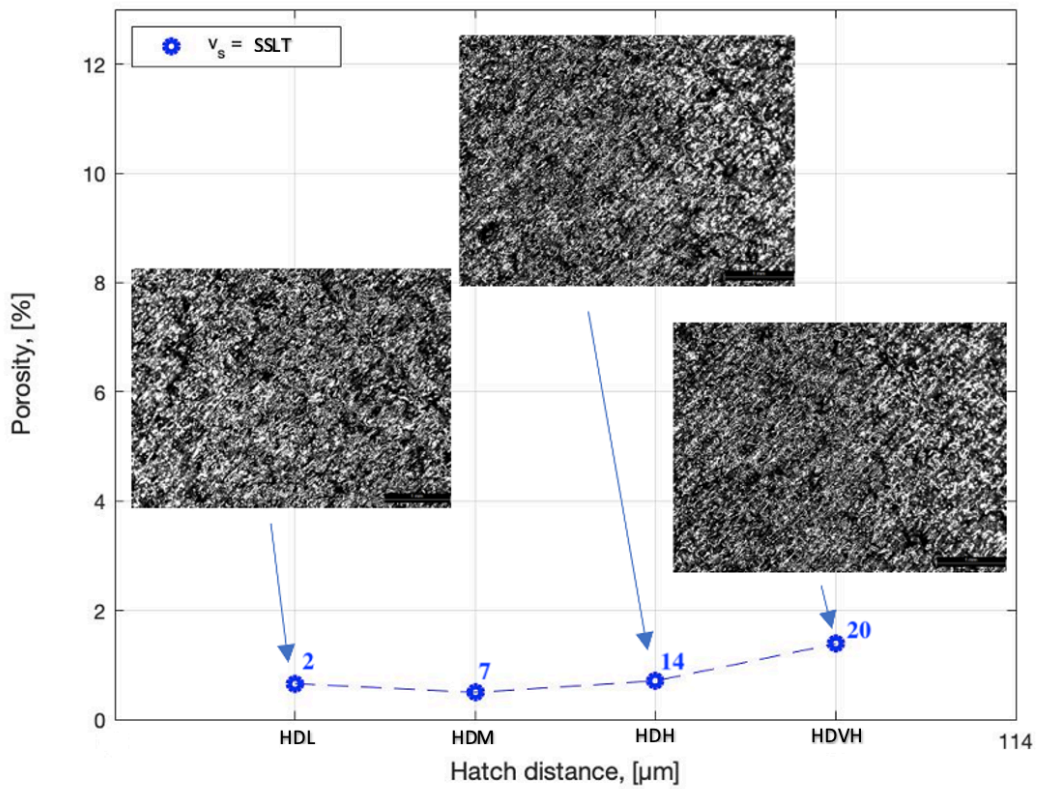


Figure 4.9: Surface porosity evolution in function of hatch distance under the lowest scanning speed

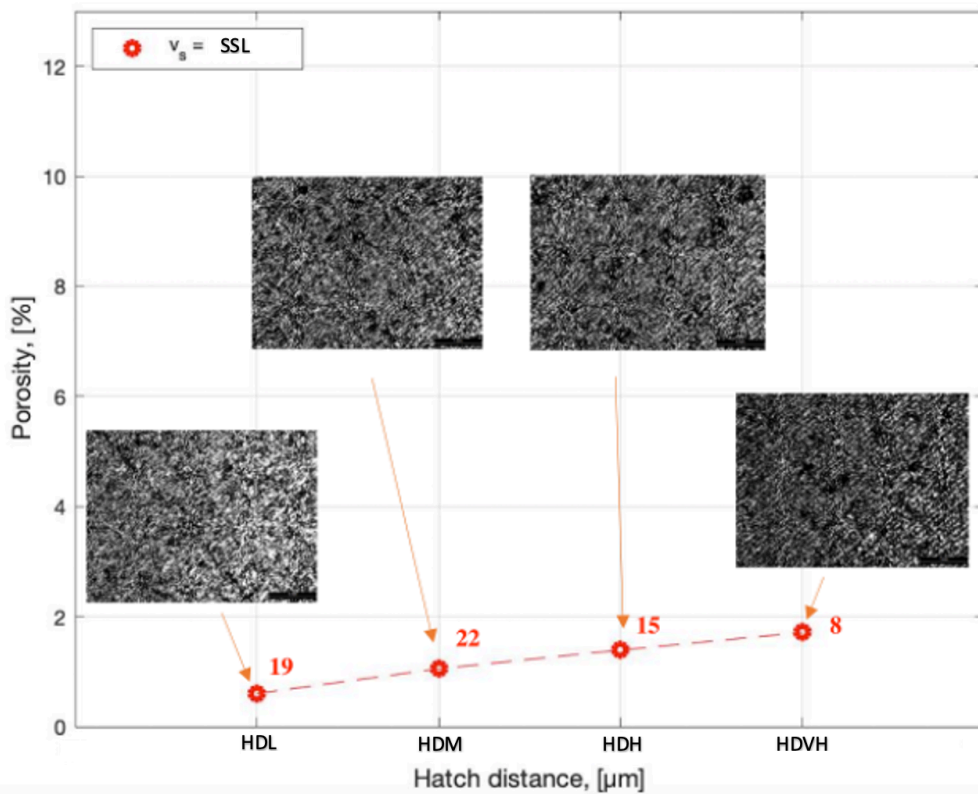


Figure 4.10: Surface porosity evolution in function of hatch distance under low scanning speed

## 4.2 Analysis of the effects of combined process parameters on relative density and porosity

The following paragraphs focus on the analysis of combined process parameters on densification behavior. In particular, the influence of VED and BR on densification and porosity will be analyzed.

### 4.2.1 The relationship between volumetric energy density and relative density

This section investigates the density results using the combined effects of the varying process parameters, referred to as volumetric energy density. As found in the literature, having a sufficiently high value of VED enhances the correct densification of the produced parts. High VED process more material per unit volume, and hence the right consolidation gives rise to compacted products. Figure 4.11 reports the densities obtained with increasing VED values, in which the samples ID have also been added on the right plot for better data visualization.

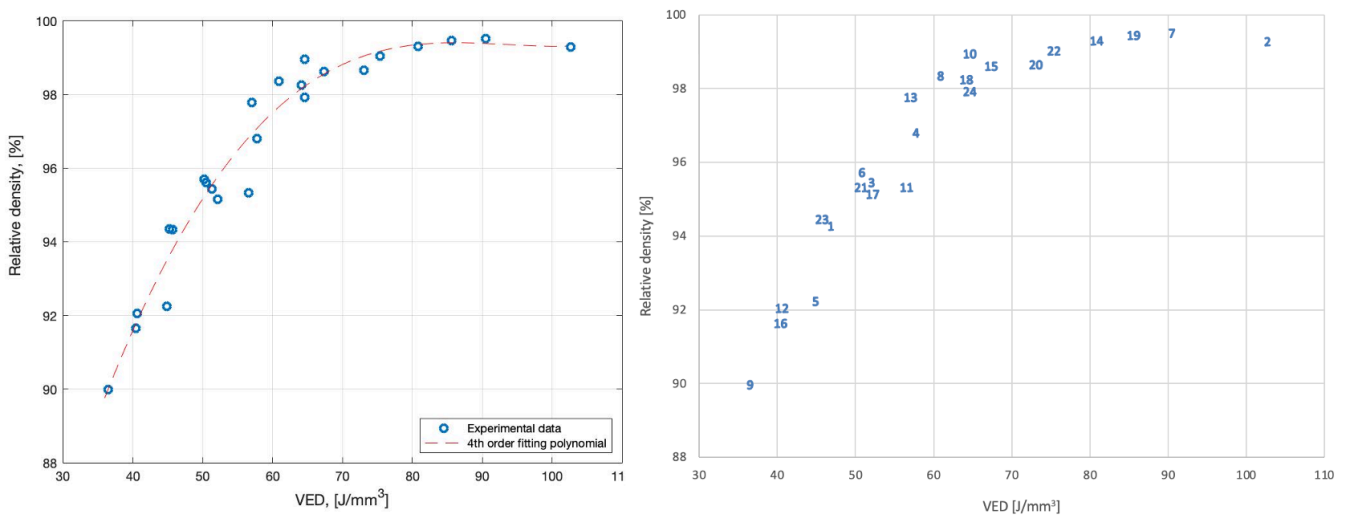


Figure 4.11: Relative density as a function of VED

The overall relative density values increase with increasing VED until reaching an almost steady region where density remains constant as VED increases. The relative density as a function of VED has been approximated with a 4<sup>th</sup> order polynomial having the following equation:

$$\rho_{\%} = a_0 \cdot VED^4 + a_1 \cdot VED^3 + a_2 \cdot VED^2 + a_3 \cdot VED \quad (4.1)$$

The coefficients  $a_0, a_1, a_2, a_3,$  and  $a_4$  have been calibrated according to the experimental data. In this study, the printed material had its maximum density at a VED of  $90.48 \text{ J/mm}^3$  and its lowest density at a VED of  $36,54 \text{ J/mm}^3$ . The results show that densities values higher than 98% can be obtained up for a specific VED threshold corresponding to  $64,19 \text{ J/mm}^3$ . Thus, it appears that for VED ranging between  $36,54 \text{ J/mm}^3$  and  $64,19 \text{ J/mm}^3$ , the energy is insufficient to assure a uniform fusion between different layers. Furthermore, samples produced with similar VEDs have similar relative densities. For example, samples 6 and 21, both built with a VED around  $50 \text{ J/mm}^3$ , show relative densities equal to 95,70% and 95,61%, respectively. Figures 4.12 and 4.13 display the surface features for samples printed with similar VEDs. These results indicate that the same density can be achieved by combining different process parameters, given that the VED obtained is similar.

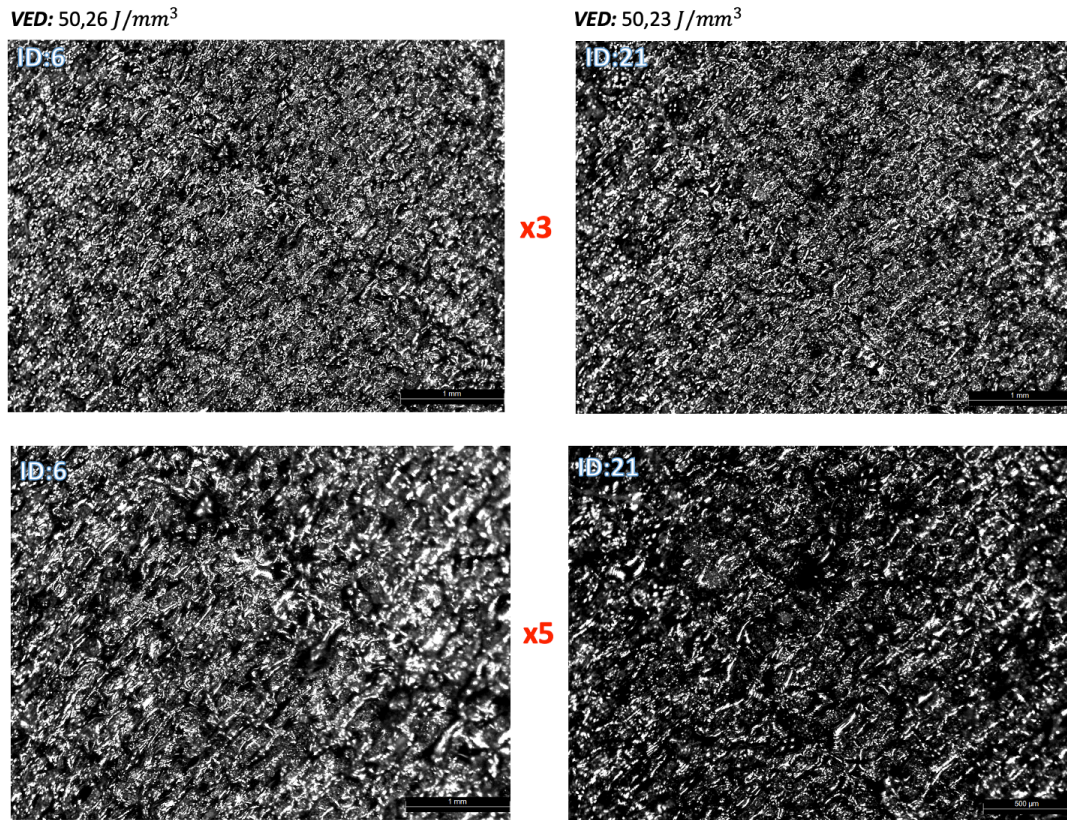


Figure 4.12: Different magnifications of surface features of samples 6 and 21

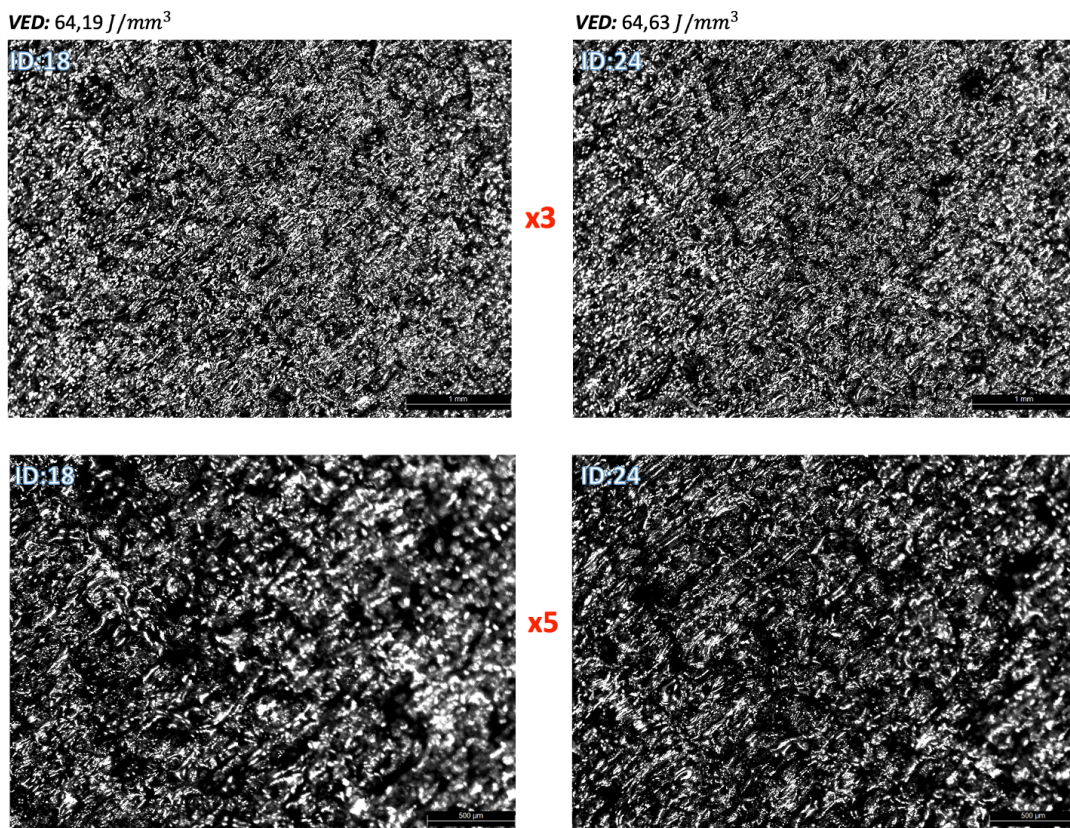


Figure 4.13: Different magnifications of surface features of samples 18 and 24

## 4.2.2 The relationship between volumetric energy density and porosity

As deeply discussed, part density is primarily affected by the introduction of pores, which are typically generated in two modes: low VED leads to lack of fusion holes, while high VED results in keyhole defects. Figure 4.14 shows the pores percentage evolution as the energy provided to the powder increases.

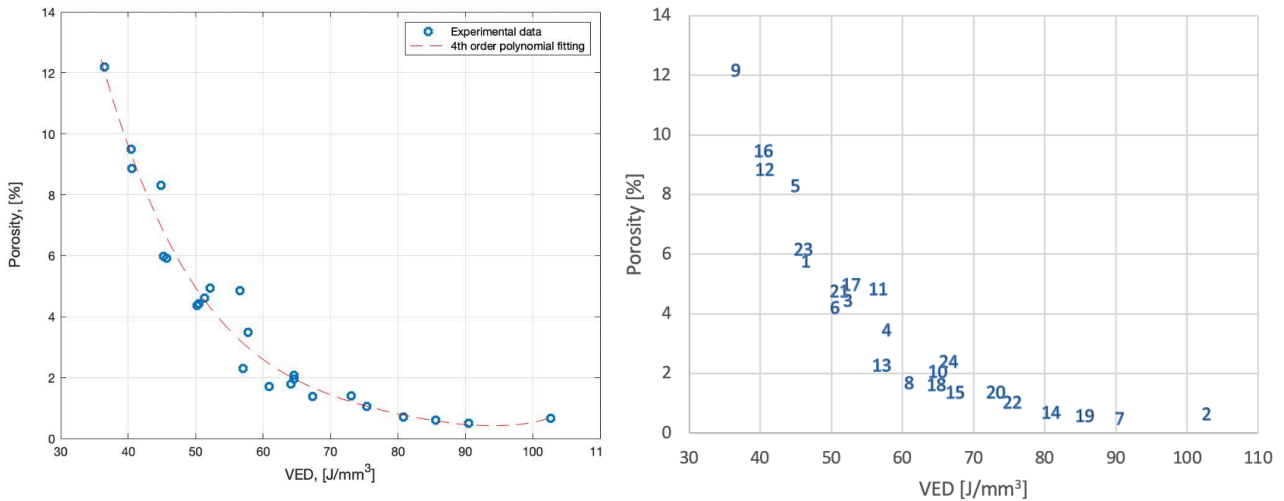


Figure 4.14: Porosity as a function of VED

Porosity gradually diminishes when VED increases until reaching an almost flat zone. Pores fraction has been approximated with a 4<sup>th</sup> order polynomial, with this equation:

$$\phi_{\%} = b_0 \cdot VED^4 + b_1 \cdot VED^3 + b_2 \cdot VED^2 + b_3 \cdot VED \quad (4.2)$$

The coefficients  $b_0, b_1, b_2, b_3,$  and  $b_4$  are opportunely selected to fit the experimental data. When the VED is above  $64,6 J/mm^3$ , porosity can reduce below 2%. The printed samples displayed a random pores distribution across the top surface. Most of the pores were visible as black marks on the surface of the specimens. Typically, the surface pores observed by analyzing the samples were attributed to be keyhole ones since the shape was almost circular, and the VED was pretty high. Figure 4.15 illustrates these kinds of defects spotted with a x3 magnification.

VED: 80,85 J/mm<sup>3</sup>

VED: 102,7 J/mm<sup>3</sup>

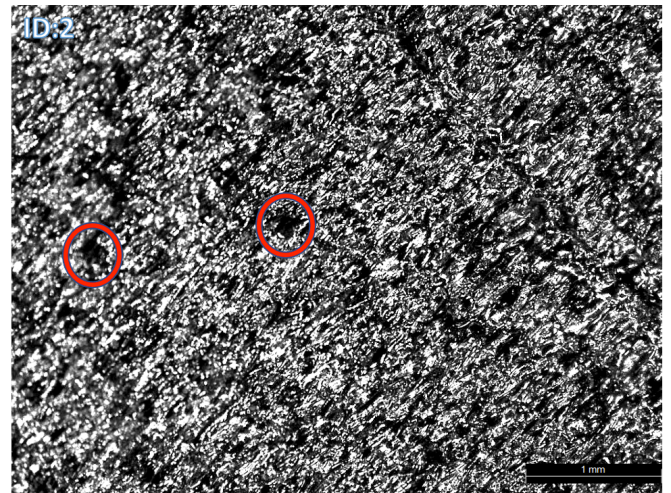
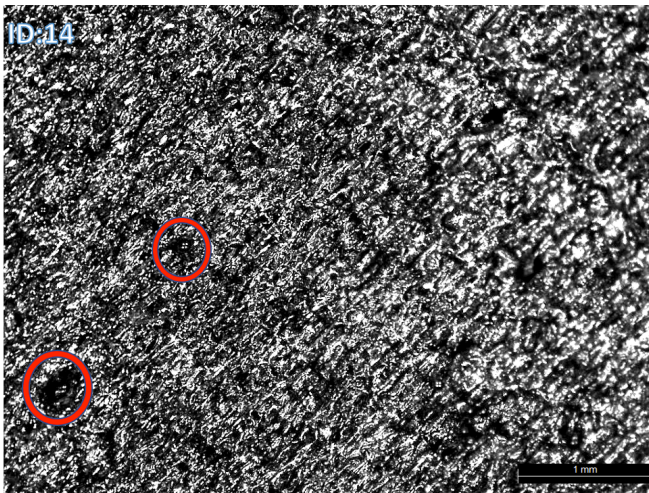


Figure 4.15: Surface pores found in samples produced at high VEDs

### 4.2.3 The relationship between productivity and density/porosity

The high cost per part is a fundamental problem associated with LPBF, mainly driven by the copious build time needed. Figures 4.16 and 4.17 present graphs showing the influence of the build rate on density and porosity. Productivity has been computed with equation (1.8), concerning only the scanning time, for the process parameters used in this study.

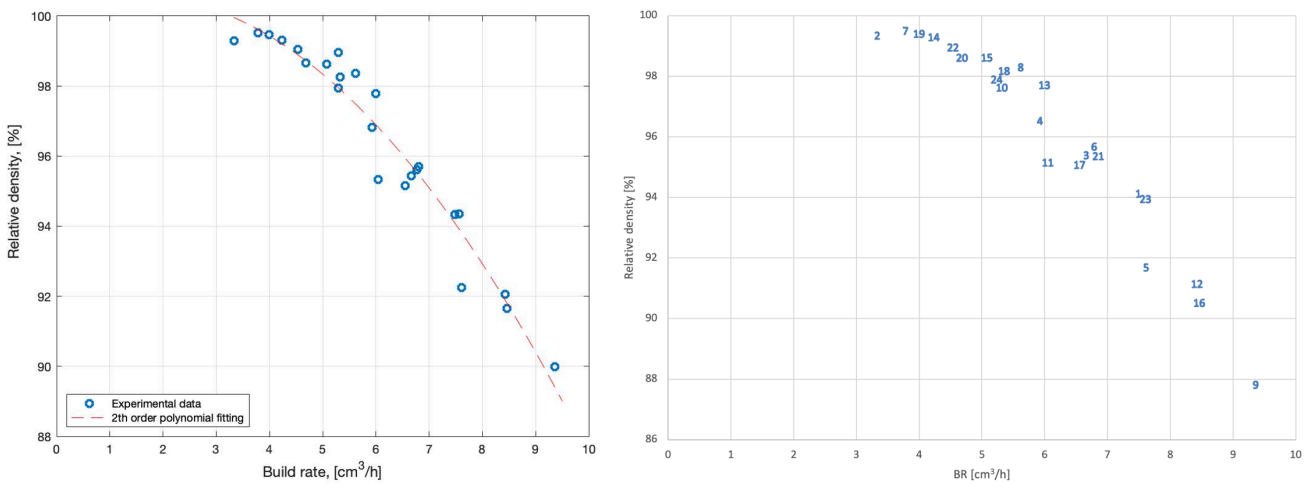


Figure 4.16: Relative as a function of the Build rate

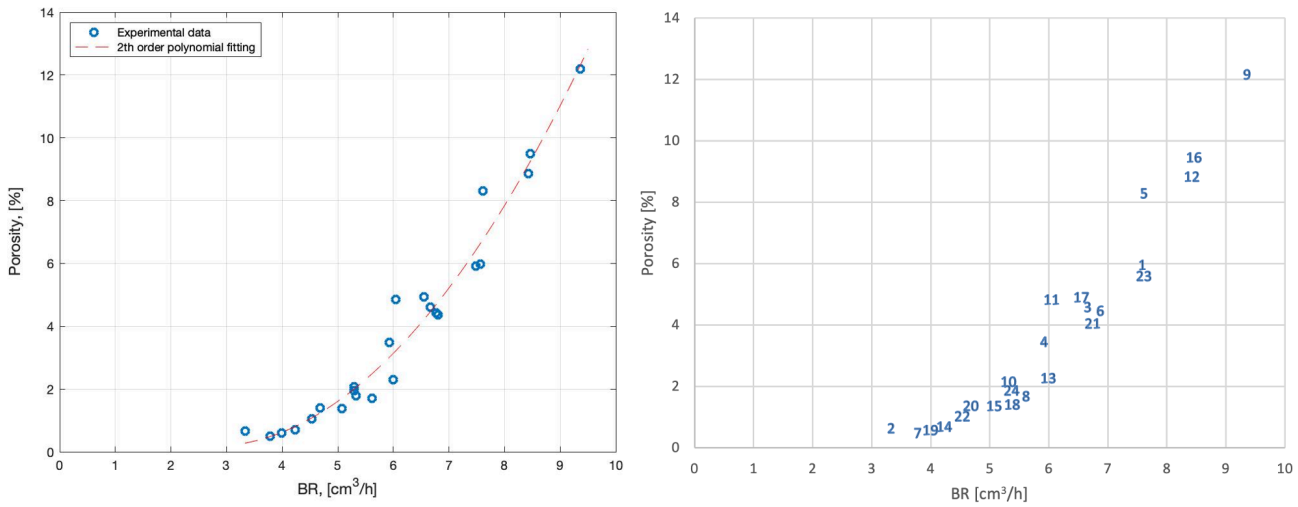


Figure 4.17: Porosity as a function of the Build rate

As expected, when the build rate increases, a degradation in density is perceived with a consequent growth in pores. By reverting equation (1.15), it is possible to find the relationship:

$$BR = \frac{P}{VED} \quad (4.3)$$

Being the BR inversely proportional to VED, the selection of significantly productive parameters leads to defects in the final part. Therefore, the highest build speed of  $9,36 \text{ cm}^3/\text{h}$  was calculated for the sample produced with the lowest energy density (SSMM scan speed and HDVH hatch distance). Therefore, this sample (ID:9) is identified by the lowest density and the highest porosity.

The results highlight the necessity to adjust the process window to increase fabrication speed and thereby reduce costs. However, this requirement must be discussed according to the final part quality needed. Indeed, the optimal Build Rate choice is subjected to the need to avoid the formation of lack of fusion porosity in the produced piece. These dissimilar constraints, required productivity and required quality, set the allowable value of process parameters functional to optimize the process.

### 4.3 Analysis of the surface quality

This part of the work aims to rate the test samples' quality status based on dimensional accuracy and surface roughness analysis. It contains the main results obtained during the examination, and it provides a discussion on the effect of a more productive set of parameters on surface quality.

#### 4.3.1 Dimensional accuracy

The dimensional accuracy assesses how strictly a LPBF machine's output complies with the original CAD model within a specified dimensional range. To evaluate how accurate the geometrical features were, a Vernier caliper was used to perform the spatial measurements of the cubes (length, height, and width). The design values for height, length, and width were 10 mm, 10 mm, and 10 mm, respectively, as given in Figure 4.18.

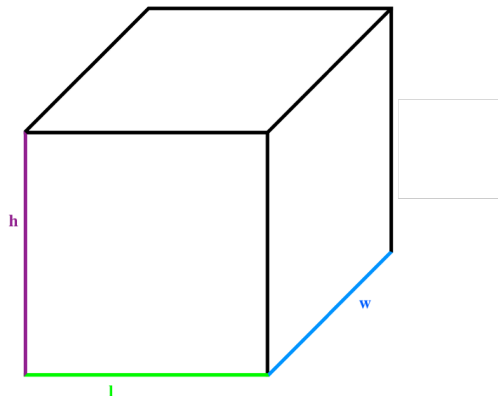


Figure 4.18: Design dimensions for the samples

Also, a 0,5 mm offset was added to the height design dimension to neutralize the cutting operation from the substrate. However, it was not considered in the accuracy evaluation. The obtained measurements are reported in Table 4.1.

Table 4.1: Dimensional measurements of the samples

Sample ID	h [mm]	l [mm]	w [mm]
1	9,1	10	10
2	9,2	10	10
3	9,5	10	10
4	9,8	10	10
5	10	10	10
6	9,3	10	10
7	9,3	10	10
8	9,2	10	10
9	9,4	10	10
10	9,8	10	10
11	10	10	10
12	9,4	10	10
13	9,2	10	10
14	9,4	10	10
15	9,6	10	10
16	9,95	10	10
17	10	10	10
18	9,5	10	10
19	9,3	10	10
20	9,3	10	10
21	9,4	10	10
22	9,9	10	10
23	10	10	10
24	9,8	10	10

The accuracy calculation was based on the following equation:

$$Accuracy = \frac{D_d - (D_d - D_m)}{D_d} \quad (4.4)$$

$D_d$  is the design value, and  $D_m$  is the measured value. The accuracy was then converted into a percentage multiplying the result by 100:

$$Accuracy_{\%} = Accuracy \cdot 100 \quad (4.5)$$

The resulting relative accuracies are presented in Table 4.2.

Table 4.2: Dimensional accuracies of the samples

Sample ID	h Acc%	l Acc%	w Acc%
1	91%	100%	100%
2	92%	100%	100%
3	95%	100%	100%
4	98%	100%	100%
5	100%	100%	100%
6	93%	100%	100%
7	93%	100%	100%
8	92%	100%	100%
9	94%	100%	100%
10	98%	100%	100%
11	100%	100%	100%
12	94%	100%	100%
13	92%	100%	100%
14	94%	100%	100%
15	96%	100%	100%
16	100%	100%	100%
17	100%	100%	100%
18	95%	100%	100%
19	93%	100%	100%
20	93%	100%	100%
21	94%	100%	100%
22	99%	100%	100%
23	100%	100%	100%
24	98%	100%	100%

The entire batch shows no deviations in length and width, even for the cubes printed with the most productive parameters. However, regarding the height accuracy, some slight distortions from the designed dimensions are observed. Samples 5, 11, 16, 17, and 23 reached a 100% accuracy for the height dimension, while the minimum height accuracy was recorded for sample 1 (91%). The effects of process parameters on the height deviations cannot be stated since, as said, the cutting operation undoubtedly influenced the measurements. Despite this, in general, all sample conditions were on

target and above 91% accurate. These results confirm that the LPBF process provides high dimensional accuracy, an essential characteristic required to produce functional components.

### 4.3.2 Surface roughness

The samples' surface roughness was analyzed using a profilometer. The instrument used recorded measurements of  $R_a$  and  $R_z$  in  $\mu\text{m}$  by moving its probe over the surface of a sample in a straight line. The roughness readings were noted on three segments along the longitudinal axis of each face of the cubes, and the roughness profiles were recorded. Figure 4.19 illustrates the nomenclature adopted to label the faces of each sample. Top face means the surface with a normal vector parallel to the building axis; instead, faces 1, 2, 3, and 4 are identified as side surfaces.

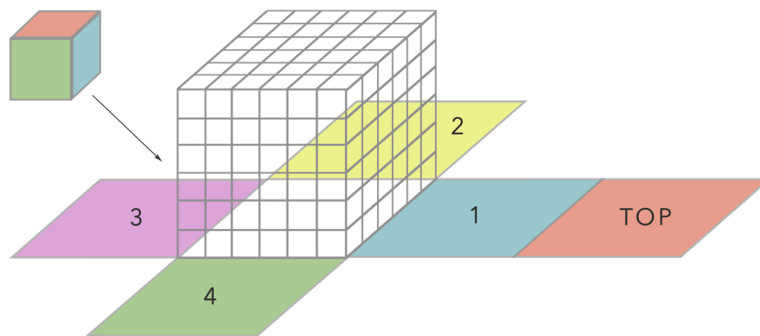


Figure 4.19: The nomenclature of the cubes' faces

The measured data indicate that a minimum value of top surface roughness,  $R_a = 7,50 \mu\text{m}$ , characterizes sample 7, having a SSLT scan speed and a HDM hatch distance. The maximum value of top surface roughness ( $R_a = 13,04 \mu\text{m}$ ) was seen in cube number 23. The corresponding values of scan speed and hatch distance were SSMM and HDM. The roughness profiles for the top faces of samples 7 and 23 are presented in figures 4.20 and 4.21.

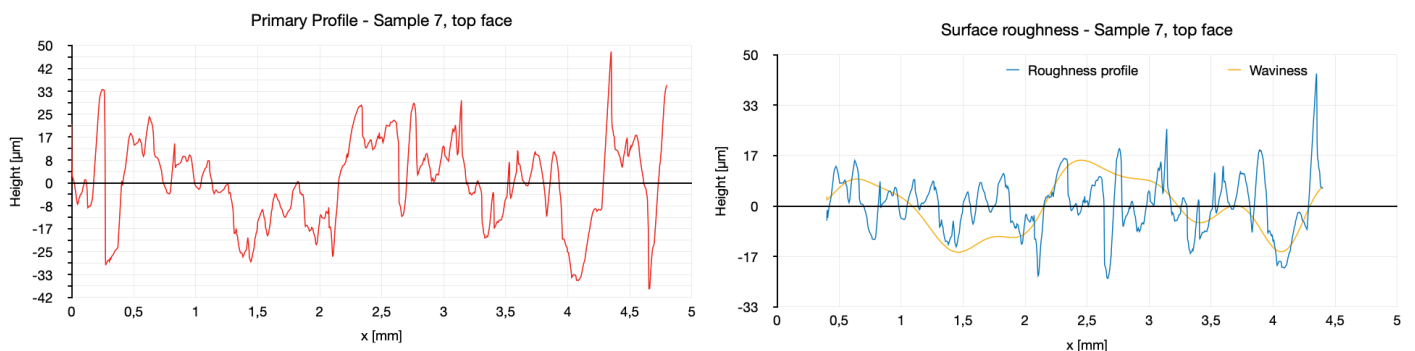


Figure 4.20: Roughness profiles of the top face of sample 7

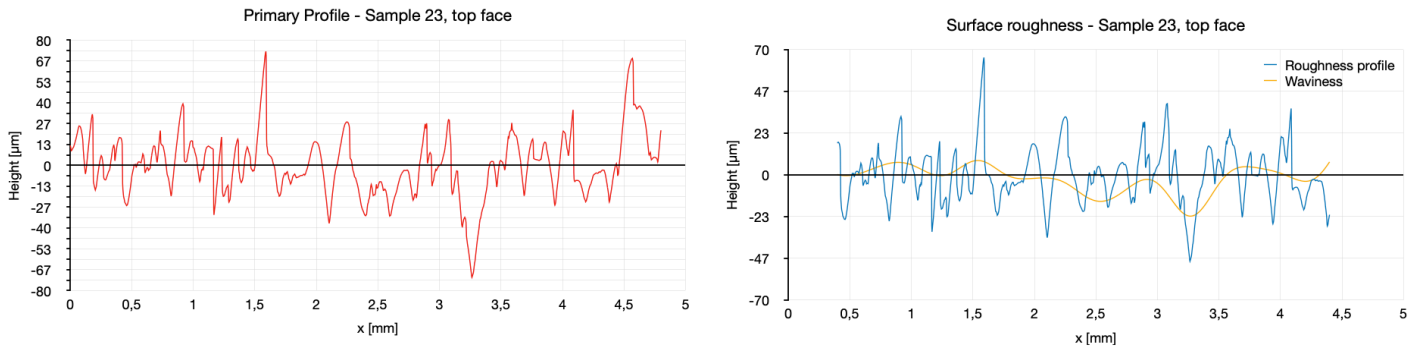


Figure 4.21: Roughness profiles of the top face of sample 23

It can also be observed that the lowest reading of side surface roughness ( $R_a = 3,53 \mu\text{m}$ ) was obtained for the face number 4 of sample 14 (SSLT scan speed, HDH hatch distance), while cube 23 showed the maximum side roughness value ( $R_a = 6,26 \mu\text{m}$ ), having a SSMM scan speed and a HDM hatch distance. The average maximum peak to valley  $R_z$ , computed for the samples' top surface, also displays a maximum of  $73,78 \mu\text{m}$  in cube number 23. In contrast, a minimum of  $43,83 \mu\text{m}$  can be observed in sample 7. Regarding the side measurements, the highest  $R_z$  equal to  $39,33 \mu\text{m}$  was found in face 2 of sample 10, produced with a SSM scan speed and a HDM hatch distance. Instead, the minimum measurement ( $R_z = 22,78 \mu\text{m}$ ) distinguished face 4 of the cube number 14.  $R_a$  and  $R_z$  values reveal that the trend in average and total roughness for each sample is similar, although the spread is large. In addition, results show that the measured mean and peak to valley roughness on the side surface was usually lower than the results obtained on the top surface. Top surfaces appeared to be overall irregular and uneven, while side faces were slightly smoother. The complete list of results in terms of surface roughness and the corresponding standard deviations is provided in the appendix.

### 4.3.3 Effects of VED on surface roughness

Although it is not possible to find an apparent trend between surface roughness and VED, all the minimum roughness measurements were taken on samples printed with an energy density ranging from  $67,38 \text{ J/mm}^3$  to  $90,48 \text{ J/mm}^3$ . This finding can be explained by considering that at first, poor densification occurred with the lowest levels of VED; hence the powder was sintered but not fully melted, resulting in the highest roughness as for sample 23 ( $R_a = 13,04 \mu\text{m}$ ), produced with VED of  $46,54 \text{ J/mm}^3$ . A graph showing the influence of VED on Surface roughness for samples' face number 4 is visible in figure 4.22.

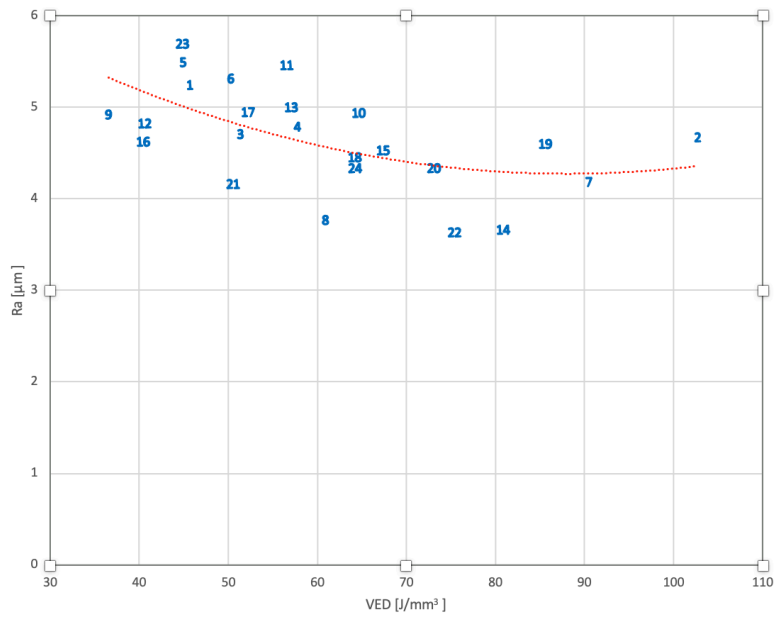


Figure 4.22: Influence of VED on Surface roughness for samples' face 3

The trend between surface roughness and VED shows a region in which the surface quality is optimal. On the other end, samples with similar VEDs showed a considerable spread in roughness results. This finding demonstrates that individual parameters play a significant role in estimating surface roughness, and therefore, the influence of each parameter should be carefully assessed through a suitable method.

#### 4.3.4 Effects of productivity on surface roughness

In this section, the mean values of top roughness  $R_a$  are taken as a reference to investigate the influence of higher productivity on the parts' surface quality. Figure 4.23 illustrates the effects high productive parameters have on the final surface quality.

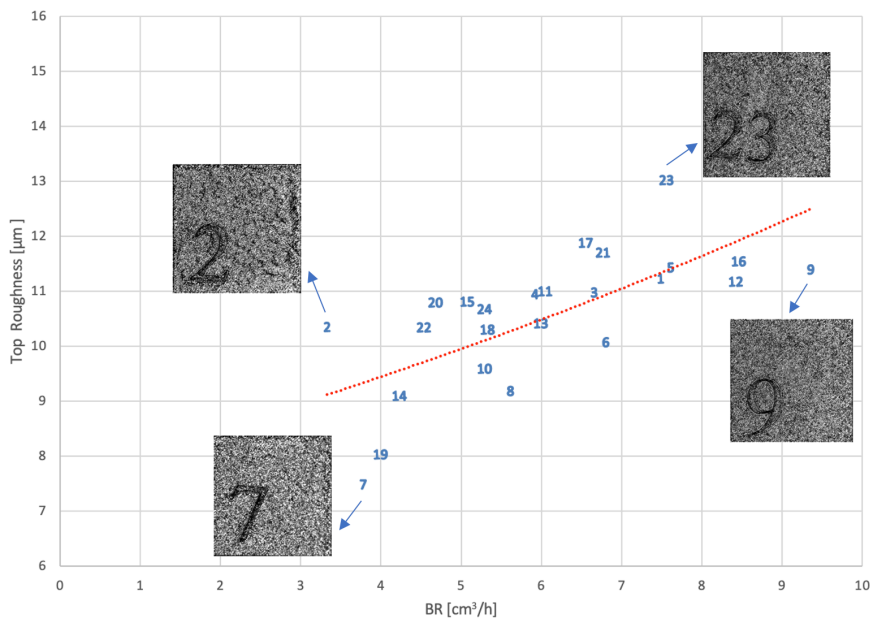


Figure 4.23: Top Roughness versus BR

Overall, it appears that as the productivity grows, the surface roughness increases consequently, even if data measurements reveal a great spread. Therefore, it was decided to compare the roughness profiles for three samples, one each printed with a low productivity set of parameters (14), one produced with medium productivity (6), and the last one built with a high productive set (16). Such profiles are shown in figure 4.24.

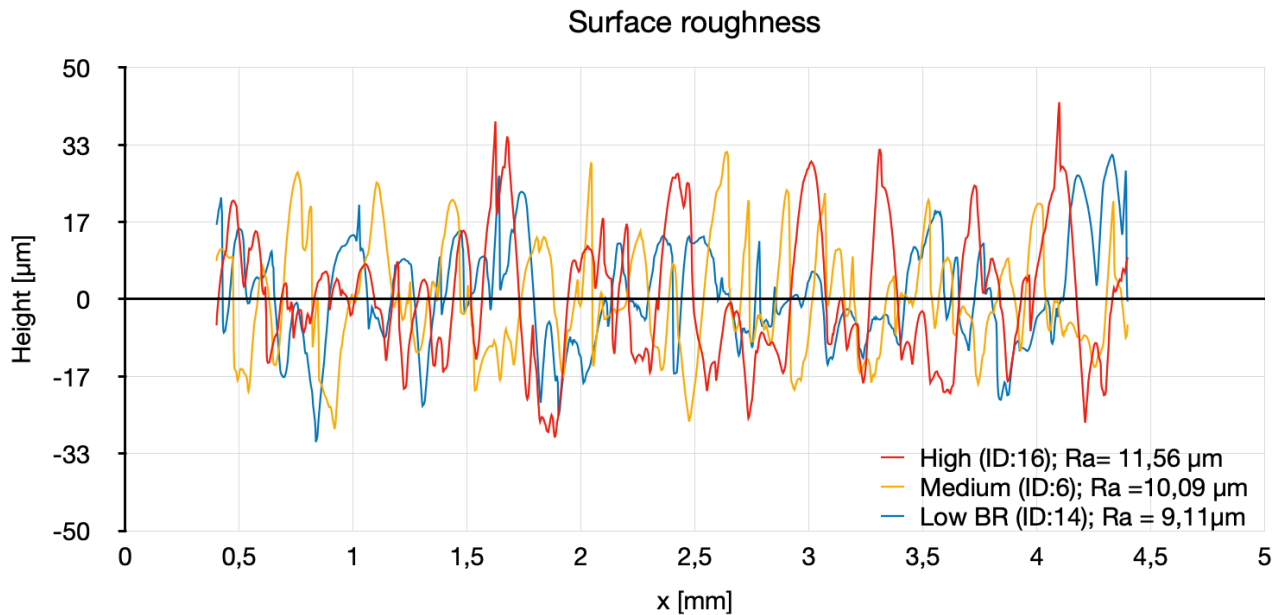


Figure 4.24: Roughness profiles for High, Medium, and Low BR

The profiles comparison shows that peaks and valleys are more accentuated in sample 16, printed with a high value of build rate. Conversely, as the build rate decreases, peaks and valleys become less evident, like the case of sample 14. In general, a highly productive set of parameters results in increased roughness and surface porosity.

#### 4.4 Mechanical characterization

The final step to assess the quality of the produced parts focused on mechanical testing. The selection of the process parameters for further characterization was based on the porosity analysis of the trial samples. Indeed, the pores percentage represents a good indicator to predict mechanical properties since, in general, the higher porosity is, the lower mechanical characteristics are.

##### 4.4.1 Selection of the process parameters for mechanical testing

The results obtained in the analysis of the VED effect over samples' porosity guided the choice of two series of parameters for the mechanical characterization. Within the process window, range observed ( $64,6 J/mm^3 - 102,70 J/mm^3$ ), two test cubes, namely number 2 and number 14, displayed a low level of porosity of 0,66% and 0,71% respectively, with two different VED values ( $102,7 J/mm^3$  and  $80,85 J/mm^3$ ). The selected parameters were then utilized to produce six tensile specimens. The first three specimens were produced using Set 1 (higher VED); the other three bars were printed with Set 2 (lower VED). The chosen process parameters and the corresponding tensile specimens manufactured are summarized in table 4.3.

Table 4.3: Selected process parameters for further characterization

Tensile specimen ID	Set Number	Laser Power [W]	Hatch distance [ $\mu m$ ]	Layer thickness [ $\mu m$ ]	Scan speed [mm/s]	VED [ $J/mm^3$ ]	BR [ $cm^3/h$ ]
1,2, and 3	1	95	HDL	25	SSLT	102,70	3,33
4,5, and 6	2	95	HDH	25	SSLT	80,85	4,23

#### 4.4.2 Tensile test

The tensile test was exploited to understand if the stress-strain characteristic of the two sets printed with different in-range VEDs had similar behaviors. The test was performed mounting the specimens in a dedicated machine in the IAM laboratory at Politecnico di Torino and subjecting them to tension. The tensile force was recorded as a function of the increase in length. The data registered by the machine were then normalized concerning the specimens' dimensions to obtain the plots of tensile stress versus strain. The stress is expressed as the tensile Load [N] divided by the sample cross-section [ $mm^2$ ]:

$$\sigma = \frac{F}{A_0} [MPa] \quad (4.6)$$

The engineering strain represents the displacement resulting from the application of the tensile stress:

$$\varepsilon = \frac{l-l_0}{l_0} [mm/mm] \quad (4.7)$$

$l_0$  is the initial length, and  $l$  is the length after the load application. The geometrical data measured for each specimen are indicated in table 4.4.

Table 4.4: Specimens' geometrical dimensions

Specimen ID	$l_0$ [mm]	$A_0$ [ $mm^2$ ]
1	95	20,176
2	95	18,688
3	50	21,222
4	50	21,88
5	50	22,577
6	50	22,080

Unfortunately, the machine did not record the data from the tests for specimens 3 and 4. Instead, the stress-strain curves for specimens 1, 2, 5, and 6 are shown from figure 4.25 to figure 4.28.

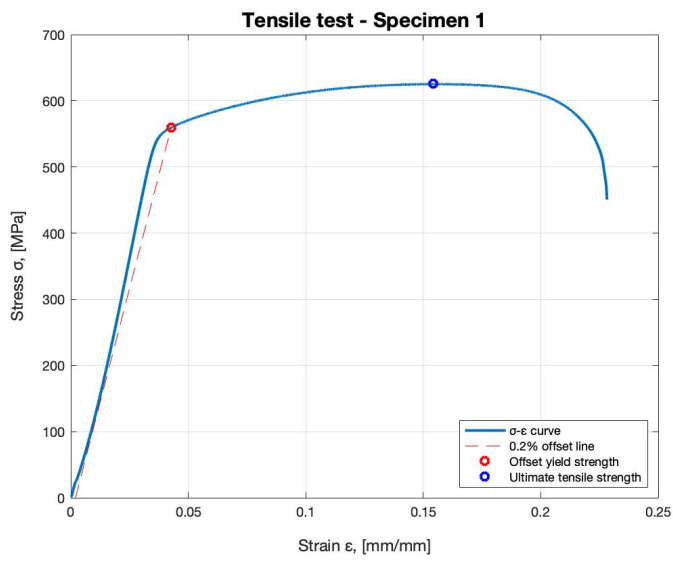


Figure 4.25:  $\sigma$ -  $\epsilon$  plot for specimen 1

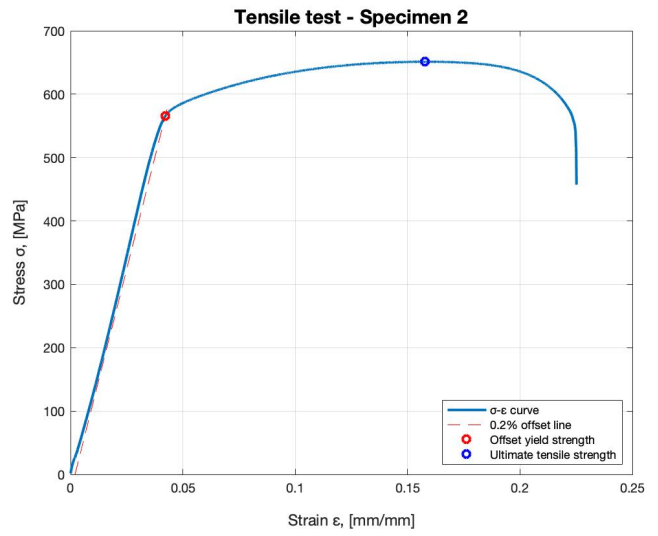


Figure 4.26:  $\sigma$ -  $\epsilon$  plot for specimen 2

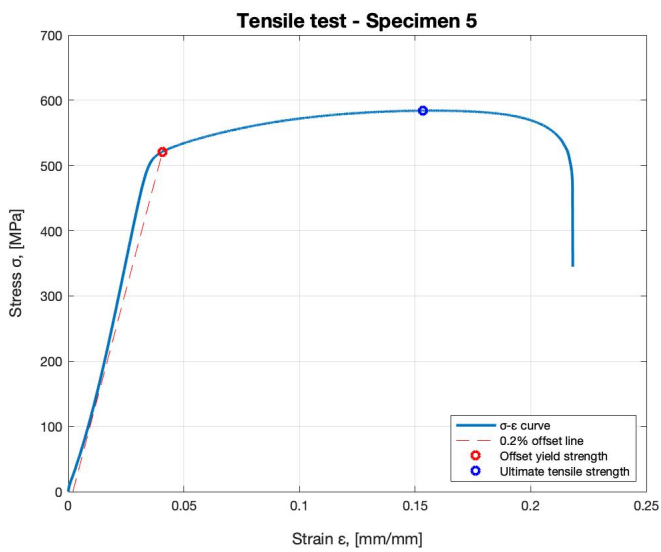


Figure 4.27:  $\sigma$ -  $\epsilon$  plot for specimen 5

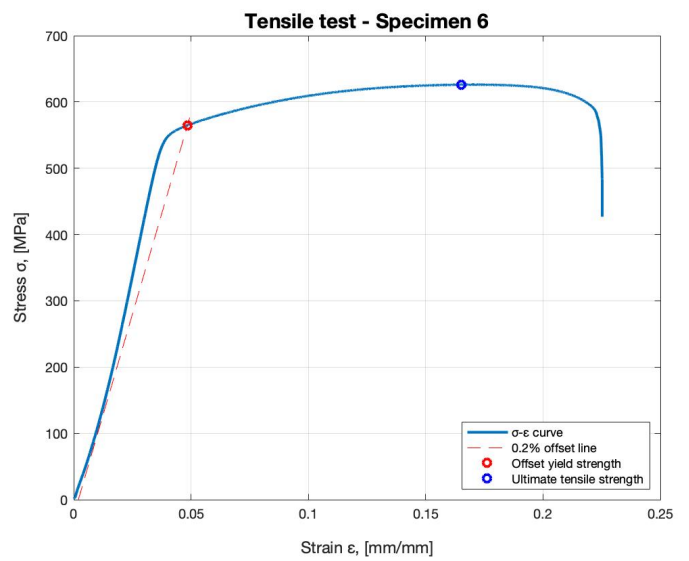


Figure 4.28:  $\sigma$ -  $\epsilon$  plot for specimen 6

Figure 4.29 presents engineering stress versus engineering strain responses of the four tensile specimens built with the selected VED levels.

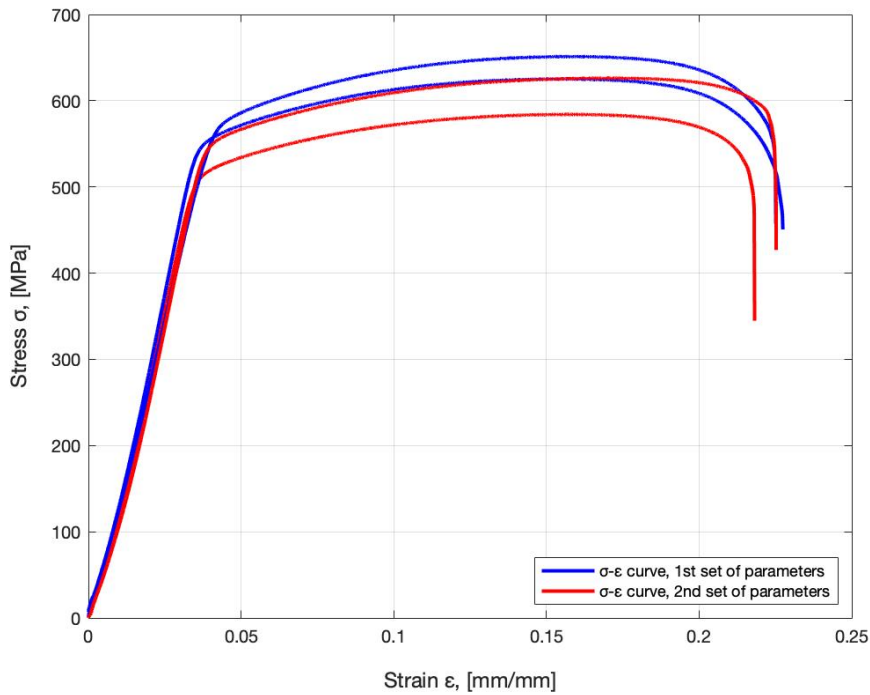


Figure 4.29:  $\sigma$ -  $\epsilon$  plots for the different specimens fabricated

The tensile properties extracted, Yield strength (YS), Ultimate tensile strength (UTS), and elongation at failure (E), are reported in Table 4.5. These characteristics are comparable with the data found in the literature for LPBF AISI 316L production.

Table 4.5: Tensile properties for AISI 316L specimens printed with the selected VED values

<b>Tensile Specimen</b>	<b>YS [MPa]</b>	<b>UTS [MPa]</b>	<b>VED [J/mm<sup>3</sup>]</b>	<b>BR [cm<sup>3</sup>/h]</b>
1	546,06	625,52	102,7	3,33
2	570,12	651,51	102,7	3,33
Mean	558,09 ± 23,58	638,52 ± 25,47	-	-
5	521,1	584,35	80,85	4,23
6	554,55	626,41	80,85	4,23
Mean	537,83 ± 32,78	587,38 ± 76,50	-	-

Overall, the specimens having VED equal to 102,70 J/mm<sup>3</sup> show a slightly better tensile behavior. The average values characterizing the first set of parameters are 558,09 MPa for YS, 638,52 MPa for UTS, and 23,05 % for E. Instead, the tensile properties for the second set of parameters show, on average, a 4% degradation in YS (537,83 MPa) and an 8% decrease in UTS (587,38 MPa). Such findings show that a 7,5% increase in porosity, as for Set 2, makes the specimen weaker, leading to a worse tensile response. Despite this, both the VED values allow producing parts with acceptable mechanical properties which satisfy the recommended values provided by the ASTM 240/240M-18 standard (485 MPa for UTS and 170 MPa for YS).

## 4.5 Cost analysis

From an economic point of view, the most important advantage of using Powder Bed Fusion technologies is the low cost for small production batches. The reason why engineers and machine operators can reduce the overall costs of additive components is, first of all, the possibility to design and create physical models within few hours during the same working day. Hence, it is possible to create customized components or small production batches directly and without the need for molds. Furthermore, this involves a short production chain since the time between the design and marketing phases drastically reduces.

Moreover, the LPBF process offers the opportunity of producing just what is necessary, which significantly cuts the costs linked to the storage of material destined for obsolescence built for the sole purpose of lowering production costs.

LPBF is also synonymous with little processing waste that translates into reducing costs for purchasing raw materials and material disposal. This peculiarity, compared to traditional manufacturing techniques, completely overturns the point of view of the materials used: by producing an object layer by layer, with no material waste, the material cost is no longer proportionate to the total material used (comprising scraps), but it depends only on the quantity of material actually used. The result is a search for complex and lightened shapes made possible by the freedom of design offered by the technology. In this, topological optimization can be decisive. Topological optimization is a re-design operation that seeks the best distribution of the material by modifying the component's geometry to lighten it while maximizing its performances, considering the specific mechanical properties of the material and the project's objectives.

The result will be an efficient, light, and functional component that also beneficially impacts costs. For example, in industrial fields where lightened components translate into fuel savings, such as the aerospace sector, the costs to be sustained decrease thanks to weight reduction. According to these considerations, this section aims to analyze manufacturing costs with different build scenarios, each with an estimated cost structure, calculated exploiting the cost model proposed in chapter 2.

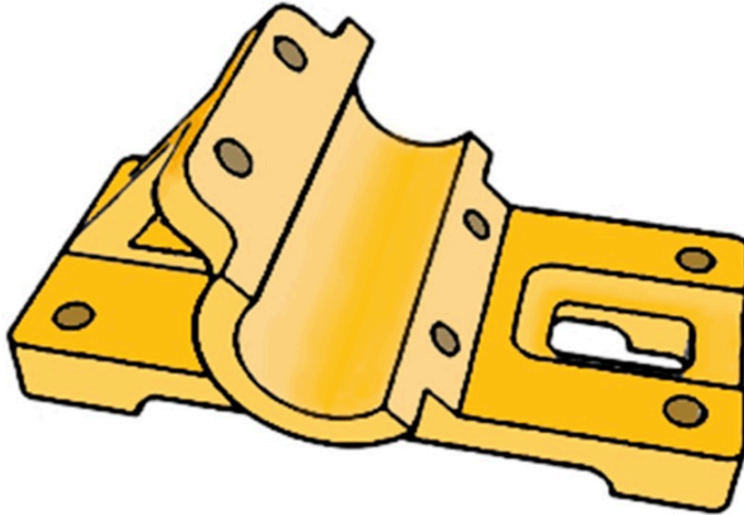
Two mechanical components that reflect variation in product size, geometry, and application are analyzed in production cost. The chosen components are a bearing block and a turbine wheel, taken from a representative basket proposed by *Baumers* [60]. Two production scenarios are studied for each mechanical component: the first uses parameters' set number 1 ( $BR = 3,33 \text{ cm}^3/\text{h}$ ), and the second uses parameters' set number 2 ( $BR = 4,23 \text{ cm}^3/\text{h}$ ). Both sets can create parts with good mechanical properties, as seen in the previous section.

All manufacturing costs and build time estimations were carried out considering a commercial Concept Laser Mlab R equipment. The proposed cost model allows computing the build time ( $T_b$ ), the machine cost ( $C_{mac}$ ), the material cost ( $C_{mat}$ ), the energy cost ( $C_{ene}$ ), and the gas cost ( $C_{gas}$ ).

The pre/post-processing costs ( $C_{p/p}$ ) should also be considered carefully. These costs are due to material preparation and secondary finishing operations. Typical pre and post-processing activities are powder drying, support material removal, surface texture improvements, aesthetic improvements, property enhancements using non-thermal techniques, and property enhancements using thermal techniques. NIST found that pre/post-processing costs account for 4% up to 13% of overall production costs, depending on the AM technique and the alloy involved [37]. Therefore, in this analysis, such contributions are assumed to weigh 10% of the total cost. Other cost structures arising from building failure, machine maintenance, machine idleness, tools consumption, and inventory expenses are neglected.

#### 4.5.1 Case study 1: Bearing block

The first mechanical part examined is a bearing block. This component provides support for a rotating shaft with the help of compatible bearings. A schematic representation with the main topological features of the piece is presented in figure 4.30.



<b>Bearing block</b>	
Dimensions:	127 x 76 x 52 mm
Volume:	96,645 cm <sup>3</sup>

Figure 4.30: Bearing block schematic

The input data adopted to evaluate the build time and the cost of the part were the AISI 316L powder cost equal to 38 €/kg, and the part volume equal to 96,645 cm<sup>3</sup>. To accurately capture the actual cost of material consumed, the material cost was corrected with two coefficients to account for material recyclability and support material. The first one was set to 1,5, while the second one was assumed to equal 1,1. Table 4.6 reports the results obtained in terms of build time and costs for the bearing block.

Table 4.6: Costs results for the bearing block

Set	BR [cm <sup>3</sup> /h]	$T_b$ [h]	$T_b$ reduction	$C_{mat}$ [€]	$C_{mac}$ [€]	$C_{ene}$ [€]	$C_{gas}$ [€]	$C_{p/p}$ [€]	$C_{total}$ [€]	Savings
1	3,33	33,6	-	48,0	176,50	10,95	5,22	26,74	267,42	-
2	4,23	27,5	18%	48,0	144,11	8,94	4,26	22,81	228,14	15%

The total time required to produce one part with the set of parameters 1 is 33,6 hours. However, employing the set of parameters 2 makes it possible to manufacture the same component in 27,5 hours, reducing the build time by 18%.

The production time reduction also reflects on costs, as it is possible to pass from a total cost of 267,42 € for set 1 to 228,14 € for set 2, with a 15% cost savings.

As displayed in figure 4.31, the cost deployment shows that the main expense in the LPBF process is the machine investment cost, compared to which the percentages of the energy, gas, pre/post-processing, and material costs are lower.

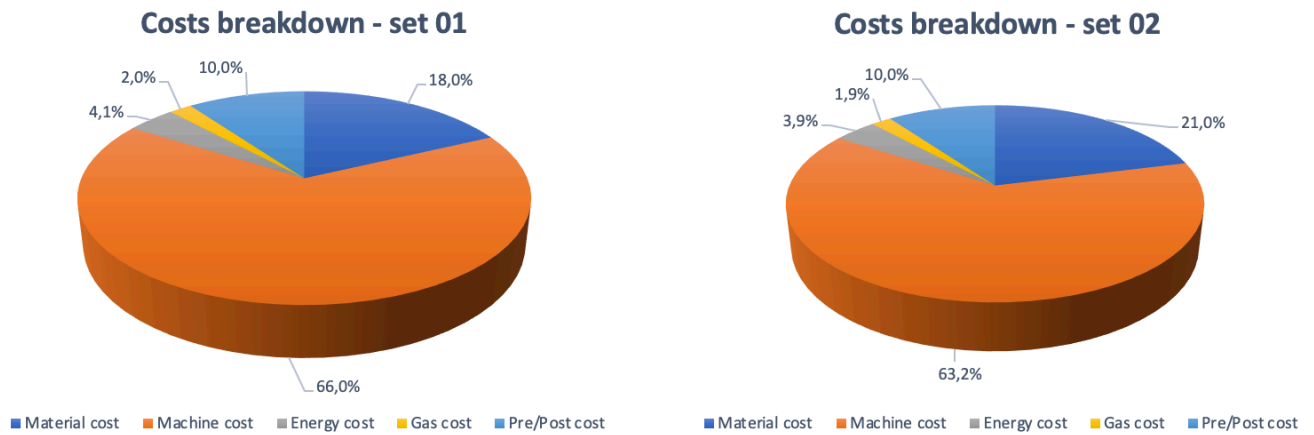


Figure 4.31: Cost deployment for the bearing block

The total production cost is found to depend strongly on the manufacturing time. Consequently, the machine cost is by far the most significant factor in a LPBF manufactured piece, leaving the effect of the other contributions to less than 37 % of the total costs. The build time is hence the crucial ingredient to reduce the cost per part for LPBF.

#### 4.5.2 Case study 2: Turbine wheel

The second component examined is a turbine wheel. This part, particularly suitable for topological optimization, is typically employed in the aerospace field. Its complex shape and limited volume make the part ideal for production via the LPBF process. Figure 4.32 shows a schematic representation of the piece.



Turbine wheel	
Dimensions:	54 x 54 x 28 mm
Volume:	20,618 cm <sup>3</sup>

Figure 4.32: Turbine wheel schematic

The cost model was applied to this part considering a powder cost for AISI 316L equal to 38 €/kg and the part volume equal to 20,618 cm<sup>3</sup>. The recyclability and support material coefficients were both assumed equal to 1,5. Since the component shape is remarkably light, in this case, the possibility of producing a batch with ten pieces is also considered to evaluate the advantages of accurately filling the building platform. Table 4.7 reports the results obtained in terms of build time and costs for the turbine wheel.

Table 4.7: Costs results for the turbine wheel

Set	N. per job	BR [cm <sup>3</sup> /h]	T <sub>b</sub> [h]	T <sub>b</sub> reduction	C <sub>mat</sub> [€]	C <sub>mac</sub> [€]	C <sub>ene</sub> [€]	C <sub>gas</sub> [€]	C <sub>p/p</sub> [€]	C <sub>total</sub> [€]	C <sub>part</sub> [€]	Savings
1	1	3,33	10,8	-	13,97	56,73	3,52	1,68	8,43	84,33	84,33	-
2	1	4,23	9,5	12%	13,97	49,82	3,09	1,47	7,59	75,95	75,95	10%
1	10	3,33	66,5	-	139,7	349,06	21,66	10,32	57,86	578,56	57,86	-
2	10	4,23	53,3	20%	139,7	279,95	17,37	8,27	49,48	494,78	49,48	14%

The build time required to produce one turbine wheel with the set of parameters 1 is 10,8 hours, while a 12% reduction can be achieved by manufacturing the same part with the parameters set 2. As a result, the cost per part can be reduced from 84,33 € to 75,95 €, with a 10% cost savings. On the other hand, producing only a single piece is relatively inefficient: building ten pieces simultaneously reduces the cost per part to 57,86 € and 49,48 €, respectively, for set 1 and set 2. Thus, a correct utilization of the building plate can be a crucial variable to help the manufacturer optimize the process in both efficiency and costs. Figures 4.33 and 4.34 show the cost deployments for the cases of single-part production and a batch of ten pieces.

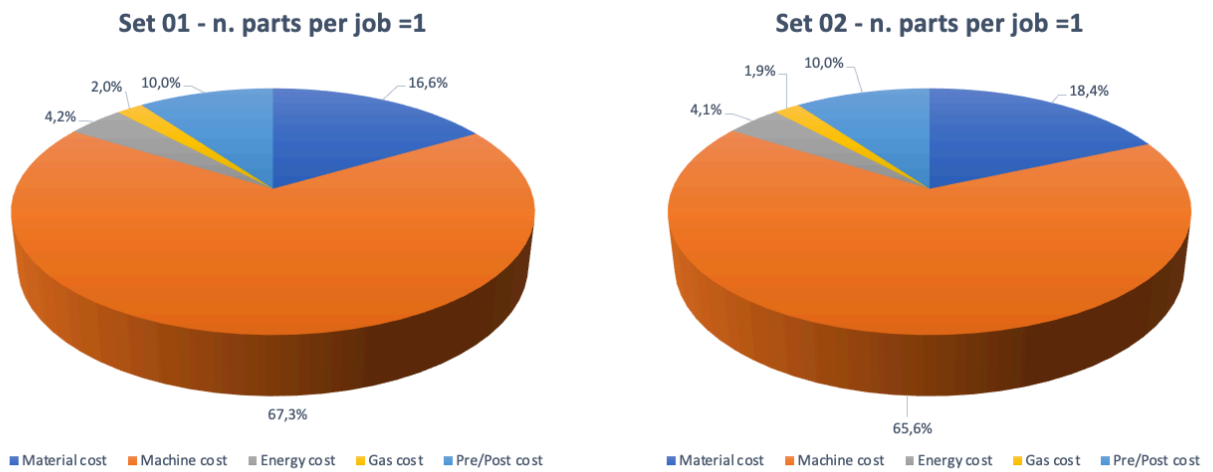


Figure 4.33: Cost deployment to produce a single turbine wheel

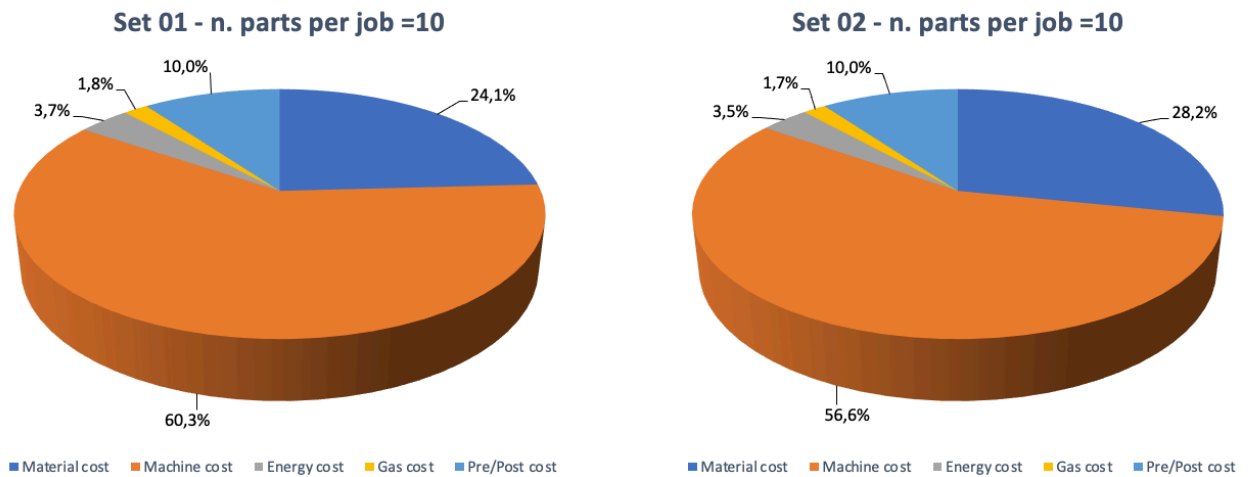


Figure 4.34: Cost deployment to produce 10 turbine wheels

Despite the machine cost still representing the main contribution to the total cost, in this case, the relative weight can be reduced to 56,6% by optimizing the process parameters and by better filling the building platform. However, fully utilizing the building platform is an essential operation the user should concentrate on to cut costs.

## 5 Conclusions

In this thesis project, AISI 316L samples produced by LPBF were studied to understand the effect of process parameters on density, porosity, surface quality, tensile properties, and build time.

This study demonstrated how to improve the productivity of laser powder bed fusion steel without significantly compromising density, porosity, or mechanical properties. The experimental performance considers a wide range of scanning speeds and scan spacings. In addition, the fabricated samples were evaluated both considering the single process parameters and the volumetric energy density.

As far as surface quality is concerned, the more the parameters are productive, the rougher the piece surface will be.

The experimental analysis also showed an increase in porosity percentage and a reduction in the relative density by enlarging the hatch spacing and the scanning speed. The VED was used to predict the porosity and the mechanical properties of the parts. VED is a reliable parameter for comparing part porosity and productivity since the maximization of the BR implies the minimization of VED. Among the VED range, two sets of parameters resulting in different energy densities were chosen to produce tensile samples for the mechanical characterization. The first set (higher VED) showed lower characteristics both in terms of productivity and porosity. The second set (lower VED) displayed a 27% higher productivity, while the pores content increased. Indeed, set 2 was characterized by a porosity percentage 7,5% higher than set number 1. The analysis of the results revealed that this augmentation in porosity reflected on mechanical properties. Thus, specimens with higher energy density registered higher tensile properties, while those made with lower energy density resulted in less performing mechanical properties. Overall, set 2 showed a decrease of 4% and 8%, in yield strength and ultimate tensile strength, respectively.

Despite the slight reduction in mechanical properties, the advantages in terms of build time and production cost are noteworthy. Indeed, set 2 allowed to produce parts with a 12% faster build time in the worst case, compared to the parameters 'set with higher VED.

As pointed out in the case study, the increase in productivity of the parameters set number 2 can lead to significant advantages in terms of production time and cost. For example, using this set of parameters allows to save up to 39€ per part in the case of a bearing block, and a 14% savings can be obtained for the turbine wheel production.

In addition, results show that optimizing the building platform utilization (the number of pieces on the build plate) improves the production speed since the recoating time for each powder layer is constant regardless of the number of parts being manufactured.

The findings presented in this study indicate that the build time can diminish by adjusting the process parameters while maintaining good mechanical properties. Still, for the lower VED, the mechanical properties can well satisfy the standard specifications for AISI 316L stainless steel, according to ASTM A240M-18. Hence, depending on the application, it might be suitable to decrease the energy density to increase productivity.



## ***6 List of acronyms***

**AM:** Additive manufacturing  
**IAM:** Integrated additive manufacturing  
**3D:** Three-dimensional  
**CAD:** Computer-aided design  
**RP:** Rapid prototyping  
**STL:** Stereolithography  
**ASTM:** American society for testing and materials  
**SLA:** Stereolithography  
**MJM:** Multi-jet modeling  
**RFP:** Rapid freeze prototyping  
**FDM:** Fused deposition modeling  
**FEF:** Freeze-form extrusion fabrication  
**SLS:** Selective laser sintering  
**DMLS:** Direct metal laser sintering  
**SLM:** Selective laser melting  
**EBM:** Electron beam melting  
**LMD:** Laser metal deposition  
**LOM:** Laminated object manufacturing  
**PBF:** Powder bed fusion  
**LPBF:** Laser powder bed fusion  
**DMLM:** Direct metal laser melting  
**DMLS:** Direct metal laser sintering  
**SEC:** Specific energy consumption  
**SS:** Stainless steel  
**FCC:** Face-centered cubic  
**BCC:** Body-centered cubic  
**MPB:** Melting pool boundaries  
**HAGB:** High angle grain boundaries  
**ANOVA:** Analysis of variance  
**SSLT:** Lowest scanning speed  
**SSL:** Low scanning speed  
**SSM:** Moderate scanning speed  
**SSH:** High scanning speed  
**SSVH:** Very high scanning speed

**SSMM:** Maximum scanning speed

**HDL:** Low hatch distance

**HDM:** Moderate hatch distance

**HDH:** High hatch distance

**HDVH:** Very high hatch distance

**NIST:** National institute of standards and technology

**EDM:** Electrical discharge machining

## 7 List of symbols

- $v_s$ : Scan speed [mm/s]  
 $h$ : Hatch distance [ $\mu m$ ]  
 $h_{opt}$ : Optimal hatch distance [ $\mu m$ ]  
 $d$ : Laser spot size [ $\mu m$ ]  
 $z$ : Layer thickness [ $\mu m$ ]  
 $P$ : Laser power [W]  
 $T_b$ : Build time [h]  
 $LED$ : Linear energy density [J/mm]  
 $AED$ : Areal energy density [J/mm<sup>2</sup>]  
 $VED$ : Volumetric energy density [J/mm<sup>3</sup>]  
 $BR$ : Build rate [mm<sup>3</sup>/s]  
 $V_p$ : Part volume [cm<sup>3</sup>]  
 $T_p$ : Processing time [h]  
 $T_{pre}$ : Pre-processing time [h]  
 $T_{post}$ : Post-processing time [h]  
 $T_d$ : Delay time [h]  
 $T_r$ : Recoating time [h]  
 $T_s$ : Scanning time [h]  
 $C_{job}$ : Cost of the job [€]  
 $C_{direct}$ : Direct cost [€]  
 $C_{indirect}$ : Indirect cost [€]  
 $P_p$ : Machine purchase price [€]  
 $k_s$ : Support material coefficient [-]  
 $k_r$ : Powder recyclability coefficient [-]  
 $p_{powder}$ : Powder price [€/kg]  
 $h_y$ : Hours of production per year [h/y]  
 $a_y$ : Amortization time [h/y]  
 $p_{el}$ : Electricity price [€/KWh]  
 $c_{el}$ : Electricity consumption [KWh/h]  
 $p_{gas}$ : Gas price [€/l]  
 $c_{gas}$ : Gas consumption [l/h]  
 $\dot{C}_{operating}$ : Machine operating cost [€/h]

$C_{part}$ : Cost per part [€]  
 $C_{mat}$ : Material cost [€]  
 $C_{mac}$ : Machine cost [€]  
 $C_{ene}$ : Energy cost [€]  
 $C_{gas}$ : Gas cost [€]  
 $C_{p/p}$ : Pre/post-processing cost [€]  
 $R_a$ : Surface roughness [ $\mu\text{m}$ ]  
 $UTS$ : Ultimate tensile strength [MPa]  
 $YS$ : Yield strength [MPa]  
 $E\%$ : Elongation to failure [%]  
 $\sigma$ : Engineering stress [%]  
 $\varepsilon$ : Engineering strain [ $\text{mm}/\text{mm}$ ]  
 $F$ : Load applied [N]  
 $l_0$ : Initial length [ $\text{mm}$ ]  
 $l$ : length after the load application [%]  
 $\rho_{Arch.}$ : Archimedes density [ $\text{g}/\text{cm}^3$ ]  
 $\rho_{rel.}$ : Relative Archimedes density [%]  
 $m_{air.}$ : mass in air [g]  
 $m_{water.}$ : mass in water [g]  
 $\rho_{theoretical}$ : Theoretical density [%]  
 $\rho_{bulk}$ : Bulk density [ $\text{g}/\text{cm}^3$ ]  
 $\rho_{water}$ : Water density [ $\text{g}/\text{cm}^3$ ]  
 $Por.\%$ : Porosity percentage [%]  
 $Acc.\%$ : Accuracy percentage [%]

## 8 Bibliography

- [1] ASTM F2792-12a, “Standard Terminology for Additive Manufacturing Technologies.” ASTM International, West Conshohocken, PA, 2015, doi: 10.1520/F2792-12A.
- [2] A. Bhatia and A. K. Sehgal, “Additive manufacturing materials, methods and applications: A review,” *Mater. Today Proc.*, 2021, doi: <https://doi.org/10.1016/j.matpr.2021.04.379>.
- [3] I. Gibson, D. W. Rosen, and B. Stucker, *Additive Manufacturing Technologies: Rapid Prototyping to Direct Digital Manufacturing*, 1st ed. Springer Publishing Company, Incorporated, 2009.
- [4] N. Guo and M. C. Leu, “Additive manufacturing: technology, applications and research needs,” *Front. Mech. Eng.*, vol. 8, no. 3, pp. 215–243, 2013, doi: 10.1007/s11465-013-0248-8.
- [5] V. Matilainen, H. Piili, A. Salminen, T. Syvänen, and O. Nyrhilä, “Characterization of Process Efficiency Improvement in Laser Additive Manufacturing,” *Phys. Procedia*, vol. 56, pp. 317–326, 2014, doi: <https://doi.org/10.1016/j.phpro.2014.08.177>.
- [6] R. Singh *et al.*, “Powder bed fusion process in additive manufacturing: An overview,” *Mater. Today Proc.*, vol. 26, pp. 3058–3070, 2020, doi: <https://doi.org/10.1016/j.matpr.2020.02.635>.
- [7] C. de Formanoir *et al.*, “Increasing the productivity of laser powder bed fusion: Influence of the hull-bulk strategy on part quality, microstructure and mechanical performance of Ti-6Al-4V,” *Addit. Manuf.*, vol. 33, p. 101129, 2020, doi: <https://doi.org/10.1016/j.addma.2020.101129>.
- [8] V. Bhavar, P. Kattire, V. Patil, S. Khot, K. Gujar, and R. Singh, “A review on powder bed fusion technology of metal additive manufacturing,” 2014.
- [9] S. Cacace and Q. Semeraro, “Improvement of SLM Build Rate of A357 alloy by optimizing Fluence,” *J. Manuf. Process.*, vol. 66, pp. 115–124, 2021, doi: <https://doi.org/10.1016/j.jmapro.2021.03.043>.
- [10] N. Singh, P. Hameed, R. Ummethala, G. Manivasagam, K. G. Prashanth, and J. Eckert, “Selective laser manufacturing of Ti-based alloys and composites: impact of process parameters, application trends, and future prospects,” *Mater. Today Adv.*, vol. 8, p. 100097, 2020, doi: <https://doi.org/10.1016/j.mtadv.2020.100097>.
- [11] A. Leicht, M. Fischer, U. Klement, L. Nyborg, and E. Hryha, “Increasing the Productivity of Laser Powder Bed Fusion for Stainless Steel 316L through Increased Layer Thickness,” *J. Mater. Eng. Perform.*, vol. 30, no. 1, pp. 575–584, 2021, doi: 10.1007/s11665-020-05334-3.
- [12] A. V Gusarov *et al.*, “On productivity of laser additive manufacturing,” *J. Mater. Process. Technol.*, vol. 261, pp. 213–232, 2018, doi: <https://doi.org/10.1016/j.jmatprotec.2018.05.033>.
- [13] J. P. Oliveira, A. D. LaLonde, and J. Ma, “Processing parameters in laser powder bed fusion metal additive manufacturing,” *Mater. Des.*, vol. 193, p. 108762, 2020, doi: <https://doi.org/10.1016/j.matdes.2020.108762>.
- [14] M. Marrey, E. Malekipour, H. El-Mounayri, and E. J. Faierson, “A Framework for Optimizing Process Parameters in Powder Bed Fusion (PBF) Process Using Artificial Neural Network (ANN),” *Procedia Manuf.*, vol. 34, pp. 505–515, 2019, doi: <https://doi.org/10.1016/j.promfg.2019.06.214>.
- [15] J. Pragana *et al.*, “Influence of processing parameters on the density of 316L stainless steel parts manufactured through laser powder bed fusion,” *Proc. Inst. Mech. Eng. Part B J. Eng. Manuf.*, vol. 234, p. 095440542091176, 2020, doi: 10.1177/0954405420911768.
- [16] A. Leicht, M. Rashidi, U. Klement, and E. Hryha, “Effect of process parameters on the microstructure, tensile strength and productivity of 316L parts produced by laser powder bed fusion,” *Mater. Charact.*, vol. 159, p. 110016, 2020, doi: <https://doi.org/10.1016/j.matchar.2019.110016>.

- [17] H. Meier and C. Haberland, "Experimental studies on selective laser melting of metallic parts," *Materwiss. Werksttech.*, vol. 39, pp. 665–670, 2008, doi: 10.1002/mawe.200800327.
- [18] M. Badrossamay, E. Yasa, J. Van Vaerenbergh, and J.-P. Kruth, "Improving Productivity Rate in SLM of Commercial Steel Powders," in *Technical Paper - Society of Manufacturing Engineers*, 2009, vol. TP09PUB17, pp. 1–13, [Online]. Available: Article.
- [19] K. Guan, Z. Wang, M. Gao, X. Li, and X. Zeng, "Effects of processing parameters on tensile properties of selective laser melted 304 stainless steel," *Mater. Des.*, vol. 50, pp. 581–586, 2013, doi: 10.1016/j.matdes.2013.03.056.
- [20] F. Calignano, D. Manfredi, E. P. Ambrosio, L. Iuliano, and P. Fino, "Influence of process parameters on surface roughness of aluminum parts produced by DMLS," *Int. J. Adv. Manuf. Technol.*, vol. 67, no. 9, pp. 2743–2751, 2013, doi: 10.1007/s00170-012-4688-9.
- [21] F. Calignano, G. Cattano, and D. Manfredi, "Manufacturing of thin wall structures in AlSi10Mg alloy by laser powder bed fusion through process parameters," *J. Mater. Process. Technol.*, vol. 255, pp. 773–783, 2018, doi: <https://doi.org/10.1016/j.jmatprotec.2018.01.029>.
- [22] Y. Song, Q. Sun, K. Guo, X. Wang, J. Liu, and J. Sun, "Effect of scanning strategies on the microstructure and mechanical behavior of 316L stainless steel fabricated by selective laser melting," *Mater. Sci. Eng. A*, vol. 793, p. 139879, 2020, doi: <https://doi.org/10.1016/j.msea.2020.139879>.
- [23] I. Zhirnov, P. Podrabinnik, M. Tokbergenov, A. Okunkova, and I. Smurov, "Optical Monitoring and Diagnostics of SLM Processing for Single Track Formation from Co-Cr Alloy," *Mater. Sci. Forum*, vol. 834, pp. 51–60, 2015, doi: 10.4028/www.scientific.net/MSF.834.51.
- [24] W. Shi, Y. Liu, X. Shi, Y. Hou, P. Wang, and G. Song, "Beam Diameter Dependence of Performance in Thick-Layer and High-Power Selective Laser Melting of Ti-6Al-4V," *Materials (Basel)*, vol. 11, no. 7, 2018, doi: 10.3390/ma11071237.
- [25] Z. Wang, Z. Xiao, Y. Tse, C. Huang, and W. Zhang, "Optimization of processing parameters and establishment of a relationship between microstructure and mechanical properties of SLM titanium alloy," *Opt. Laser Technol.*, vol. 112, pp. 159–167, 2019, doi: <https://doi.org/10.1016/j.optlastec.2018.11.014>.
- [26] E. Ramirez-Cedillo *et al.*, "Process planning of L-PBF of AISI 316L for improving surface quality and relating part integrity with microstructural characteristics," *Surf. Coatings Technol.*, vol. 396, p. 125956, 2020, doi: <https://doi.org/10.1016/j.surfcoat.2020.125956>.
- [27] R. Goodridge and S. Ziegelmeier, "7 - Powder bed fusion of polymers," in *Laser Additive Manufacturing*, M. Brandt, Ed. Woodhead Publishing, 2017, pp. 181–204.
- [28] Y. Oh and S. Behdad, "Assembly Based Part Design to Improve the Additive Manufacturing Productivity: Process Time, Cost and Surface Roughness," 2016, doi: 10.1115/DETC2016-59652.
- [29] D. Buchbinder, H. Schleifenbaum, S. Heidrich, W. Meiners, and J. Bültmann, "High Power Selective Laser Melting (HP SLM) of Aluminum Parts," *Phys. Procedia*, vol. 12, pp. 271–278, 2011.
- [30] "<https://www.eos.info/en>."
- [31] "<https://www.slm-solutions.com>."
- [32] "<https://www.ge.com/additive/who-we-are/concept-laser>."
- [33] R. Poprawe, C. Hinke, W. Meiners, J. Schrage, S. Bremen, and S. Merkt, "SLM Production Systems: Recent Developments in Process Development, Machine Concepts and Component Design," in *Advances in Production Technology*, 2015, pp. 49–65.
- [34] G. Costabile, M. Fera, F. Fruggiero, A. Lambiase, and D. Pham, "Cost models of additive manufacturing: A literature review," *Int. J. Ind. Eng. Comput.*, vol. 8, pp. 263–282, 2017, doi: 10.5267/j.ijiec.2016.9.001.
- [35] E. Atzeni and A. Salmi, "Economics of additive manufacturing for end-usable metal parts," *Int. J. Adv. Manuf. Technol.*, vol. 62, no. 9, pp. 1147–1155, 2012, doi: 10.1007/s00170-011-

3878-1.

- [36] “<https://industria.airliquide.it>.”
- [37] D. Thomas and S. Gilbert, “Costs and Cost Effectiveness of Additive Manufacturing.” Special Publication (NIST SP), National Institute of Standards and Technology, Gaithersburg, MD, 2014, doi: <https://doi.org/10.6028/NIST.SP.1176>.
- [38] Z. Y. Liu, C. Li, X. Y. Fang, and Y. B. Guo, “Energy Consumption in Additive Manufacturing of Metal Parts,” *Procedia Manuf.*, vol. 26, pp. 834–845, 2018, doi: <https://doi.org/10.1016/j.promfg.2018.07.104>.
- [39] M. Baumers, C. Tuck, R. Wildman, I. Ashcroft, and R. Hague, “Energy inputs to additive manufacturing: Does capacity utilization matter?,” *22nd Annu. Int. Solid Free. Fabr. Symp. - An Addit. Manuf. Conf. SFF 2011*, 2011.
- [40] F. Calignano *et al.*, “Investigation of accuracy and dimensional limits of part produced in aluminum alloy by selective laser melting,” *Int. J. Adv. Manuf. Technol.*, vol. 88, no. 1, pp. 451–458, 2017, doi: [10.1007/s00170-016-8788-9](https://doi.org/10.1007/s00170-016-8788-9).
- [41] C. Guo *et al.*, “Effect of processing parameters on surface roughness, porosity and cracking of as-built IN738LC parts fabricated by laser powder bed fusion,” *J. Mater. Process. Technol.*, vol. 285, p. 116788, 2020, doi: <https://doi.org/10.1016/j.jmatprotec.2020.116788>.
- [42] Z. Sun, X. Tan, S. B. Tor, and W. Y. Yeong, “Selective laser melting of stainless steel 316L with low porosity and high build rates,” *Mater. Des.*, vol. 104, pp. 197–204, 2016, doi: <https://doi.org/10.1016/j.matdes.2016.05.035>.
- [43] A. Eliasu, A. Czekanski, and S. Boakye-Yiadom, “Effect of laser powder bed fusion parameters on the microstructural evolution and hardness of 316L stainless steel,” *Int. J. Adv. Manuf. Technol.*, vol. 113, no. 9, pp. 2651–2669, 2021, doi: [10.1007/s00170-021-06818-9](https://doi.org/10.1007/s00170-021-06818-9).
- [44] W. J. Sames, F. A. List, S. Pannala, R. R. Dehoff, and S. S. Babu, “The metallurgy and processing science of metal additive manufacturing,” *Int. Mater. Rev.*, vol. 61, no. 5, pp. 315–360, 2016, doi: [10.1080/09506608.2015.1116649](https://doi.org/10.1080/09506608.2015.1116649).
- [45] M. Yakout, M. A. Elbestawi, and S. C. Veldhuis, “Density and mechanical properties in selective laser melting of Invar 36 and stainless steel 316L,” *J. Mater. Process. Technol.*, vol. 266, pp. 397–420, 2019, doi: <https://doi.org/10.1016/j.jmatprotec.2018.11.006>.
- [46] J. A. Cherry, H. M. Davies, S. Mehmood, N. P. Lavery, S. G. R. Brown, and J. Sienz, “Investigation into the effect of process parameters on microstructural and physical properties of 316L stainless steel parts by selective laser melting,” *Int. J. Adv. Manuf. Technol.*, vol. 76, no. 5, pp. 869–879, 2015, doi: [10.1007/s00170-014-6297-2](https://doi.org/10.1007/s00170-014-6297-2).
- [47] N. Read, W. Wang, K. Essa, and M. M. Attallah, “Selective laser melting of AlSi10Mg alloy: Process optimisation and mechanical properties development,” *Mater. Des.*, vol. 65, pp. 417–424, 2015, doi: <https://doi.org/10.1016/j.matdes.2014.09.044>.
- [48] C. Brown *et al.*, “The Effects of Laser Powder Bed Fusion Process Parameters on Material Hardness and Density for Nickel Alloy 625.” Advanced Manufacturing Series (NIST AMS), National Institute of Standards and Technology, Gaithersburg, MD, 2018, doi: <https://doi.org/10.6028/NIST.AMS.100-19>.
- [49] J. Sun, Y. Yang, and D. Wang, “Parametric optimization of selective laser melting for forming Ti6Al4V samples by Taguchi method,” *Opt. Laser Technol.*, vol. 49, pp. 118–124, 2013, doi: [10.1016/j.optlastec.2012.12.002](https://doi.org/10.1016/j.optlastec.2012.12.002).
- [50] J. Slotwinski, C. Martin, and T. Johnson, “A Survey of Mechanical Property Variability of Additively Manufactured Metals,” Nov. 2021.
- [51] Z. Zheng, L. Wang, and B. Yan, “Effects of laser power on the microstructure and mechanical properties of 316L stainless steel prepared by selective laser melting,” *Int. J. Mod. Phys. B*, vol. 31, no. 16–19, p. 1744015, 2017, doi: [10.1142/S0217979217440155](https://doi.org/10.1142/S0217979217440155).
- [52] J. Liu *et al.*, “Effect of scanning speed on the microstructure and mechanical behavior of 316L stainless steel fabricated by selective laser melting,” *Mater. Des.*, vol. 186, p. 108355, 2020, doi: <https://doi.org/10.1016/j.matdes.2019.108355>.

- [53] I. Yadroitsev and I. Smurov, "Selective laser melting technology: From the single laser melted track stability to 3D parts of complex shape," *Phys. Procedia*, vol. 5, pp. 551–560, 2010, doi: <https://doi.org/10.1016/j.phpro.2010.08.083>.
- [54] Q. B. Nguyen, D. N. Luu, S. M. L. Nai, Z. Zhu, Z. Chen, and J. Wei, "The role of powder layer thickness on the quality of SLM printed parts," *Arch. Civ. Mech. Eng.*, vol. 18, no. 3, pp. 948–955, 2018, doi: <https://doi.org/10.1016/j.acme.2018.01.015>.
- [55] X. Shi *et al.*, "Performance of High Layer Thickness in Selective Laser Melting of Ti6Al4V," *Materials (Basel)*, vol. 9, no. 12, 2016, doi: [10.3390/ma9120975](https://doi.org/10.3390/ma9120975).
- [56] S. Sun, M. Brandt, and M. Easton, "Powder bed fusion processes: An overview," 2017.
- [57] A. Ulbricht *et al.*, "Separation of the Formation Mechanisms of Residual Stresses in LPBF 316L," *Metals (Basel)*, vol. 10, no. 9, 2020, doi: [10.3390/met10091234](https://doi.org/10.3390/met10091234).
- [58] G. Dzukey and ke Yang, "Process Parameter Optimization for Selective Laser Melting of 316L Stainless Steel Material using Taguchi's Statistical Design of Experiment Procedure," *Int. J. Eng. Technol.*, vol. 11, pp. 6–13, 2019, doi: [10.21817/ijet/2019/v11i1/191101014](https://doi.org/10.21817/ijet/2019/v11i1/191101014).
- [59] M. Letenneur, A. Kreitchberg, and V. Brailovski, "Optimization of Laser Powder Bed Fusion Processing Using a Combination of Melt Pool Modeling and Design of Experiment Approaches: Density Control," *J. Manuf. Mater. Process.*, vol. 3, no. 1, 2019, doi: [10.3390/jmmp3010021](https://doi.org/10.3390/jmmp3010021).
- [60] M. Baumers, C. Tuck, R. Wildman, I. Ashcroft, E. Rosamond, and R. Hague, "Combined build-time, energy consumption and cost estimation for direct metal laser sintering," *23rd Annu. Int. Solid Free. Fabr. Symp. - An Addit. Manuf. Conf. SFF 2012*, pp. 932–944, 2012.
- [61] C. Vyas, G. Poologasundarampillai, J. Hoyland, and P. Bartolo, "3D printing of biocomposites for osteochondral tissue engineering," 2017, pp. 261–302.
- [62] Y. H. Zhou *et al.*, "Selective laser melting of Ti–22Al–25Nb intermetallic: Significant effects of hatch distance on microstructural features and mechanical properties," *J. Mater. Process. Technol.*, vol. 276, p. 116398, 2020, doi: <https://doi.org/10.1016/j.jmatprotec.2019.116398>.

## 9 Appendix

Table I:  $R_a$  and  $R_z$  values recorded

	top		1		2		3		4	
	$R_a$ [ $\mu\text{m}$ ]	$R_z$ [ $\mu\text{m}$ ]								
1	11,24	58,08	4,37	28,77	5,57	33,10	5,24	35,19	5,30	31,45
2	10,36	50,54	3,98	25,35	4,82	31,62	4,67	30,97	4,69	33,31
3	10,99	59,44	4,90	30,96	4,93	31,52	4,71	29,12	6,23	37,08
4	10,96	57,98	4,18	27,33	4,96	30,77	4,79	30,33	5,56	36,25
5	11,45	62,57	5,21	33,66	5,91	34,80	5,49	33,90	5,53	33,64
6	10,09	49,99	4,82	29,89	6,01	38,61	5,31	34,45	4,77	32,76
7	7,50	43,83	3,95	27,88	4,64	33,32	4,18	27,07	5,10	29,09
8	9,20	52,40	4,25	27,72	6,25	37,55	3,77	25,85	4,70	31,04
9	11,41	56,94	4,89	25,66	4,78	31,69	4,92	33,66	4,83	32,00
10	9,61	55,64	4,36	28,48	5,64	39,33	4,94	35,39	5,41	31,60
11	11,01	61,77	5,59	34,44	5,78	37,76	5,46	34,98	5,53	34,97
12	11,19	59,53	4,68	29,87	5,19	33,30	4,82	29,50	3,96	27,51
13	10,43	53,60	4,81	30,95	4,84	32,10	5,00	33,03	4,78	28,22
14	9,11	47,91	4,05	29,29	4,95	29,41	3,66	25,68	3,53	22,78
15	10,83	54,16	4,22	27,42	4,03	27,82	4,53	29,67	4,76	28,66
16	11,56	59,95	5,58	33,46	4,78	32,60	4,62	32,57	4,53	32,56
17	11,90	59,74	4,80	32,29	5,73	33,10	4,95	33,37	5,86	34,36
18	10,32	54,56	4,84	32,61	5,50	36,72	4,45	29,40	4,68	30,34
19	8,05	45,93	5,11	31,97	5,07	32,72	4,60	32,31	4,77	28,25
20	10,81	54,14	4,70	29,44	4,96	33,59	4,34	30,07	5,08	31,99
21	11,72	56,95	4,53	28,19	4,62	28,08	4,16	28,47	5,14	35,03
22	10,36	56,31	4,67	30,45	5,29	36,48	3,63	24,71	5,02	34,86
23	13,04	73,78	5,72	35,54	6,26	36,12	5,61	35,47	6,12	38,28
24	10,69	55,70	4,94	31,45	5,49	34,61	4,40	28,12	4,88	30,06

Table II: Standard deviations for  $R_a$  and  $R_z$  measurements

	<b>top</b>		<b>1</b>		<b>2</b>		<b>3</b>		<b>4</b>	
	$\sigma (R_a)$	$\sigma (R_z)$								
<b>1</b>	0,87	4,01	0,95	6,88	1,01	6,24	0,36	4,60	0,53	3,32
<b>2</b>	1,82	4,37	0,09	0,40	0,24	3,03	0,35	3,74	0,83	4,85
<b>3</b>	1,09	3,87	0,34	2,58	1,02	6,68	0,44	1,65	0,64	7,70
<b>4</b>	0,91	8,91	0,39	2,84	0,41	1,21	0,18	1,86	0,78	5,43
<b>5</b>	1,98	10,07	0,55	3,08	0,16	1,61	0,75	6,02	0,59	3,97
<b>6</b>	0,51	3,31	0,42	1,63	0,50	2,68	0,11	2,54	1,29	8,82
<b>7</b>	1,01	4,71	0,21	2,61	0,65	5,06	0,57	1,35	0,23	1,76
<b>8</b>	0,80	4,18	0,33	2,03	0,84	4,10	0,72	6,47	0,37	3,14
<b>9</b>	0,73	4,00	0,44	16,61	0,68	2,46	0,78	3,47	1,28	8,00
<b>10</b>	0,49	8,69	0,37	2,72	0,46	4,49	0,54	1,22	1,35	6,32
<b>11</b>	2,10	6,36	0,99	3,57	0,78	3,58	1,01	4,44	0,56	3,02
<b>12</b>	0,98	2,96	1,23	5,73	0,56	2,73	0,36	3,40	0,35	1,40
<b>13</b>	0,97	4,72	0,23	1,37	0,56	0,25	0,42	1,15	0,63	2,63
<b>14</b>	0,33	5,51	0,09	1,83	0,84	3,61	0,28	3,32	0,23	1,18
<b>15</b>	0,67	5,97	0,25	1,12	0,90	4,49	0,81	3,84	0,27	3,52
<b>16</b>	0,17	3,70	0,30	4,17	0,28	1,43	0,35	2,85	0,42	2,71
<b>17</b>	1,03	7,00	0,54	0,85	0,98	6,94	0,49	3,86	0,55	4,28
<b>18</b>	0,39	2,22	0,98	2,55	0,05	3,95	1,01	4,87	0,55	4,33
<b>19</b>	0,70	6,02	0,29	2,11	1,13	3,42	0,97	1,77	0,69	2,52
<b>20</b>	2,47	10,40	0,51	4,58	0,60	3,55	1,16	5,29	0,39	2,82
<b>21</b>	0,91	4,14	0,13	2,31	0,79	1,96	0,75	4,50	0,57	0,90
<b>22</b>	1,67	8,08	0,24	1,89	0,45	2,42	0,19	3,56	0,45	3,45
<b>23</b>	1,70	8,36	0,07	4,05	1,53	6,78	0,64	1,22	0,88	3,61
<b>24</b>	0,49	5,35	0,84	1,86	0,13	5,54	0,55	1,97	0,88	6,22